VOLUMETRIC HIGH-SPEED IMAGING THROUGH THE USE OF AN ELECTRIC TUNABLE LENS IN A LIGHT SHEET MICROSCOPE SYSTEM

by

JOHN EDWARD PRICE GREEN II

(Under the Direction of Peter Kner)

ABSTRACT

Light Sheet Microscopy is a recently revitalized field of fluorescence microscopy that offers high speed imaging over a wide field of view (FOV). Light sheet microscopes are often used for biological studies of model organisms such as zebrafish because of they offer high-speed imaging of *in vivo* events, high resolution, and optical sectioning. The organisms imaged with a light sheet microscope often serve as models that can for human biology. However, light sheet microscopy is limited to 2D image acquisition. By moving the sample through the focal plane, 3D data acquisition is possible; however, this mechanical movement is often too slow to accurately capture *in vivo* events. By pairing the light sheet microscope with an electric tunable lens (ETL), high speed volumetric imaging can be achieved for the purpose of studying *in vivo* events. We demonstrate the system by imaging the Central Nervous System (CNS) of zebrafish embryos while neuronal events occurred. We demonstrate imaging the brain of the zebrafish at a volume of 400 by 400 by 100μm^3 at a rate of 0.6Hz.

INDEX WORDS: Fluorescence Microscopy, Selective Plane Illumination Microscopy (SPIM), Volumetric Imaging, Electric Tunable Lens, Light Sheet Microscopy

VOLUMETRIC HIGH-SPEED IMAGING THROUGH THE USE OF AN ELECTRIC TUNABLE LENS IN A LIGHT SHEET MICROSCOPE SYSTEM

by

JOHN EDWARD PRICE GREEN II

BS, University of Georgia, 2018

A Thesis Submitted to the Graduate Faculty of The University of Georgia in Partial Fulfillment of the Requirements for the Degree

MASTER OF SCIENCE

ATHENS, GEORGIA

2021

VOLUMETRIC HIGH-SPEED IMAGING THROUGH THE USE OF AN ELECTRIC TUNABLE LENS IN A LIGHT SHEET MICROSCOPE SYSTEM

by

JOHN EDWARD PRICE GREEN II

Major Professor:	Peter Kner
Committee:	James D. Lauderdale
	Eric Freeman

Electronic Version Approved:

Ron Walcott
Dean of the Graduate School
The University of Georgia
May 2021

DEDICATION

I am dedicating this thesis to my family. Patricia and John Green, thank you for pushing me to be better and giving me a strong foundation. I would also like to dedicate this work to my late Uncle Jonathan and Aunt Pam. I miss you both and wish I had more time to show you how far I have come. To my friends Ryan, Dani, Aneek, Roland, Asif, Miranda, Jackson, Collin, Rashad, Emily, Brenson, Quinn, Melissa, Cory, and the host of others, thank you so much for the encouragement and kind words you have given me during my studies. This path has not been easy, but I feel incredibly blessed to have my family and friends in my life. Thank you.

ACKNOWLEDGEMENTS

I would like to dedicate this page to the people who helped me produce this thesis. I would like to express my gratitude to my major professor, Dr. Peter Kner. Thank you for letting me join your lab and learn from you. I truly feel like I can take the skills I have learned in your lab and apply them anywhere. Your support during my time as a graduate student has been instrumental in my growth and appreciation for the field of optics. I hope to mirror your patience, kindness, and intellect as I move forward into my future career.

I would also like to thank my committee, Dr. James Lauderdale, and Dr. Eric Freeman. Dr. Lauderdale, the support from your lab has been invaluable; from the zebrafish specimen to your knowledge dealing with biological studies. I have had a pleasant time working with your group. Dr. Freeman, your guidance and encouragement have been greatly appreciated since my time as an undergraduate.

I want to extend my thanks to several graduate students who have helped me get here. Thank you, Yang Liu for teaching me how to handle the light sheet microscope. I appreciate you taking time to help me understand the general knowledge needed to navigate the field of optics. Carly Duffy, thank you for preparing the zebrafish and being a supportive collaborator. I would also like to thank Ruizhe Lin, Abhijit Marar, and Nahian Siddique for assisting me whenever I had questions or doubts. I appreciate the contributions of everyone involved with this work.

TABLE OF CONTENTS

LIST OF TABLES

LIST OF FIGURES

Page

CHAPTER 1 - INTRODUCTION

Light sheet microscopy is a modality of fluorescence microscopy in which high resolution, high speed and optical sectioning are achieved through illumination with a thin sheet of light perpendicular to the imaging direction. Although light sheet microscopes have existed since 1903 [1], their modern day application was not seen until 90 years later when the Voie group used the light sheet microscope to excite fluorescent proteins in guinea pig cochlea samples [2]. The fields of developmental biology and neuroscience have benefitted from light sheet microscopy due to the ability of light sheet microscopy to directly investigate large specimens like zebrafish embryos or fly (*Drosophila*) larvae. Aside from the transparent nature of these fish, zebrafish make for good models in light sheet imaging due to the similarity of their central nervous system (CNS) morphology to that of humans and due to the existing tools for manipulating their DNA with relative ease [3]. The CNS of the small brain of the zebrafish is made of roughly 100,000 neurons [4]. To better understand the CNS of the zebrafish embryo, a model for higher mammals, high-speed volumetric imaging capabilities, like those offered by light sheet microscopy, are required to capture the many neuronal events happening throughout the brain.

Light sheet microscopy has become a powerful tool for volumetric bioimaging in recent years due to the benefits of high imaging speed, high signal-to-noise ratio, and reduced photobleaching/phototoxic effects [2]. These advantages will be explored and compared to previous fluoresce microscopy methods in this chapter.

Basics of Widefield Fluorescence Microscopy

Fluorescence microscopy is well suited for the interrogation of biological specimens because specific structures can be labeled for observation [5]. Widefield fluorescence microscopy, as shown in Figure 1, can be divided into two pathways: illumination (light red) and detection (dark red/brown). The illumination path uses a light source to supply excitation light to stimulate the fluorophores labeling the specimen. The detection path images the light emitted by the sample onto the camera. The objective lens and tube lens create a magnified image of the sample on the camera. The emission light has a slightly longer wavelength due to the Stokes shift (Figure 2) which allows the dichroic mirror to separate the excitation and emission light [6].

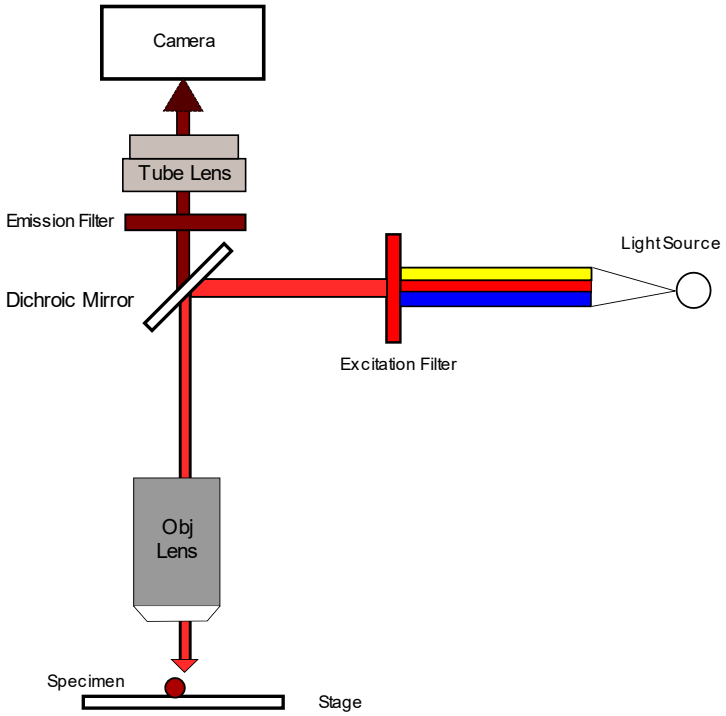

Figure 1. Basic fluorescence microscope schematic. A light source is passed through an excitation filter and reflected off a dichroic mirror to excite the sample. The fluorescence light from the sample is collected by an objective lens and magnified by the tube lens onto a camera.

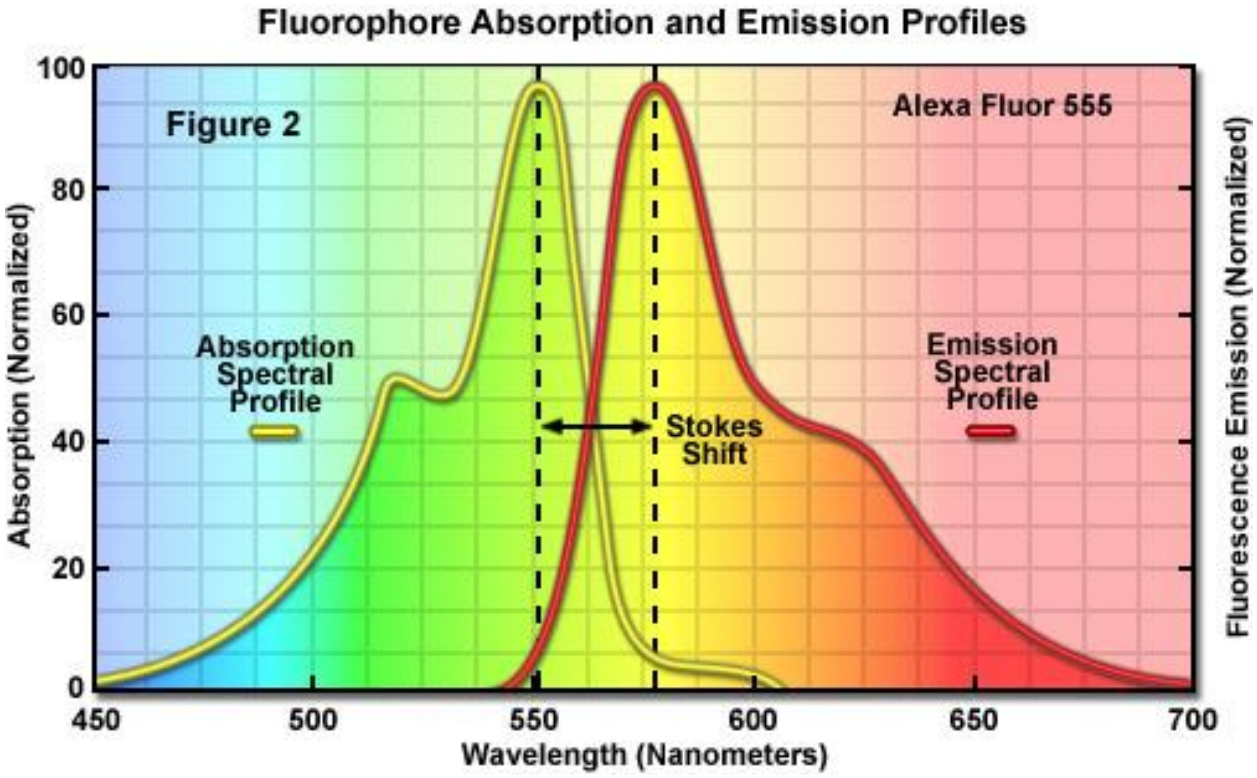

Figure 2. Stokes shift displayed between absorption and emission profiles [7]. The emission spectrum is right-shifted from the absorption spectrum. The right-shifted wavelengths can be passed through filters in the microscope system and captured by a detector.

Fluorescence microscopy is unique in that this modality can image objects tagged by fluorophores with very high contrast due to the relatively large cross section of fluorescent proteins and small molecule fluorophores and the Stokes wavelength shift between the absorption spectrum and the emission spectrum which allows the emission to be separated from the excitation. Fluorescent molecules can be attached to specific proteins through either antibody labeling with small molecular fluorophores or the genetic insertion of a fluorescent protein gene. Small molecule fluorophores are very bright and useful for labeling fixed samples [8]. Fluorescent proteins can be genetically encoded into structures for in vivo imaging applications, such as tracking tumors [9].

Resolution and Magnification

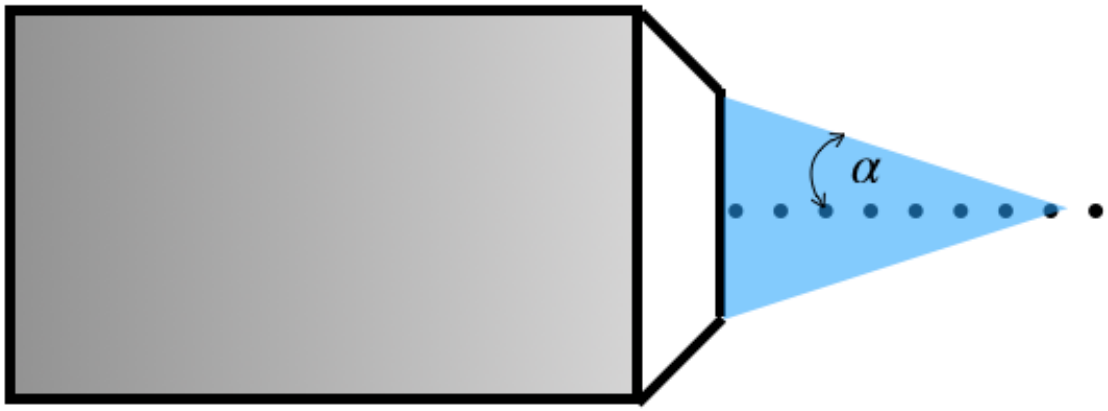

Figure 3. Numerical aperture of objective lens. A point source of light is being collected over an angle, α.

The function of the microscope objective is to capture the fluorescent light emitted by the sample. The numerical aperture quantifies how much light enters the system. The numerical aperture of the detection objective is a dimensionless number that describes the angular acceptance of light into the optical system. The numerical aperture is defined by the following equation [10]:

$$NA = (\mathrm{n})\sin(\alpha).$$

As shown in Figure 3, the maximum angle of acceptance (sometimes referred to as the "half-angle"), α, defines the largest angle that light can diverge from the optical axis and still be accepted by a lens. The numerical aperture is also dependent on, n, the index of refraction of the immersion medium [6]. The magnification of the widefield system is the quotient of the focal length of the tube lens divided by focal length of the objective lens [6].

$$M = \frac{f_{TL}}{f_{obj}},$$

where f_{TL} is the focal length of the tube lens, and f_{obj} is the focal length of the detection lens.

Resolution refers to the ability to discern the details within an image. Resolution is among the most important criteria of a fluorescent microscope system because the better the resolving power, the more detail can be seen in an image. If two point sources of light are imaged by an optical system, two unique spots of light can be seen in the image. As the distance between the point sources becomes smaller, the dots move closer together until they become hard to distinguish. This is known as a resolution limit, or the smallest definable distance for which the two points can still be distinguished (Figure 4). The image of a source of light, no matter how small, has a finite size determined by diffraction.

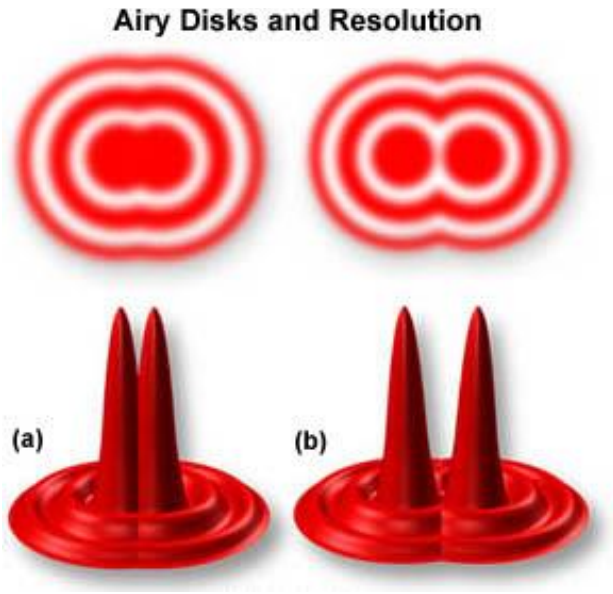

Figure 4. Airy disks and resolution [11]. 4a shows two point sources of light are harder to discern as they approach the resolution limit. 4b shows the light sources are more easily discernable when they become further apart.

Figure 4 illustrates the resolution limit by displaying the images, Airy disks, of two point sources separated by different distances. An Airy pattern is the intensity distribution of light

through a circular aperture in an aberration-free system [12]. The intensity distribution of the Airy disk is described by the following equation [12]:

$$I(r) = \left(\frac{A}{\lambda z}\right)^2 \left[2\frac{J_1(kwr/z)}{(kwr/z)}\right]^2,$$

where r is the radial coordinate, w is the radius of the aperture, J_1 is the Bessel function of the first order, $A = \pi w^2$, λ is the wavelength of light through the aperture, k is the wavenumber, and z is the observation distance between the circular aperture and the Airy disk pattern. As Figure 5 suggests, the further away from the first maximum, the lower the intensity of light. Another way to think about observable point sources is by analyzing the NA of an objective lens, where the minimum resolved distance between two points is $\delta = \frac{0.61\lambda z_i}{w}$, and the nonparaxial resolvable distance is $\frac{0.61\lambda}{NA}$ [12]. For low NA objectives, the NA is $\frac{w}{z}$ in the Airy disk intensity distribution equation. The larger the NA, the wider the angle of light that can be accepted into the system i.e. better resolution. Two considerations for using a higher NA objective lens are the increase in magnification and decrease in working distance.

The local maxima and minima of the Airy disks are easy to see in Figure 5; they can be found by locating the locations where the zeroes of the Bessel function occur. The maxima and minima are generated by the constructive and destructive interference due to the diffraction. Referring back to Figure 4, there is a limit to how close two point sources of light can be and still be distinguished. Specifically, this limit occurs when the Airy disks begin to overlap. (Figure 4a). The Airy disk also plays an important role in image formation. An imaged is formed by the convolution of the Point Spread Function (PSF) with the object in the microscope system. The Airy disk is the lateral in-focus section of the PSF.

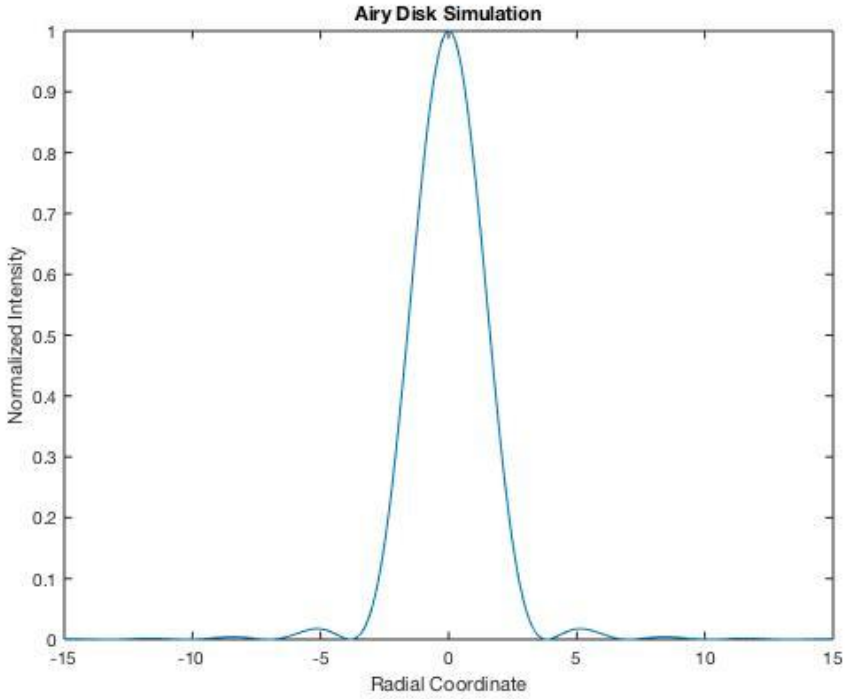

Figure 5. MATLAB® Simulation of 2D Airy disk profile. The centralized maxima has a normalized intensity of 1.

Although there are multiple ways to define the resolution limit, one of the basic definitions is the Rayleigh criteria. The Rayleigh criteria defines the resolution limit between two point sources as occurring when the peak of the image of one point source overlaps the first minima of the image of another point source. Resolution is evaluated in both the axial direction and transverse (lateral) directions [6]. The transverse resolution is defined as:

$$R_T = \frac{0.61\,\lambda_{em}}{NA_{det}},$$

where λ_{em} is the wavelength of emission and NA_{det} is the numerical aperture of the detection objective lens. The equation for axial resolution is defined as:

$$R_{det,axial} = \frac{1.78n\,\lambda_{em}}{NA_{det}^2}$$

Shorter wavelengths and higher indices of refraction allow the optical system to resolve more detail. For an NA of 1.3, index of refraction of 1, and emission light of 400nm, the

resulting transverse resolution is 188nm and the axial resolution is about 421nm. Axial resolution will always be worse than the transverse resolution. Unless otherwise specified, resolution refers to transverse resolution.

The image quality at the end of the detection path also greatly depends on the sampling capabilities of the optical system. The sampling of a system is determined by the pixel size of the detector and magnification. The sampling can be defined by the following equation [6]:

$$R_T > (2)(pixel\ size_i) = 2\frac{pixel\ size_x}{M},$$

where pixel $size_i$ is the size of the pixel at the sample plane. pixel $size_x$ is the size of the pixel at the camera sensor in the x direction, and M is magnification. This equation for the sampling of the transverse resolution, R_T, follows from the Nyquist Theorem which states that to measure a frequency accurately, the sampling rate must be twice the frequency [13].

One of the final basic concepts important to fluorescence microscopy is the signal-to-noise ratio (SNR or S/N). This ratio describes the relationship of the signal (emitted light from the photons) to the total noise of the system. Noise is defined as, "the variation of the signal during repeated observations" [14]. Although there are several different types of noise, the following equation describes the SNR for a perfect detector [15]:

$$SNR = \frac{(QE)(S)}{\sqrt{(F_n^2)(QE)(S + I_b) + (N_r/M)^2}},$$

where QE is the quantum efficiency, S is the input signal (photons/pixel), F_n is the noise factor, N_r is the readout noise, M is the EM gain, and I_b is the background. As the noise in the system increases, the quality of the signal decreases, thus making it tougher to distinguish features in an image. For that reason, high SNR values are strongly desired for observing biological samples [16]. However, if the signal becomes too strong, the pixels become saturated.

When pixel saturation occurs, the pixels of the detector read out the highest possible value and are no longer able to respond to changes in intensity. The oversaturation of pixels can potentially damage the detector in use, so caution should be exercised. A way to overcome this oversaturation is by using filters in the microscope to cut down the amount of signal making its way to the detector.

The three major drawbacks to widefield microscopy are photobleaching, phototoxicity, and the capture of out-of-focus light. When a live specimen is introduced to too much illumination light, the sample will be harmed. As a sample is illuminated over a long period of time, it begins to lose its ability to fluoresce. To overcome the loss of fluorescence, a higher intensity light is needed to excite the sample, but this will also harm the subject. Widefield illumination excites the entire sample. The emission from parts of the sample located away from the focal plane of the objective lens is captured by the camera but is out-of-focus. The out-of-focus light that is captured by the camera results in a large background and additional noise that makes it harder to observe the finer details of the image. To overcome the problem of out-of-focus light, confocal microscopy was developed to effectively block the out-of-focus light and only allow light from the focal plane to reach the detector. In the following section, confocal microscopy will be introduced and described.

Basics of Confocal Microscopy

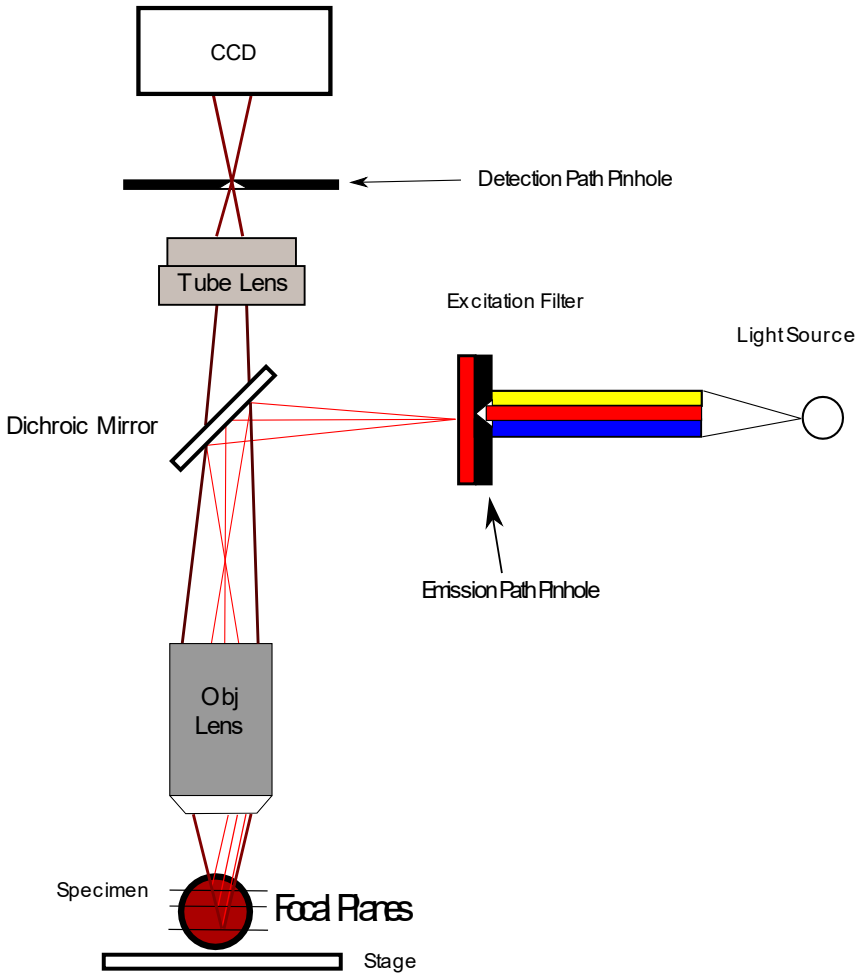

Figure 6. Basic confocal schematic. This microscope scans point-by-point to build images pixel-by-pixel. The pinhole introduced in the emission path is scanned throughout the specimen. The pinhole in the detection path rejects out-of-focus light from the system.

In a confocal microscope, a diffraction limited spot is scanned across the sample. In the detection path, this spot is imaged onto a pinhole that rejects the out-of-focus light that is not focused, as seen in Figure 6. These pinholes allow only the focused portion of light to pass through to the detector that will record the light. The size of the pinhole determines the optical sectioning depth in the microscope [17]. When selecting the size of a pinhole, the specific

applications of the experiment must be considered. When the pinhole in front of the detector is reduced, spatial resolution in the transverse plane (xy) is increased at the cost of the signal that makes its way to the detector [18]. If the pinhole is opened, more signal (including out-of-focus light) from the sample can make its way to the detector at the cost of spatial resolution. The size metric of the pinhole is known as Airy units. One Airy unit is defined as the same size as the diameter of the first maximum of the Airy disk [18]. To illustrate this process, a pinhole sized to 1 Airy unit will pass nearly 80% of the in-focus light and gain 10% of the resolution, however, when the pinhole is reduced to less than 0.1 Airy units, the xy resolution will improve nearly 40% at the cost of losing 95% of the signal [18].

Figure 7 highlights the stark difference in image quality between widefield and confocal microscopy due to the elimination of out-of-focus light. Thicker samples tend to have more problems with out-of-focus light, especially samples greater than 15-20 μm [19].

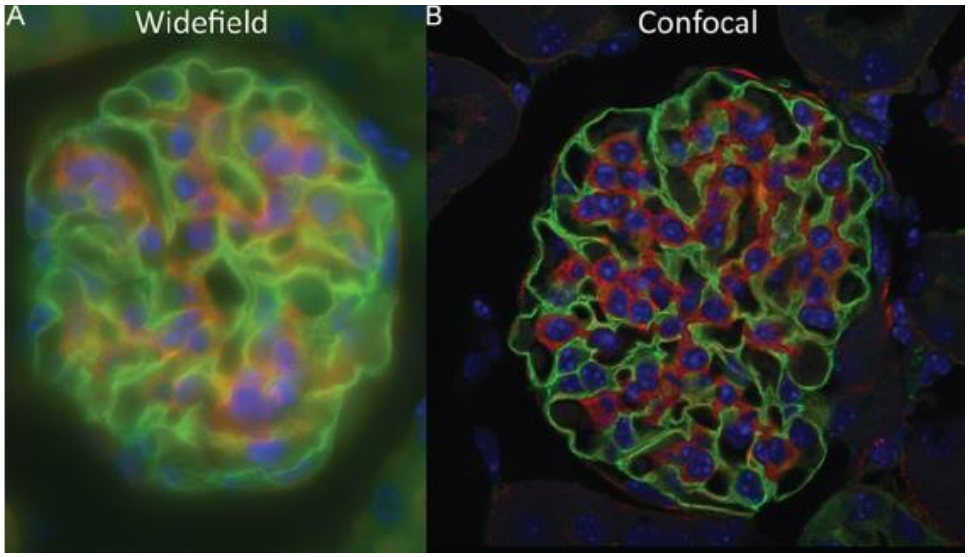

Figure 7. Widefield vs. confocal image of mouse kidney tissue [19]. Out-of-focus light is rejected.

Because confocal microscopy images a focused spot, the focused point must be scanned across the specimen to image a field of view. The process of collecting and building images

point-by-point is known as Raster Imaging [17]. To achieve a video rate of 30 frames per second (fps) across 512 x 512 pixels, a lab group from the Republic of Korea used a polygon mirror to scan 15,000 lines per second. [20]. For this confocal line scanning acquisition method, each pixel was captured at an approximate rate of 1.3μs per pixel. This confocal microscope setup was used to observe individual cells (and their trajectories) within the bloodstream of a mouse observed with a 4μm axial resolution at 33 fps. [21]. In recent years, the same group has pushed their frame rate acquisition to 200 fps for images of 512x512 pixels by modifying their polygonal scanning mirror [20]. At these high rates, very few photons are captured per pixel, and most confocal microscopy is still done at rates of ~ 1 frame per second.

Although confocal microscopy offers benefits over basic widefield fluorescence microscopy, there are some drawbacks and considerations that must be made. First, factors such as the step speed of the stage or scanning mirror for the excitation laser limit how fast images can be taken. Second, the excitation light still passes through the entire thickness of the sample; therefore, photobleaching occurs while the in-focus sections are being imaged [17]. In other words, the out-of-focus portions of the specimen are experiencing intense illumination and heat damage while the data from those regions are not being captured. The slow speeds of the point-by-point image capture process, photobleaching, and tradeoffs for improving the resolution at the cost of signal are all important drawbacks to confocal microscopy. In the next section, I will show that these drawbacks can be addressed and overcome by light sheet fluorescence microscopy.

Light Sheet Microscopy

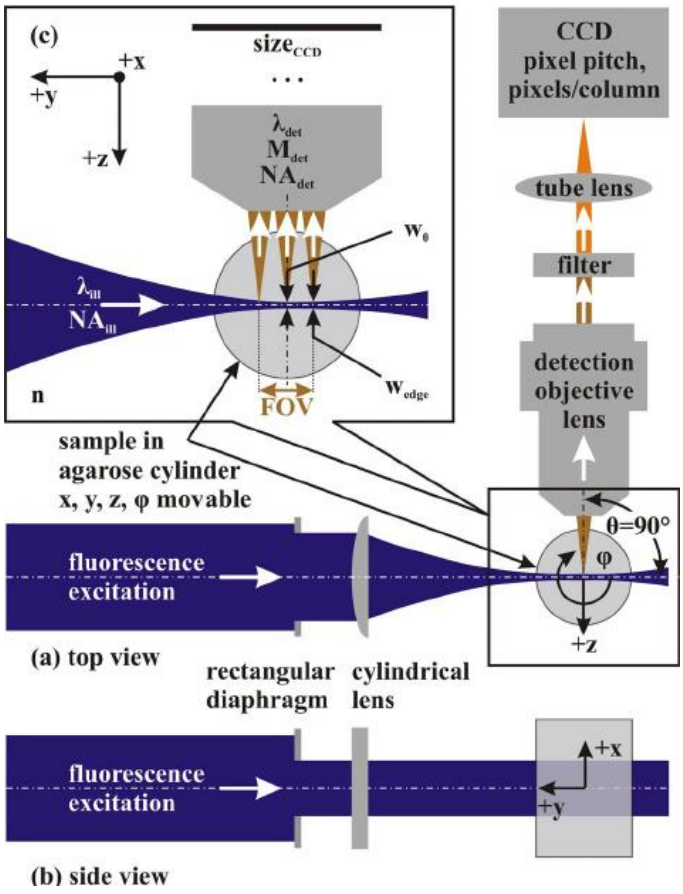

Figure 8. Light sheet microscope schematic [22]. A single plane of the sample is illuminated and collected which cuts down on phototoxicity and photobleaching.

In Light sheet Microscopy (LSM), Figure 8, a thin sheet of light illuminates a thin slice of a large specimen so that only the in-focus plane emits light. Both widefield and confocal microscopy illuminate the entire volume of their sample, introducing phototoxicity and photobleaching to the sample. Widefield microscopes excite and capture the entire volume at once while confocal microscopes scan and capture a specimen point-by-point. Light sheet imaging gets around these problems by illuminating and imaging only the desired plane of a sample [6]. By illuminating and capturing only the desired in-focus plane, light sheet microscopes avoid the problem of out-of-focus light that plagues widefield microscopes. By capturing and illuminating an entire plane across a large FOV, light sheet microscopes avoid

wasting illuminated photons and are faster than confocal microscopes because they do not require raster scanning. The FOV of light sheet microscopes can vary depending on the design, but they can be designed for large FOVs of 5000 µm, high resolution FOVs of 500 µm, and also small FOVs of 50 µm [6]. When using a 450nm laser and 40X, 0.75 objective lens to observe phytoplankton, some groups have achieved high lateral resolutions of 0.81 ± 0.07 µm and axial resolution of 1.42 ± 0.15 µm have been achieved in light sheet systems [23].

In addition to offering high resolution, light sheet imaging has emerged as a modality for in vivo imaging due to the ability of light sheet systems to efficiently excite fluorophores in samples with a relatively small amount of light, thus reducing overall phototoxicity and photobleaching [6]. Too much exposure from the light of the high-powered laser can end up damaging the physiology or end up killing the sample [24]. The lower amount of damage due to efficient excitation gives light sheet microscopy an advantage compared to other microscope imaging modalities like 2-photon and confocal microscopy [25].

Figure 8 illustrates the setup of the light sheet microscope. This setup can be understood in mathematical terms. The image information of a light sheet microscope can be understood as the convolution of the fluorescent object and the overall intensity PSF of the light sheet microscope [6]:

$$i(x, y, z) = o(x, y, z) * |h_{LS}|^2,$$

where $i(x, y, z)$ is the image, $o(x, y, z)$ represents the fluorescent object, and $|h_{LS}|^2$ is the PSF of the light sheet microscope. The standard light sheet microscope's intensity PSF can be described by the following equation [6]:

$$|h_{LS}|^2 = |h_{ill}|^2 \times |h_{det}|^2$$

where the intensity PSF of the light sheet microscope is the result of multiplying the illumination and detection intensity PSFs. This equation is important because it highlights that there are two orthogonally coupled arms of the system that work together to form the image.

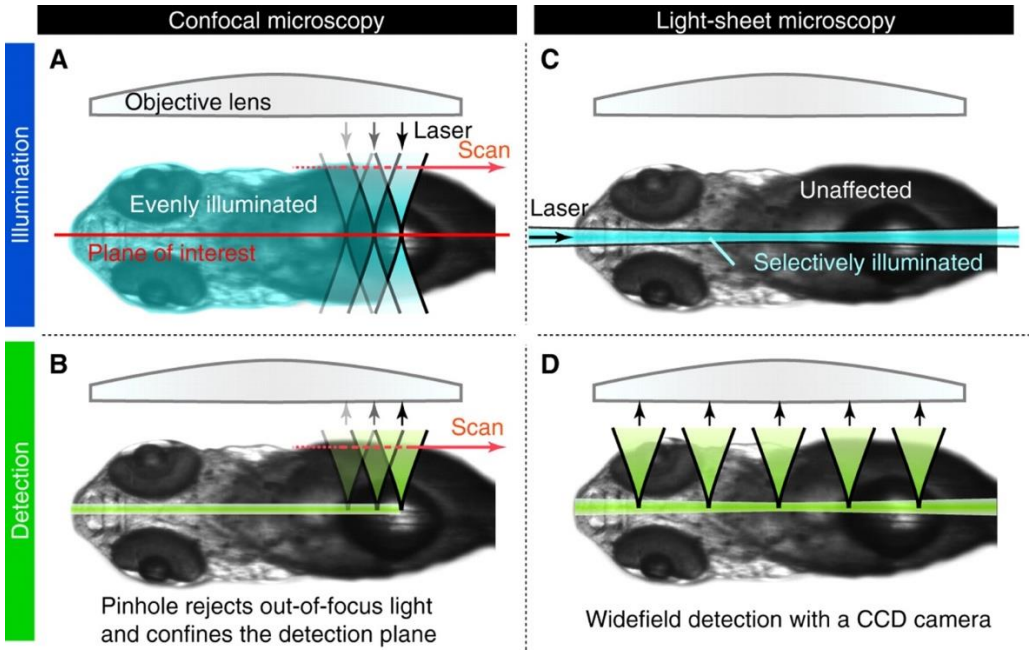

Figure 9. Confocal and light sheet illumination and detection methods [17].

Figure 9 highlights the difference between light sheet and confocal microscopy. Confocal microscopy scans a focal point across the plane of interest while illuminating much more of the sample than what is being captured by the CCD. Light sheet microscopy offers a different approach in that only the detection plane of interest is illuminated in the sample. In LSM, a high-powered laser only excites fluorescent molecules near the focal plane so that only the in-focus emission is then collected and captured by the systems camera [24]. By only exciting the sample in/near the focal plane, light sheet microscopy minimizes photodamage to the illuminated areas, and, therefore, there is less irradiation than other modalities that illuminate the entire sample. This can be seen in the Engelbrecht and Stelzer configuration seen in Figure 8. Many light sheet

systems illuminate from an orthogonal direction to the detection objective to efficiently capture as many photons as possible.

Light sheet imaging is commonly used for relatively large specimens. Embryos are frequently used specimens for in vivo imaging for several reasons. As zebrafish are developing in the embryonic stage, they are largely transparent, which is good for in vivo imaging [26]. The transparent nature of the fish allows for the illumination light path to penetrate the specimen to allow for better detection. Studies have been conducted in the recent past that image the neuronal networks of zebrafish by taking advantage of genetically encoded calcium indicators such as GCaMP5G [27]. Light sheet microscopy has benefitted other in vivo studies of zebrafish such as organogenesis [28] and cardiac-related studies [29] [30]. Although zebrafish are widely used as specimens in light sheet microscopy, other organisms such as *Drosophila melanogaster*, worm embryos, and some plants have been studied with light sheet microscopes [6].

Gaussian Light Sheet

The Gaussian beam is the most common beam profile for light propagating in free space and is the most common beam profile used in light sheet microscopy. The intensity profile of a Gaussian beam is given by the following equation [6]:

$$\varepsilon(\rho, \varphi, z) = \varepsilon(\rho, z) = \frac{1}{\sigma^2(z)2\pi} e^{-\frac{1}{2}\left(\rho^2/\sigma(z)^2\right)},$$

where ρ represents the radial coordinate of the beam and σ is the lateral size of the beam. The equation relating σ to the beam waist, w, is shown by the following equation:

$$\sigma(z) = \frac{w(z)}{2} = \frac{w_0}{2}\sqrt{1 + \left(\frac{z}{\frac{\pi\omega_0^2}{\lambda}}\right)^2},$$

where σ describes the Gaussian beam's radial size as a function of its position along the z axis. Figure 10 shows the normalized intensity of the Gaussian beam if observed from the transverse plane. As the radial distance from the center of the profile increases, the intensity steeply drops off. Figure 11 is the beam profile of the Gaussian beam as observed along the xz-axis. The center of this profile gives the smallest possible beam waist; note that the beam waist equation does not allow for the beam waist to become infinitely small. Because resolution and optical sectioning are controlled by the size of the beam waist in a light sheet microscope, σ must be kept as small as possible over the entire field of view. Both Figure 10 and Figure 11 are ideal Gaussian beams.

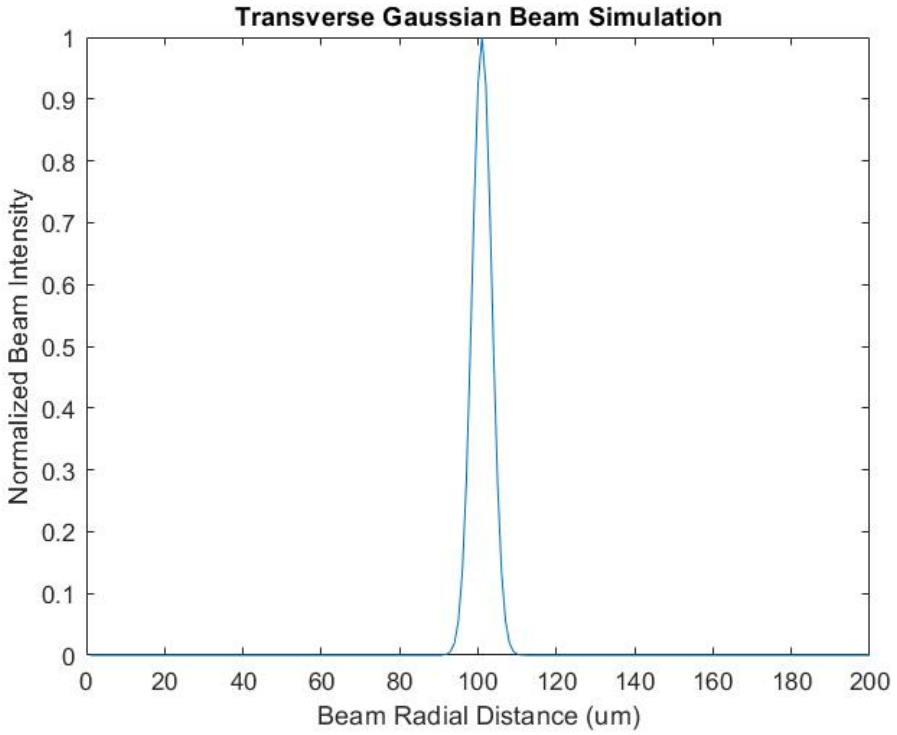

Figure 10. Transverse Gaussian beam simulation. The intensity of the Gaussian beam is highest at the center of the beam waist.

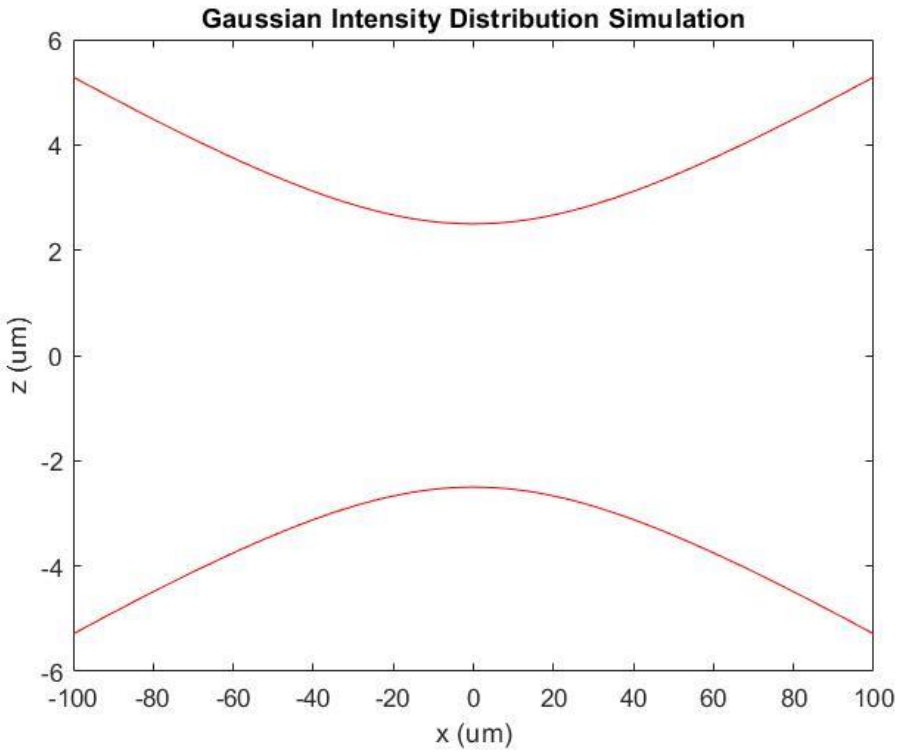

Figure 11. MATLAB® simulated profile for Gaussian beam. The z-axis is the axial coordinate. The x-axis is the transverse coordinate. As the transverse distance from the beam waist is increased, the beam diverges.

Optical Sectioning and Light Sheet Resolution

Light sheet microscopy is also referred to as selective plane illumination microscopy (SPIM) because of the ability to clearly resolve a single plane in the sample. Figure 12 shows a visual contrast of SPIM illumination and point scanning illumination. By illuminating all desired points in a plane at the same time, photobleaching is cut down, the signal to noise ratio is kept high, and image data is acquired quicker. [31]. SPIM methods have been shown to increase the throughput of images up to ~20 fold compared to point scanning microscopy [32].

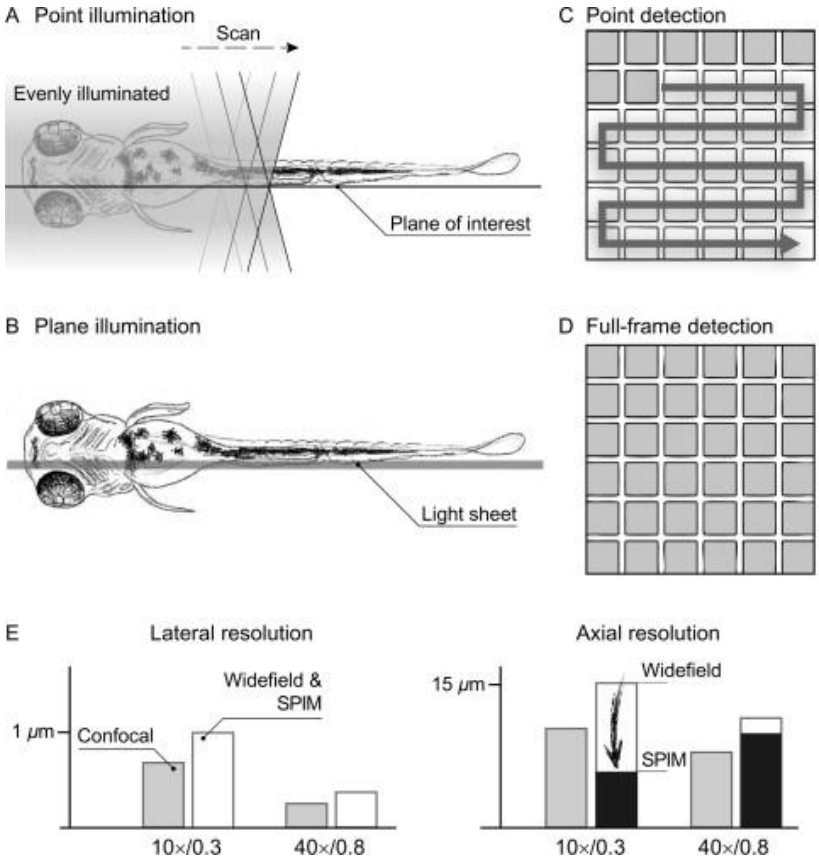

Figure 12. Light sheet detection methods compared to confocal detection methods [31]. 12a-d show illumination and detection of confocal and light sheet systems, respectively. 12e illustrates noticeable improvement of axial resolution when compared to confocal (by factor of 2) and widefield (by a factor of 2.5).

The quality of the image observed in the detection path heavily depends on the thickness of the light sheet beam waist that illuminates the subject. The thickness of a Gaussian beam in the illumination path is described by the following equation [6]:

$$R_{A,ill} = 2\omega_0 = \frac{\lambda}{\pi\theta} = 2\frac{2\lambda f}{\pi D} = 2\frac{n\lambda}{\pi NA},$$

where ω_0 is the beam waist at the center, f is the focal length of the lens, and D is the diameter of the lens. The equation for resolution of illumination describes the optical sectioning ability of the Gaussian light sheet. It should be noted that biological imaging typically uses a ω_0 value between 1-5μm [33]. The Rayleigh Range, z_r, is the range over which the beam diameter is kept within a factor of $\sqrt{2}$ of the beam waist. This range is where the light sheet is the thinnest,

and therefore where the axial resolution is the best within the FOV. The FOV is described by the following equation [6],

$$FOV = 2z_r = 2\frac{\pi\omega_0^2}{\lambda}.$$

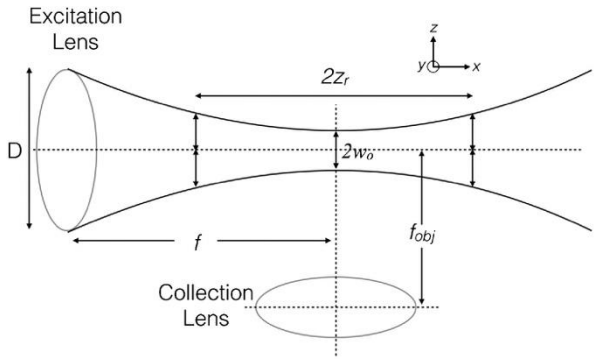

Figure 13. Schematic for illumination and detection objectives with light sheet profile [6].

The detection path objective lens collects the image data from this FOV from an orthogonal view. The Gaussian beam waist across the field of view increases as the light approaches the boundaries of the Rayleigh Range. The boundary value of ω_0 at the edge of the FOV is $\sqrt{2}\omega_{z,0}$ [33]. Clearly, a larger beam waist will allow more out of focus light and is undesired. Optical sectioning capabilities greatly depend on the axial resolution of a light sheet, but at a cost of the FOV. When ω_0 is small, the axial resolution is improved, but the FOV becomes smaller and vice versa. Another drawback to using this single beam Gaussian illumination is that as the light sheet travels across the specimen, the light is absorbed and scattered. The degradation of the light sheet leads to stripes and shadows appearing in thicker specimen [33]. The thicker the specimen, the more striping patterns and shadows will appear. Zebrafish embryos between 5 and 7 days post fertilization [34] [4] are able to express observable neuronal events and they are still translucent.

In Vivo System Speed Considerations

Large specimen like zebrafish embryos or fly embryos (*Drosophila*) are imaged on the scale of several hundreds of microns. Accurate volumetric imaging for *in vivo* imaging requires that the images are captured several times faster than the biological processes are occurring. For example, a zebrafish heart, which is about 200µm in length, can beat at a rate of 2-3 Hz [30]; the minimum Nyquist sampling rate would require sampling at 4-6 Hz. For a confocal setup in which visual stimulation was used in a late-stage zebrafish larvae (7dpf and 21 dpf), neuronal activity was sampled at a rate of 2.3 Hz [35]. This previous work indicates that a sampling rate greater than or equal to 2 Hz is required.

Volumetric Imaging

The acquisition of volumetric images via light sheet microscope is a highly valuable tool for biologist. Observing in vivo processes in a single 2D plane of the specimen only gives data for that singular plane, while at the same time, information from the rest of the volume of the specimen is unrecorded. The motivation for capturing volumetric images is to capture in vivo data throughout the entire specimen. To capture volumetric images, either the focal plane of the microscope must be mechanically moved throughout the sample or the sample must be moved throughout the focal plane. After the movement is stepped, an image is acquired, and the process is repeated.

One method is to move the specimen through a stationary light sheet along the imaging path. A caveat to this method is that slow speeds are needed to keep the sample from becoming too disturbed [30]. Another limit placed on 3D imaging is the need to allow the agar to rest to prevent vibrations from blurring the image. As much as 10 milliseconds are needed to prevent this blurring [32]. In an earlier iteration of a SPIM setup, in which the sample was translated

through the focus with an axial step size of 4μm between each of the 56 slices, the recording speed ranged between 1 to 4 planes per second (1344 x 1024 pixels, FOV = 660μm) [36]. In a more recent study in which brain activity in zebrafish larvae was observed, 3D image acquisition was obtained at a rate of 4 Hz, but with only 5 individual planes separated by 8 μm [32].

The second method of volumetric imaging involves mechanically moving the detection objective to displace the focal plane throughout a stationary sample. Displacement of the detection focal plane can be achieved by mounting the objective lens onto a piezo-operated stage, thus being limited by the inertia of the detection objective [30]. Once the detection lens is moved, the light sheet must also be moved to the same plane along the axis. The process of moving the light sheet through the sample is often referred to as "scanning". Scanning in light sheet microscopy is done by moving the illumination light through the sample via piezo-operated scanning mirrors. Systems utilizing detection mounting have captured a volume consisting of 41 planes in 0.8Hz (~1.3s) while covering 800 x 600 x 200 μm^3 [27]. To acquire these volumetric images, the objective lens had a settling time of 30ms after every 5ms exposure [37]. Other light sheet microscopy methods vary how their objective is mounted, such as oblique plane microscopy (OPM) have achieved fast speeds of 21 Hz imaged across the limited range a 48 μm [29].

Due to traditional 3D acquisition relying on mechanical movement and settling time, volumetric imaging has been limited in speed and the range of axial steps, but new developments in recent years have allowed for a faster image acquisition process. Electrically tunable lenses allow the plane conjugate to the camera to be moved through the sample, therefore enabling 3-D imaging without mechanical movement. The ETL has shown promise as it has been shown to image 17 planes (218 μm x 148 μm) at a volumetric rate of 30Hz [30]. Previous experiments

done with electrically tunable lens and high magnification objectives have shown the ability to track particles of speeds of up to 5 μm/s for 3D acquisition [38]. By rapidly adjusting the focus with the tunable optic component, rapid 3D image acquisition is possible.

Thesis Objective

The objective of this thesis is to build a volumetric imaging capability in our light sheet microscope system through incorporating an Electric Tunable Lens. The desired imaging speed of the system is 1 volume per second. Image performance will be analyzed on fluorescent beads to calibrate the electric tunable lens. After calibration, in-vivo interrogation will be carried out on zebrafish.

The biological processes to be analyzed in our system are seizure events in the central nervous system of the zebrafish larvae. In collaboration with the Lauderdale Lab Group, zebrafish embryos, within a week of fertilization, will be provided. Seizure events will be induced upon these fish by adding PTZ to their environment. Mounting and imaging of the zebrafish specimen will take place shortly after the inducement of neuronal events. An integration and approach for the ETL, like that seen in the Fahrbach and Huisken approach, will be implemented to achieve a fast image capture. In the following chapters of this thesis, I will discuss the specifics of our light sheet microscope system, the design of the light sheet microscope incorporating the ETL, discuss the calibration process of the tunable lens, and present the results of the high-speed volumetric imaging project.

CHAPTER 2 - THE KNER LAB LIGHT SHEET MICROSCOPE

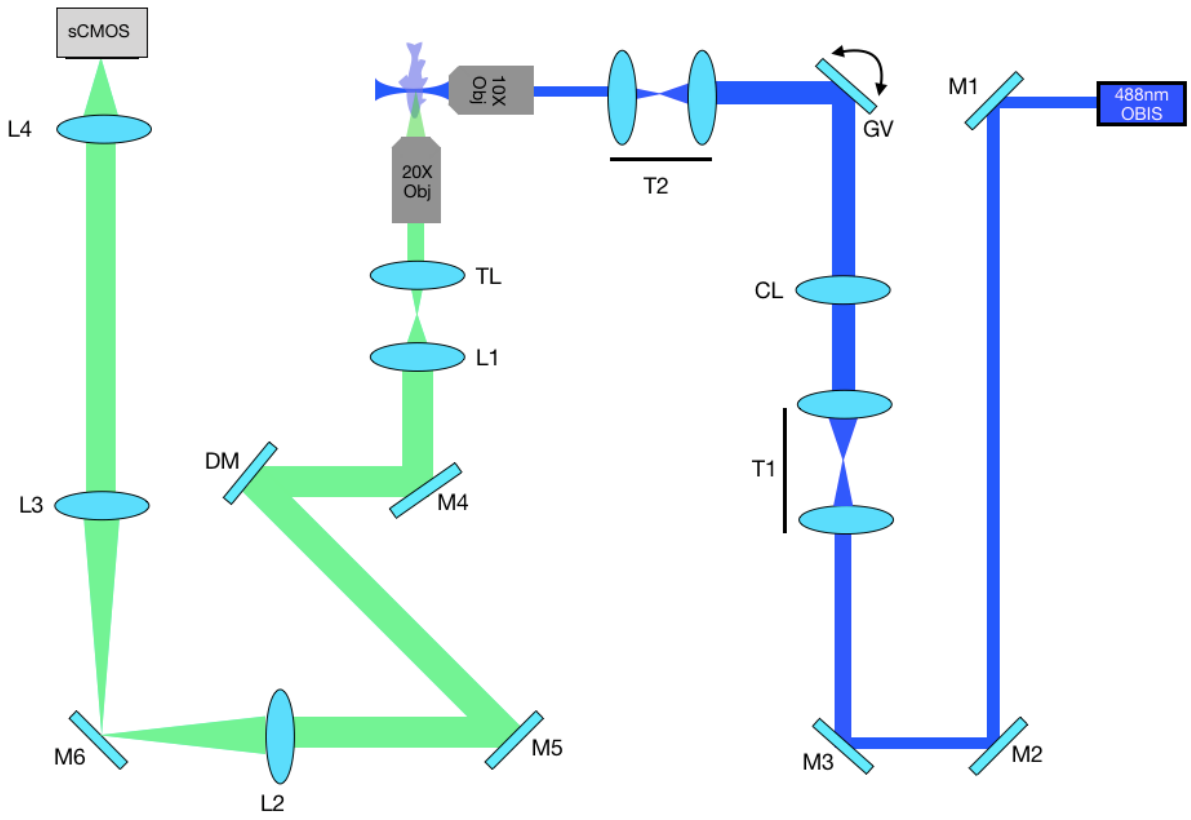

Figure 14. Schematic of the Kner light sheet microscope before insertion of the electric tunable lens. Following the illumination path from the 488nm illumination laser; M1-6: mirror; T1: 2x magnification telescopic lens pair (25mm and 50mm, respectively); CL: cylindrical lens (50mm); GV: galvanometric mirror; T2: 3/5 magnification telescopic lens (50mm and 30mm, respectively), 10x 0.3NA water dipping objective lens. Following the detection path from the 20X, 0.5 NA water dipping objective; TL: tube lens (180mm); L1-L2: relay lens (80mm and 200mm, respectively); DM: deformable mirror; L3-L4: relay lens (200mm and 300mm, respectively); scMOS: high-speed camera.

In this chapter I will describe the Kner Lab light sheet microscope. The design of our SPIM system (Figure 14) is based on the OpenSPIM design [36]. The light sheet microscope is comprised of two major paths: one for illumination and the other for detection. This system can

achieve a lateral resolution of 610 nm and an axial resolution of 4.73 μm for the blue channel (488nm laser excitation). The illumination path provides a Gaussian beam waist of 5.6μm. The FOV captured by the camera is 400 x 400 μm^2 (2048 x 2048 pixels)

The system's volumetric imaging capabilities are bottlenecked due to the 150ms settling time required for the stage when it steps by 3.0μm along the axial direction. When we image with a 20 ms exposure time, our system can acquire a single frame every 170ms. To capture a volume of 40 images, we would acquire that volume at a rate of 6.8 seconds per volume (0.147Hz); this is far too slow to observe neuronal seizure events in zebrafish larvae. This slow volume acquisition speed provided the motivation for implementing the ETL in our system. Below, I describe the design of the system in more detail.

Illumination Path

The goal of our illumination path is to provide optimal optical sectioning of the Gaussian beam across the FOV of the sample. In the illumination path (the blue laser line of Figure 14), the 488nm laser is expanded by a factor of two by the first pair of telecentric lenses (T1) to a radius of 0.8mm. The beam is turned into a light sheet after passing through the 50mm cylindrical lens. The cylindrical lens focusses light along a line, meaning that the beam is focused in one dimension; thus, forming the light into a sheet in that direction. For our system, the cylindrical lens will focus the beam along the axial direction of the detection path. The axial beam waist of the light sheet after passing through the cylindrical lens is determined by the following equation:

$$\omega_{cyl} = \frac{\lambda f_{cyl}}{\pi \omega} = \frac{(488e-6)(50)}{\pi(0.8)} = 0.0097mm = 9.7\mu\text{m},$$

where ω is the beam diameter before entering the cylindrical lens and λ is the laser wavelength. The second telescopic pair, T2, shrinks the illumination axial cross section of the beam by a ratio of 3/5 to bring the size to 5.8 μm at the back pupil plane of the illumination objective in the axial direction. The transverse cross section of this beam is shrunk from a radius of 0.8mm to 0.480 mm. The transverse beam waist diameter over the entire FOV of the illumination detective is given by:

$$\omega_{OBJ,\text{transverse}} = \frac{\lambda f_{obj}}{\pi \omega_{obj}} = \frac{(488e-6)(18)}{\pi(0.0058)} = 0.480mm = 480\mu\text{m},$$

where ω_{obj} is the transverse beam waist before entering the objective lens. The beam waist in the axial direction is calculated similarly. After the axial beam passes through the illumination objective, the beam waist is:

$$\omega_{Obj,axial} = \frac{\lambda f_{obj}}{\pi \omega_{obj,z}} = \frac{(488e-6)(18)}{\pi(0.480)} = 0.0058mm = 5.8\mu m,$$

where $\omega_{Obj,z}$ is this beam waist of the axial portion of the beam before passing through the illumination objective lens. Because we are examining the beam waist in the axial direction, we can compute the FOV over the Rayleigh range. The FOV is described by the following equation:

$$FOV = 2z_r = 2\frac{\pi \omega_{Obj,axial}^2}{\lambda} = \frac{2\pi(5.8^2)}{(488e-6)} = 0.4369mm = 436.9\mu m$$

This means the light sheet beam waist maintains its thickness to within a factor of $\sqrt{2}$ of 5.6 μm across a lateral plane of 436.9 μm.

The galvanometer scanning mirror (Thorlabs GVSM002) is placed conjugate to the back pupil plane of the 10x objective to control the position of the laser along the xy plane of illumination (this corresponds to the yz plane of the detection axis). The galvo mirror can achieve 1kHz with a sinusoidal waveform across small angles of ±0.2° [39].

The 10X, 0.3 NA water dipping lens orthogonally mounted water dipping lens (Figure 15) allows the sample to be at the focal plane of both objectives. The working distance, the space between the front of the objective lens and the sample, of both paths is shown in Figure 16. For our system, both the illumination and detection objectives have a working distance of 3.3mm. Another benefit of the water dipping lens is its ability to reduce overall spherical aberrations in the system [6]. A custom sample chamber, that uses DI water as the immersion medium, houses both objective lenses. The sample is mounted on a stage (Picard industries USB 4D-STAGE) with 4 degrees of freedom (x, y, z, and rotation) to translate and rotate the sample throughout the water-immersed area.

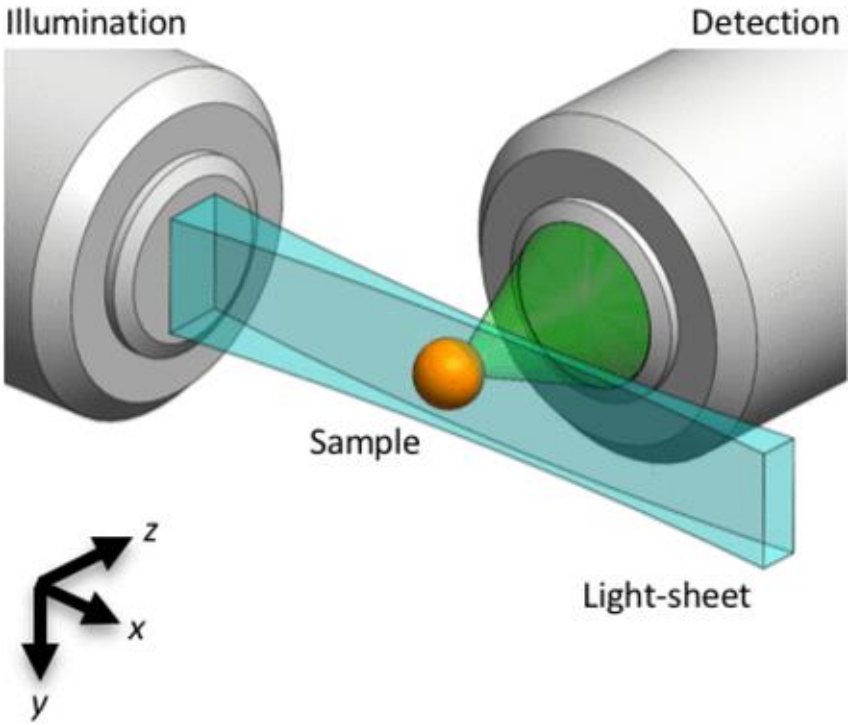

Figure 15. Orthogonally mounted light sheet objectives *[40]*.

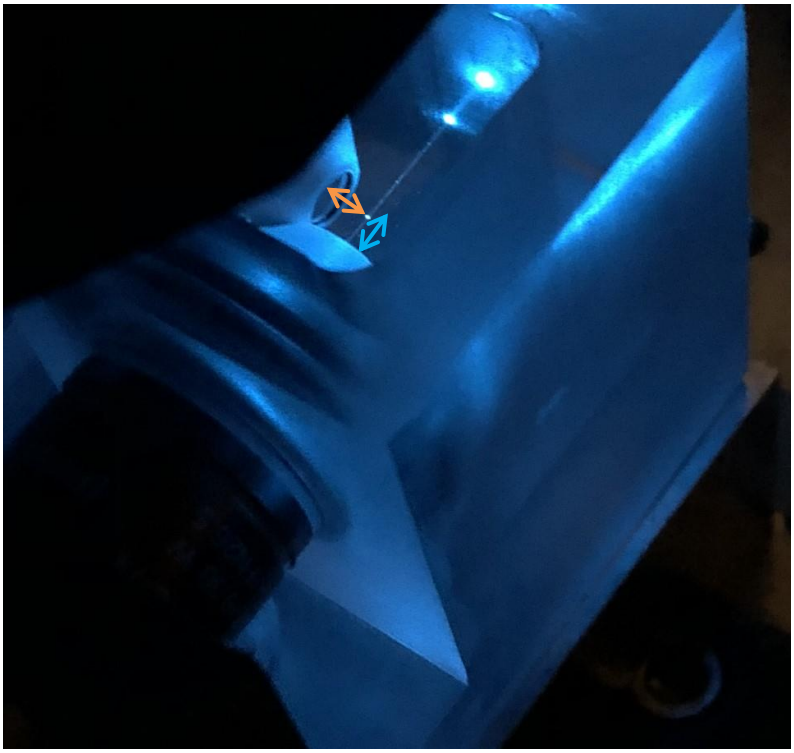

Figure 16. Working distance of illumination (blue arrow) and detection objective (green arrow) of Kner light sheet microscope.

Detection Path

The purpose of the detection arm of the system (Figure 14) is to pass the fluorescent light emitted by the sample through the system and onto the camera. The 20X, 0.5NA detection objective captures the emitted light from the sample. The detection objective and 180mm tube lens magnify the image by a factor of 20 (180mm/9mm). Lens 1 through 4 in Figure 14 transmit and magnify the image onto the camera detector which records the data. The overall system magnification of the detection path is 33.3. This magnification is calculated by multiplying the ratio of focal lengths of lenses 1 through 4 with the initial 20X magnification of the objective lens as seen:

$$M = 20\frac{L_2}{L_1}\frac{L_4}{L_3} = 20\frac{200mm}{80mm}\frac{200mm}{300mm} = 33.3.$$

This system also contains a deformable mirror (DM) (Boston Micromachines Multi-3.5) for correcting optical aberrations. The mirror shape is controlled by 140 actuators [41] that can deform the mirror shape to induce a wavefront that corrects aberrated light. These aberrations, or imperfections, are induced by both the system and the sample. The DM has a diameter of 4mm. Because the objective aperture is too big to fit onto the 4mm DM, L_1 is chosen to demagnify the aperture onto the DM. The aperture exiting the detection objective lens is:

$$Aperture\ size = 2NA(f_{Obj}) = 2(0.5)\left(\frac{180}{20}\right) = 9mm.$$

Lens L_1 (80mm) was chosen with that focal length because of its demagnification ratio. The demagnification factor of $\frac{80}{180} = 0.44$ shrinks the aperture down to a size of 4mm, which is the exact same size of the DM diameter. The final important component to the detection path is the high-speed sCMOS camera (Hamamatsu Orca Flash 4.0v2) which records the data. Each pixel of this camera is 6.5 x 6.5μm and the effective area of the sensor is 13.312 mm^2. As stated

earlier, the transverse resolution of this microscope is 610nm and the system magnification is 33.3. Each pixel of the camera's sensor collects light across 0.1952 μm (6.5/33.3) in the sample plane. To properly acquire an image, the sampling size per pixel must be at least 0.305μm (610 nm/2). Nyquist sampling is fulfilled in this system due to the system's ability to sample 0.195μm per pixel.

Electric Tunable Lens

Figure 17. Optotune EL-10-30-TC [42].

The Optotune EL-10-30-TC was chosen for the project because of its ability to rapidly adjust the axial position of the focal plane in the detection path of the light sheet microscope. The ETL has an adjustable effective focal length between +50 and +120mm, corresponding to a focal power range of 8.3 to 20 dpt. The focal power of the lens is controlled by an input current and the step response of the lens is 15ms [43]. The current is sent to an electromagnetic actuator that exerts pressure on an optical fluid sealed in the ETL. The pressure exerted on the fluid directly affects the curvature of the lens and therefore alters the focal length of the lens [44].

To displace the image plane symmetrically, an offset lens is paired with the ETL by placing it as close as possible to the ETL [30]. The effective focal length of the ETL and offset lens is [30]:

$$\frac{1}{f_{ETL,eff}} = \frac{1}{f_{ETL}} + \frac{1}{f_{OL}} - \frac{d}{(f_{ETL} * f_{OL})} \approx \frac{1}{f_{ETL}} + \frac{1}{f_{OL}},$$

where $f_{ETL,eff}$ is the effective focal length of the ETL and offset lens, f_{ETL} is the focal length of the ETL, f_{OL} is the focal length of the offset lens, and d is the distance between the ETL and offset lens.

The negative value of the offset lens adjusts the ETL focal power range so that it is symmetric about zero power. For a tuning range from P1 to P2, the offset lens should have focal power $\frac{-1}{2}(P_1 + P_2)$. Therefore, for our system with P1=8.3 and P2=20, the offset lens should have focal power 14.15 diopters, corresponding to a 70mm focal length. This would result in a tuning range from -5.85 to +5.85 diopters.

Because manufactures do not generally make offset lenses of -70mm, we chose to pair the ETL with the next closest size, which was -75mm. For the purposes of imaging with our system, the final focal power range used for symmetric displacement ranged from -3.50 to 6.67dpt. The ETL was placed between L3 and L4. The ETL lens was placed in a cage system (Thorlabs**,** CXY2) with manual x-y adjustable translation of ± 2mm to ensure the image plane could be placed directly on the lens.

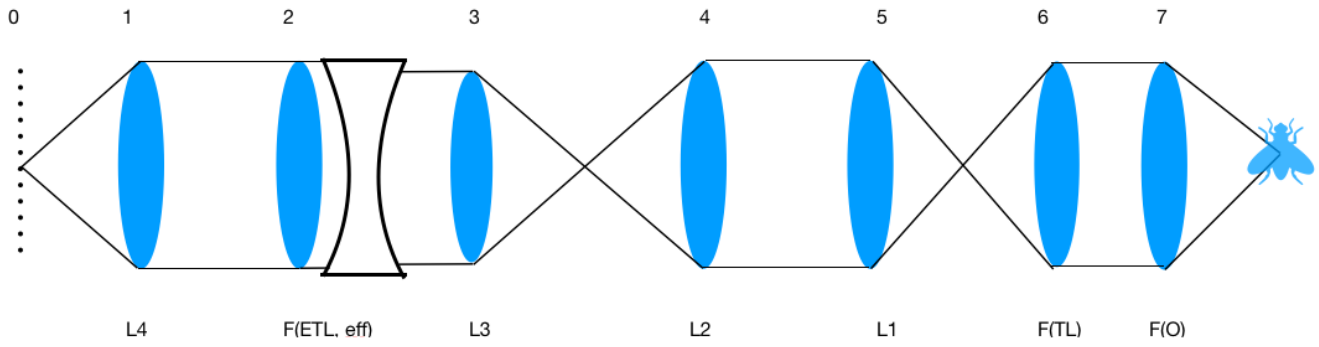

Figure 18. Detection pathway of light sheet microscope from the sCMOS camera to the sample. This model was used for ray tracing purposes to understand how the focal shift in the electric tunable lens would affect the detection pathway. 0) sCMOS Camera (Hamamatsu Orca Flash 4.0v2); 1) 200mm 2) Electric Tunable Lens (Optotune EL-10-30-TC) and Offset Lens (-75mm); 3) 300mm; 4) Relay Lens (200mm); 5) Relay lens (80mm); 6) Tube Lens (Olympus U-TLU 180 mm); 7) Objective Lens (Olympus, UMPLFLN20X/W, 3.3 mm WD 0.5NA).

The implementation of the ETL in our system (Figure 18) gives the following relationship for the position of the focal plane:

$$\Delta z = -\frac{1}{M_{det}^2}\frac{1}{F_{ETL,eff}}\left(\frac{L_1}{L_2}\right)^2 L_3^2,$$

where M is the magnification, $F_{ETL,eff}$ is the effective focal length of the ETL and the offset lens, and Δz is the shift of the focal plane of detection path. The various $L_{\#}$'s correspond to the focal lengths of the lens in Figure 18. The ETL shift, Δz, was calculated to be 180 microns. Ray tracing formulas and geometrical optics were used to derive the equation. A full derivation of the equation for the system can be found in the appendix.

Figure 18 shows a diagram of the ETL implementation with a net focusing power of 0. The black lines represent the rays of light that make their way from the ETL when the effective focal power of the system is 0. When the ETL's focusing power is negative (Figure 19), the ETL lens becomes flatter, thus resulting in a divergence of the light. The resulting angle deflection (the red rays) bend the light further into the sample. In the contrasting scenario, where the ETL focusing power is positive (Figure 20), the ETL lens becomes more round and converges the light rays immediately after the ETL and offset lens. The light rays at focus end up focusing at a closer axial position to the camera.

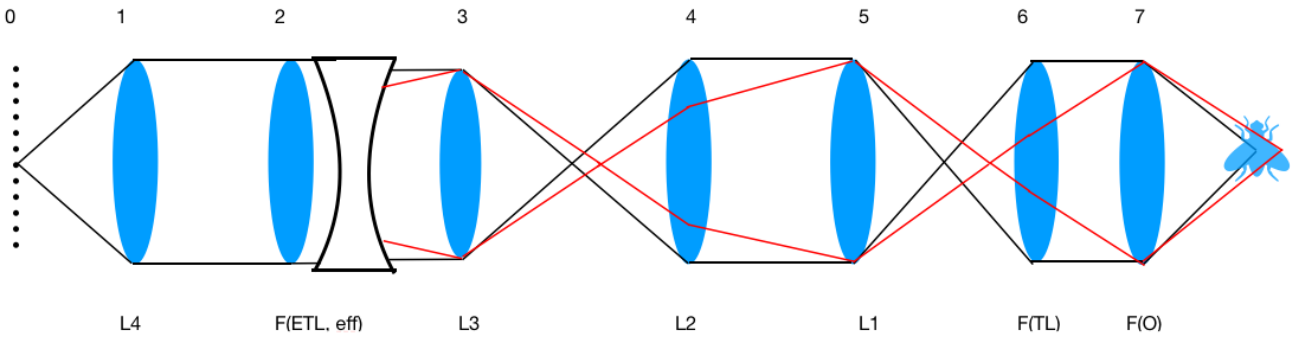

Figure 19. ETL ray deflection with decreasing optical power.

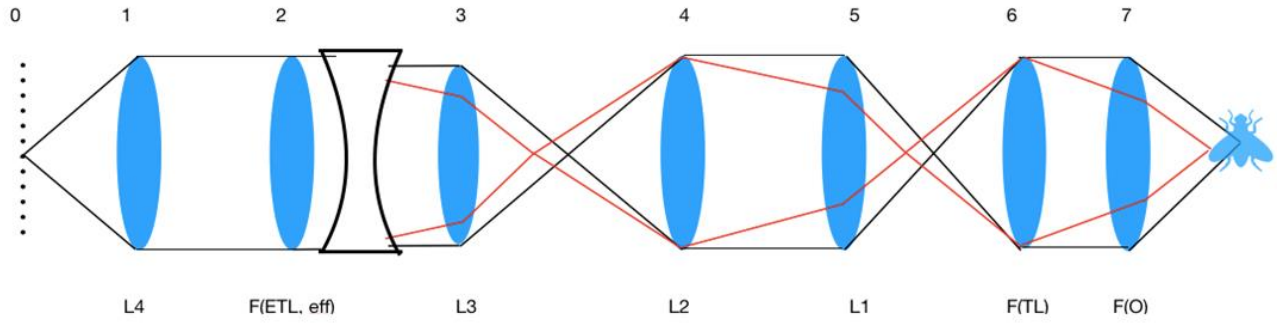

Figure 20. ETL ray deflection with increasing optical power.

Optotune advertises that the EL-10-30-TC focal distances corresponding to a 12-diopter range (8.3dpt-20dpt) at 30° C [44]. Although these are their specifications, our calibration methods provided a guaranteed range (no errors in the software) between ~9.77 and 22.16 dpt. Throughout the experimental process, several calibration attempts were needed to synchronize the galvo and focus, therefore the focal power would vary between experiments. The step-by-step calibration procedure is in the appendix.

Kner Lab Microscope Setup with ETL

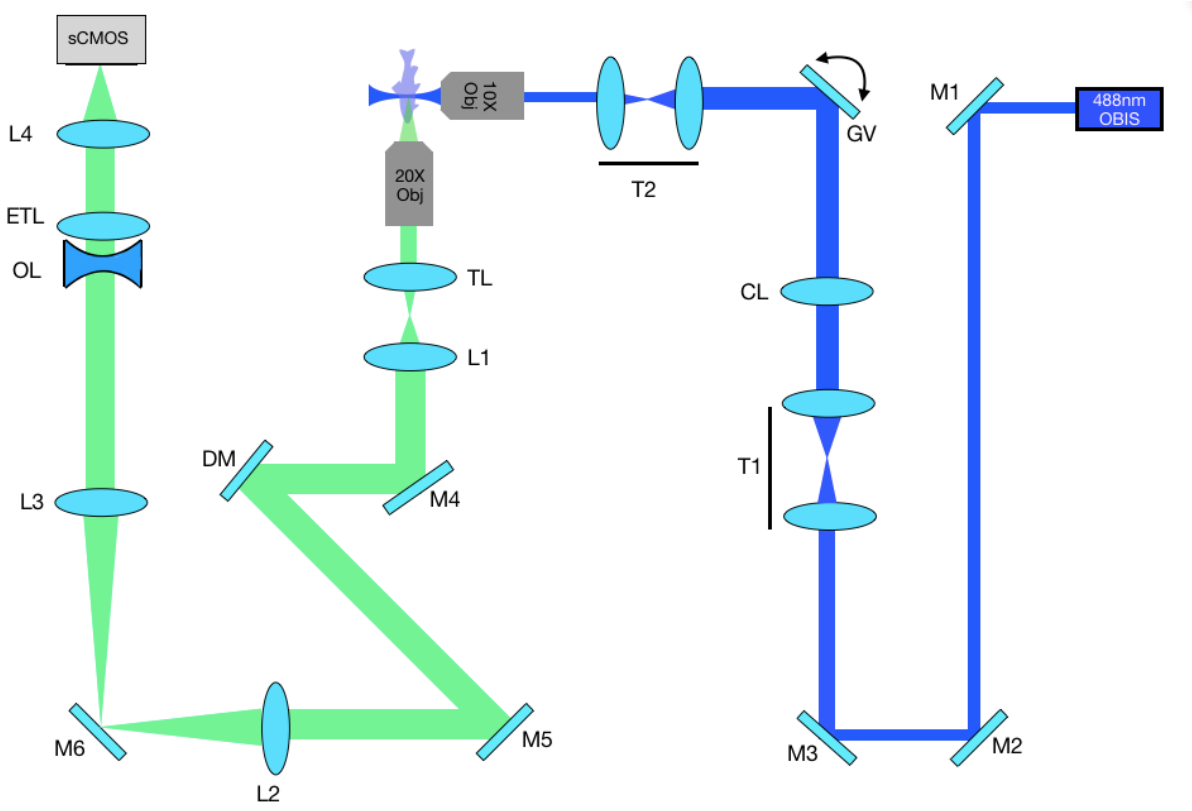

Figure 21. Light sheet with ETL Schematic. ETL and offset lens (-75mm) inserted between L3 (200mm) and L4 (300mm).

Due to the guaranteed achievable range of the tunable lens, the displacement along the axis was estimated to be about 180 microns. Several calibration methods (Chapter 3) were implemented to synchronize the position of the focal plane and the light sheet position. To calibrate the ETL with our light sheet microscope, we must also examine the positioning of the light sheet by the galvanometric mirror.

Galvanometric Mirror Setup

The galvanometric mirrors (I will occasionally refer to this mirror as “galvo” in this document) shown earlier in this chapter can achieve high speeds of movement on the kHz level. The galvanometric system contains two mirrors to control both the x and y angles; however axial scanning corresponds with changing the angle of the galvo’s x-axis component. The system uses a 16-bit value to set a voltage -5 and +5 volts, and the galvanometric mirrors are set to a setting of 1 volt per degree rotation. The limits of the galvo mirrors are set to 10 degrees total. Taking account of the 50mm, 30mm, and objective lenses (18mm) shown in Figure 22, a relationship can be determined between the 16-bit numeric value used to control the galvo mirror and the angle/distance of laser displacement.

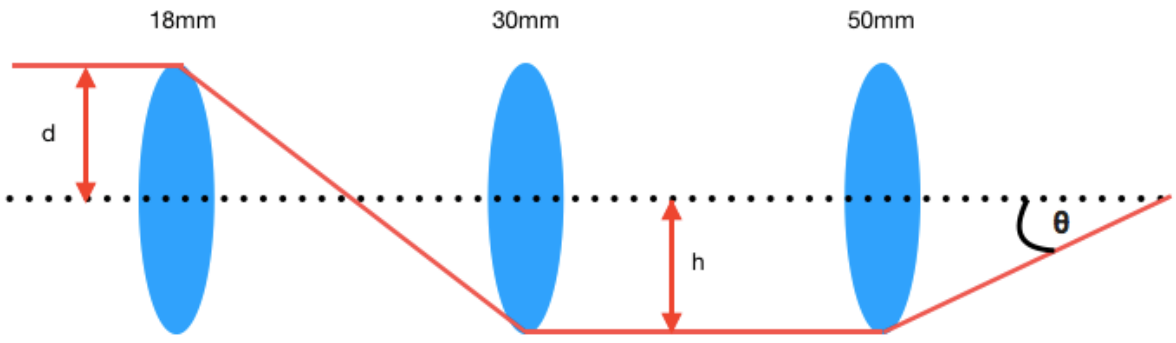

Figure 22. Ray tracing diagram of illumination pathway from the galvo mirrors to the objective lens. The dotted line is the optical axis.

Ray tracing techniques were used to derive the lens relationship of Figure 22. By starting from the light sheet position along the optical axis in the sample and ending with the galvo scanning mirror the relationship for setting the light sheet position can be derived.

$$\frac{d}{18mm} = \frac{h}{30mm},$$

where *d* is the optical axis displacement and h is the height of the beam between the 30mm and 50mm lenses. The focal length of the illumination objective lens is 18mm and the lens before the objective lens has a 30mm focal length. The relationship between the height h and the angle of the galvo mirror (in degrees) is given by:

$$\tan^{-1}\left(\frac{h}{50mm}\right) * \frac{180}{\pi} = \theta,$$

where θ is the angle of displacement along the x-galvo mirror. The relationship between the x-galvo scanning mirror and its programming can be described by the bits used:

$$\theta * \frac{65535}{10} = bit\ range.$$

The bit range is the scan range represented by values between 0 and 65535. Since our system is 16-bit and the galvo was set to 10V range (1V/1°) we can represent the angle in terms of volts; from 0 (-5 volts) to 65535(+5 volts). For example, if a light sheet needed to be displaced 400 microns (.400mm), a rotation of 0.7639° or about 5006 bits would need to be used. In principle, we can set the position of the light sheet to correspond to a position of the imaging plane determined by the ETL.

CHAPTER 3 - ETL CALIBRATION PROCEDURE

To acquire volumetric images in the SPIM microscope, the ETL's axial focus must match the position of the light sheet beam waist at the center. Therefore, the relationship between the ETL's focal power and the focal plane axial displacement needs to be calibrated. Without precise calibration, the focal plane axial location will not coincide with the brightest illumination, resulting in out-of-focus images. Figure 23 and Figure *24* show the extreme difference in image quality when the ETL and galvo are at different positions. By analyzing the image quality as a function of the ETL's focal power and the galvo mirror setting, we can build a relationship (sometimes referred to as a "calibration map") of the ETL's focal power and its axial displacement shift. Because of the research done by the Huisken group, a linear relationship is expected between the ETL's focal power and the shift of the image plane, Δz [30].

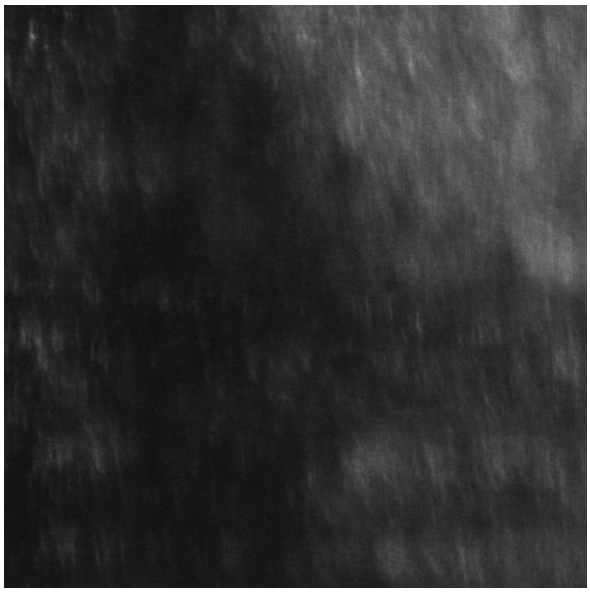

Figure 23. Out-of-focus image frame of 200nm beads. ETL = 14.93dpt.

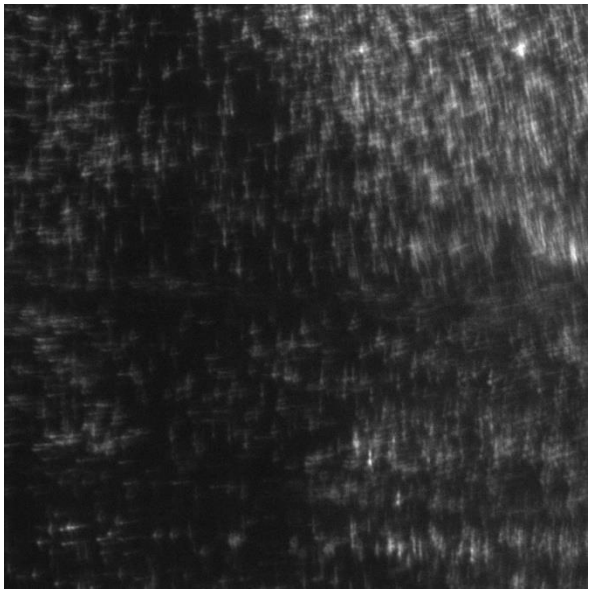

Figure 24. In-of-focus image frame of 200nm beads. ETL = 14.27dpt.

Since the galvo laser displacement is determined by the 16-bit control value (Chapter 2), we decided to map the ETL power settings for those control values. A sample of 200nm yellow-green fluorescent beads was used for determining the calibration. These beads were distributed in ratios of 1:50, 1:100, and 1:200 in 0.2% agarose. The calibration procedure for the ETL involved sweeping the ETL focal power through a range for each light sheet position. Every time the ETL was driven to its next power setting, an image is taken. After all images are taken for every ETL focal power a stack is acquired. For every stack acquired, the galvo mirror is rotated to shift the light sheet to its next position and the process is repeated. Because the sharpest images occur when the image plane is at the light sheet beam waist, the relationship between the ETL power and the image plane can be deduced. An image analysis metric was applied to each stack of images to generate a calibration map along the detection axis. This map can then be validated by taking volumetric image data with the calibration map. If the image stack is in focus as in Figure 24, the test calibration is correct.

Although the Huisken Group used maximum intensity as their metric, we decided on judging the best frame of the bead sample by the metric of sharpness. We used a different image analysis metric because the frame with the maximum intensity did not match the index of the most focused bead image when viewed in ImageJ. This was most likely due to an uneven distribution of beads in the agarose. The sharpness metric is given by the following equation which was implemented in a MATLAB® script:

$$Sharpness_n = \frac{\sigma}{\mu},$$

where the sharpness of each 2D image (n = 1,2,3,…,3000) is the result of dividing the standard deviation of the image, σ, by the mean value of the pixels of the image, μ. This simple equation was repeated 3000 times (30 volumes with 100 frames per volume) to yield the best sharpness over all ETL focusing powers. The calibration map could then be used to drive the ETL in sync with the galvo in a LabVIEW program dedicated to obtaining volumetric data for the fluorescent beads and zebrafish larvae.

For the most accurate calibration we implemented multiple methods. These methods include driving the ETL with different driving signals (sawtooth and sinusoidal), using hardware/software driving methods, and using multiple calibration maps. These different methods were tried because of the effects of hysteresis in the ETL. I will discuss these calibration methods and the results in this chapter.

ETL Sawtooth Calibration

Our first calibration method was to drive the ETL with a sawtooth signal while the galvo was parked. A sawtooth signal driving method was used because we wanted to see if the first calibration method Huisken used could provide a linear relationship between the ETL current and the shift in the image plane [30]. The Huisken group achieved their linear relationship by changing their sawtooth wave to a sinusoidal wave, but we wanted to verify how the sawtooth wave affected the ETL's performance in our system. The ETL was driven in current mode (mA). 30 volumes (sometimes referred to as a "stack") of images were recorded with each volume containing 100 image frames.

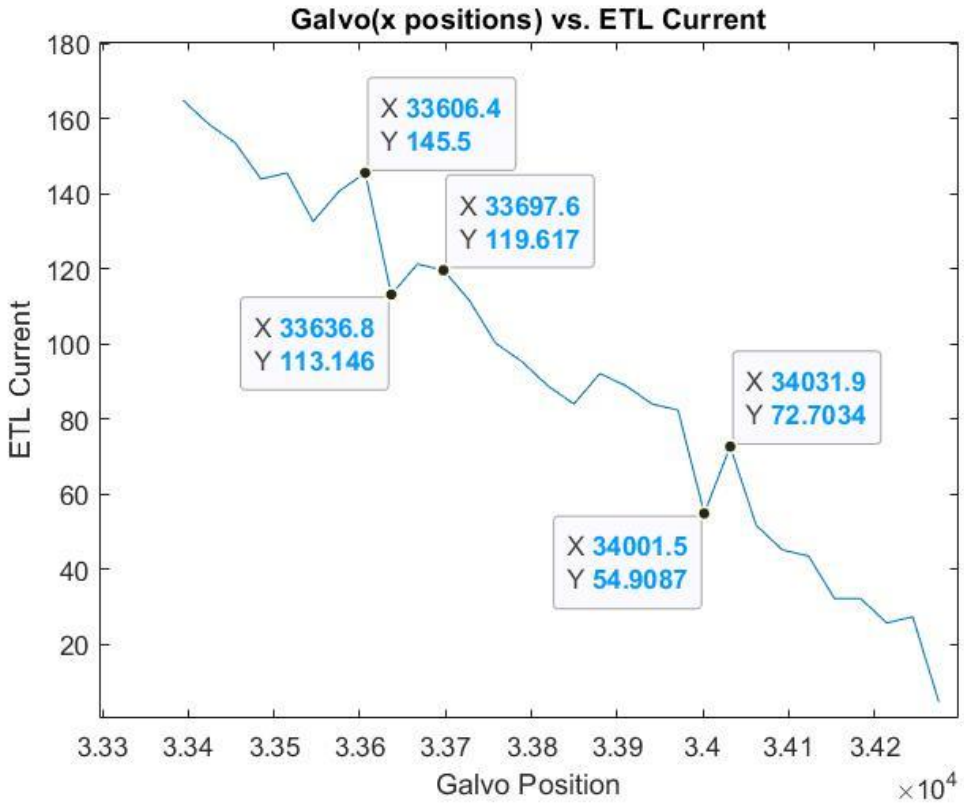

Figure 25. Calibration map of the best galvo points of sawtooth ETL calibration. ETL ran between 4.76-166.53mA; galvo settings between 33394 and 34275 (70µm).

Figure 25 shows a calibration map measured on a sample of 200 nm yellow-green fluorescent beads mixed with 2.0% agarose at a ratio of 1:100. The general shape of the calibration map was too jagged and nonlinear to be used for calibration. As the current being sent to the ETL is decreased, the curvature of the ETL flattens, thus extending the ETL's focus further along the optical axis of the detection path. Therefore, the relationship between galvo position and ETL focus should be linear. Figure 25 shows the relationship between the ETL current and focal shift was not linear as expected. For instance, when the ETL is set to 54.9098 mA, the next expected focused point should occur at a lower current setting (meaning the lens becomes flatter), but the next corresponding point occurred at 72.7034 mA – an obvious increase in current. In this situation, adding more current would mean the axial focus would be displaced in the opposite direction from the light sheet so there was a problem with the sawtooth calibration.

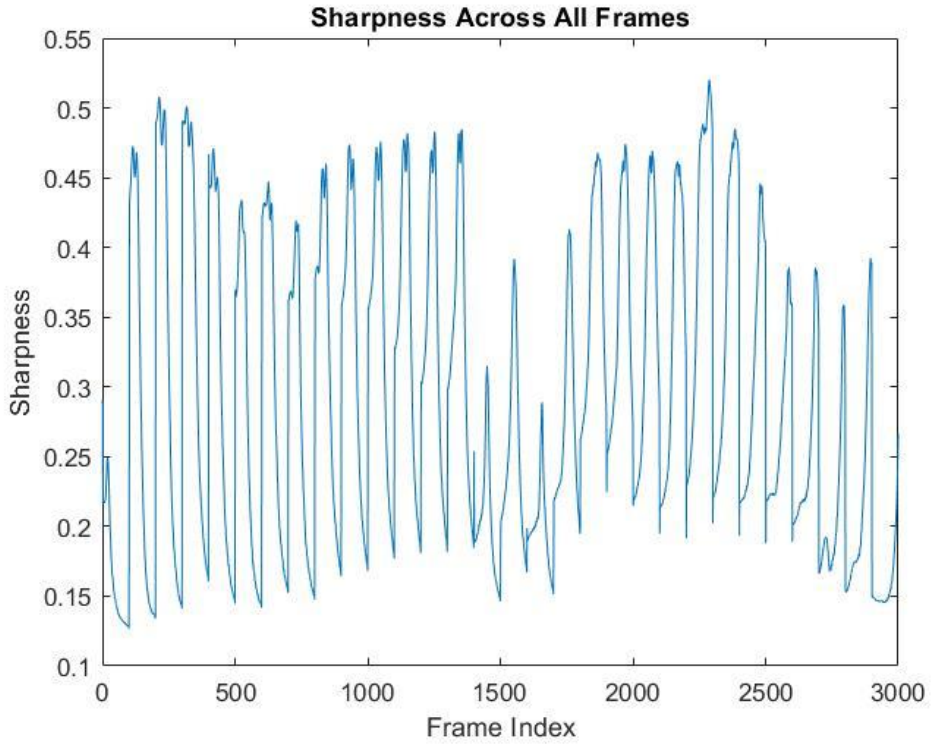

Figure 26. Sharpness of all 3000 frames in the sawtooth calibration.

To investigate this issue, a sharpness plot was generated for all volumes (Figure 26). Observing the sharpness for each stack allows us to look at how the 200 nm beads were imaged throughout the image capturing process. The calibration map is built from plotting where the maximum sharpness for each stack in Figure 26 occurs. Because the experiment drives the ETL focus through the stack of beads, we should see the beads start unfocused, become focused, and go out-of-focus again. This would correspond to the sharpness across this volume having a parabolic arch as seen in Figure 27. Unexpected sharp peaks like the one seen at the beginning of Figure 27 can be caused by an uneven distribution of fluorescent beads in the sample tube. When peaks occur outside of the parabolic arch (i.e. the expected area of unfocus, focus, and unfocus), the resulting calibration map will be inaccurate. Peaks like the one seen in Figure 27 are major factors in the jagged looking calibration map.

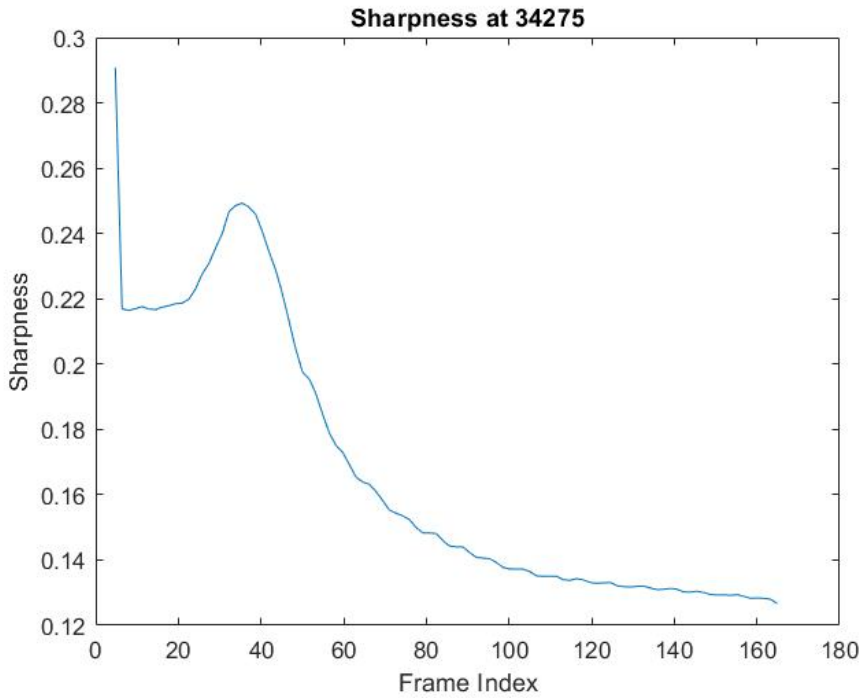

Figure 27. Sharpness of the first volume. Galvo parked at bit 34275.

As the galvo is moved for each volume iteration, we would expect the peak of the parabolic arch to shift its indexed position within each 100 image stack. This can be seen in Figure 28 and Figure 29 where the peak ETL currents are 95.3512 and 88.8804 mA, respectively. The best frame occurring at a successive lower current settings (i.e. lower focal power), makes sense because less power would result in the focus arm extending further into the system.

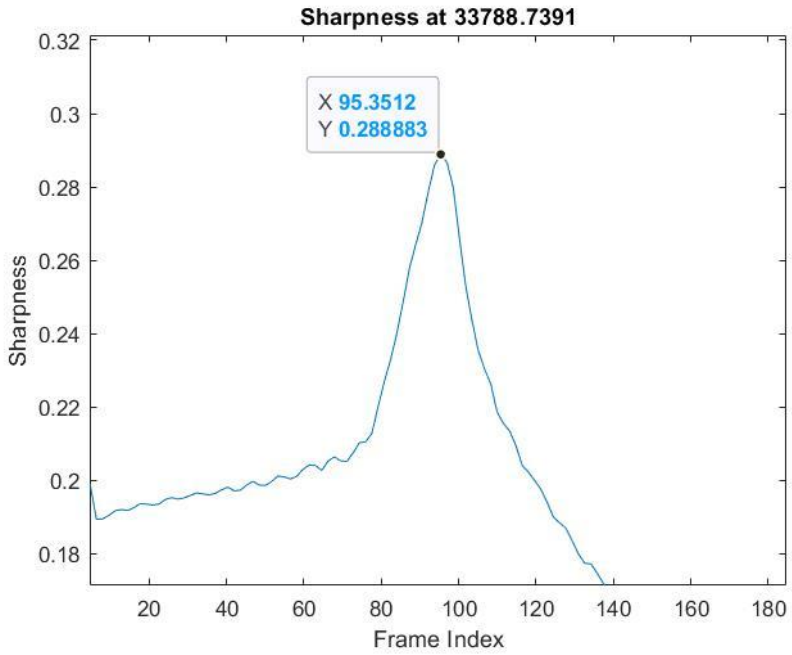

Figure 28. 17th volume of calibration. X-axis is current (mA). Y-axis is sharpness metric. Galvo parked at bit 33789 (bit rounded up).

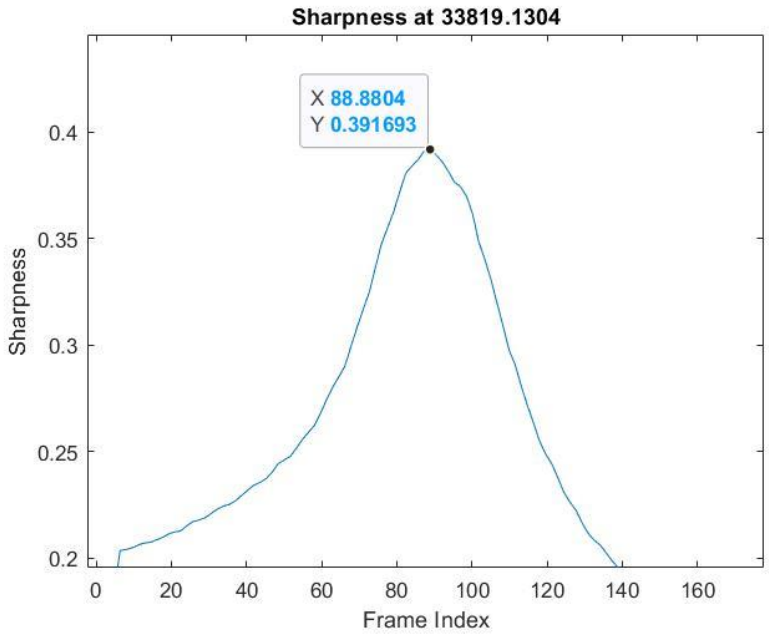

Figure 29. 16th Volume of calibration. X-axis is current (mA). Y-axis is sharpness metric. Galvo parked at 33819 (bit rounded down).

The calibration method of driving the ETL with a sawtooth current signal showed the calibration map was not smooth enough. The Huisken group reported that higher frequency components of driving signals made imaging with the ETL unreliable [30]. In our case, the triangle wave caused unsuitable calibration results the jagged calibration map. To correct the problems in the calibration map, we decided to drive the ETL with a sinewave. This was done to eliminate the overshoot from the high frequency portions of the sawtooth wave. Instead of controlling the ETL with software, we decided to directly input the sinewaves with a hardware control method.

ETL Software Sinewave Calibration

To investigate the nonlinear calibration map, the driving wave was changed to a software sinewave (via LabVIEW). The software sinewave was selected to avoid high frequency driving components that hinder the construction of a linear calibration map. The ETL was run in focal power mode instead of current mode. This was done to make sure that the temperature of the lens would not affect the shape of lens (refer to Appendix C). The bead ratio was strictly kept to 1:200 for this experiment so each individual plane of sparse sample that was captured could be discerned by the sharpness quality metrics. A new MATLAB® script was devised for this calibration mode to handle the calibration process and give a linear relationship between ETL diopters and the galvo mirror position.

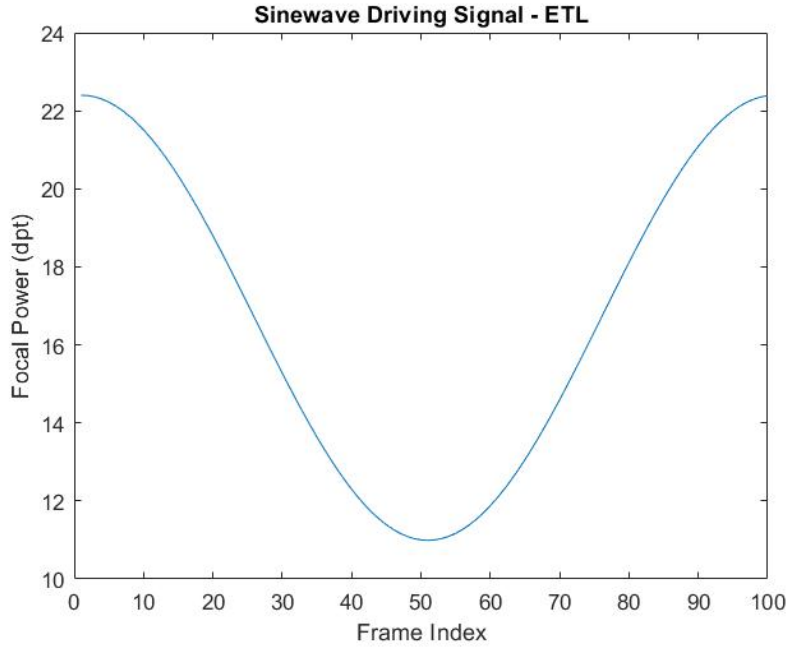

Figure 30. ETL diopter sinewave. Generated between 11.79 dpt and 17.87 dpt. 100 focal power points were generated in this sinewave. Note that the trough occurs at index 51. X-axis is frame index. Y-index is the diopters of the ETL.

Figure 30 shows the diopter-controlled sinewave that drove the ETL. 100 points were generated along this sine wave from the crest to the trough. Because the best frame would occur

twice, the first 50 generated points of the sinewave were referred to as the “forward” part of the sinewave, while the later 50 generated points were referred to as the “backwards” part of the sinewave. Both portions of the sinewaves would individually build their own calibration map.

As seen in Figure 31, there were two peaks for each stack of 100 photos. The existence of the two peaks was expected due to the ETL’s sinewave driving through the galvo laser twice. The maximum sharpness of each peak was apparent from the sharpness plot.

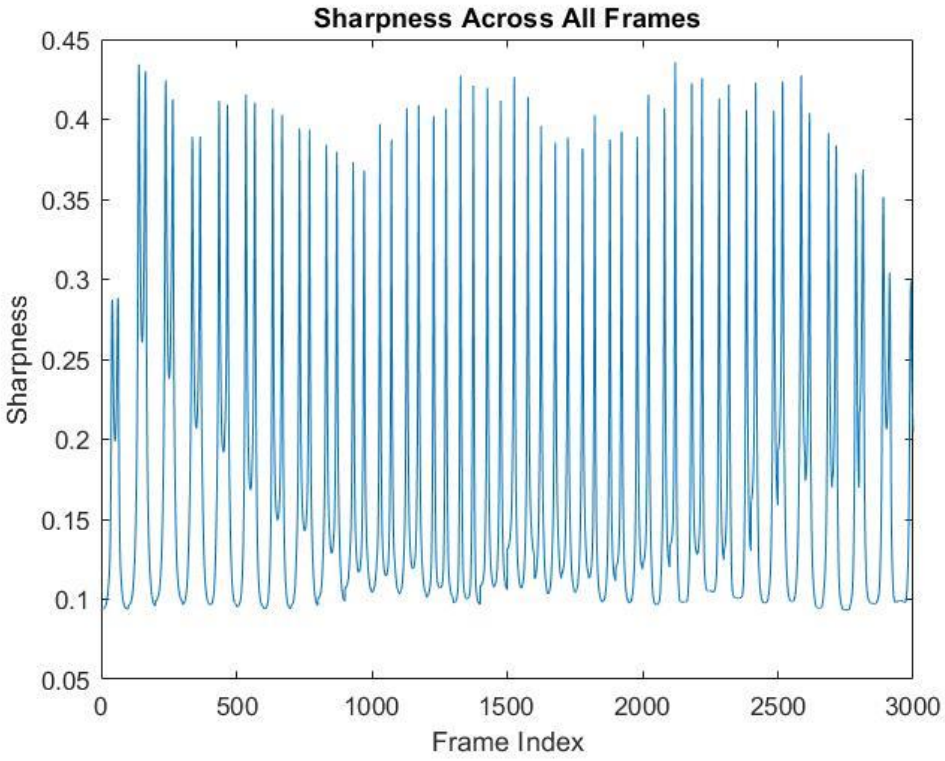

Figure 31. Calibration sharpness (diopter mode). Two peaks occur every volume (1 volume = 100 frames). X-axis = frame index. Y-axis = sharpness metric.

Figure 32 shows that these peaks did not occur at the same place in the sinewave. This suggest that the temperature invariance did not affect the ETL, but instead a hysteresis was present in the ETL. The sinewave that drives the ETL generates the focal powers that are symmetric, so the best focused frame of the beads should be seen twice every period. Because each stack of images consisted of 100 frames (with the middle of the sinewave occurring at the

51st frame of every period), the best in-focus frames should occur an even number of steps away from the center (in this case, the trough at the 51st frame) of the sinewave. For example, if the best frame from the first half of the wave was observed at frame 40 (11 frames away from the middle sinewave trough), then the ETL should drive back through the best in-focus frame at index 62 (also 11 frames away from the middle sinewave trough). The MATLAB® calibration curve showed that the best frames of each sinewave was uneven. With the middle of the curve occurring at index 51, we can see in the first stack of Figure 32, the best focus frame occurs 21 frames away on the forward side of the sine curve while it occurs 22 frames away. In the other stack shown between frames 1300 and 1400, we can see that the sharpest frames occurring 23 and 24 frames for the forwards and backwards portions. For several previous calibrations, the forwards and backwards curves were often mismatched by 3-4 frames. Although it may not seem very pronounced for this calibration, the mismatched frames were separated by as much as 0.38 diopters, so the evidence of this change in position of the best focus frame was concerning.

Figure 33 shows the linear calibration for the forward and backward sections of the sinewave. The hysteresis can be observed in the fact that the calibrations curves are offset. These calibration curves provide a map of the ETL for a known number of galvanometric positions represented in 16-bit.

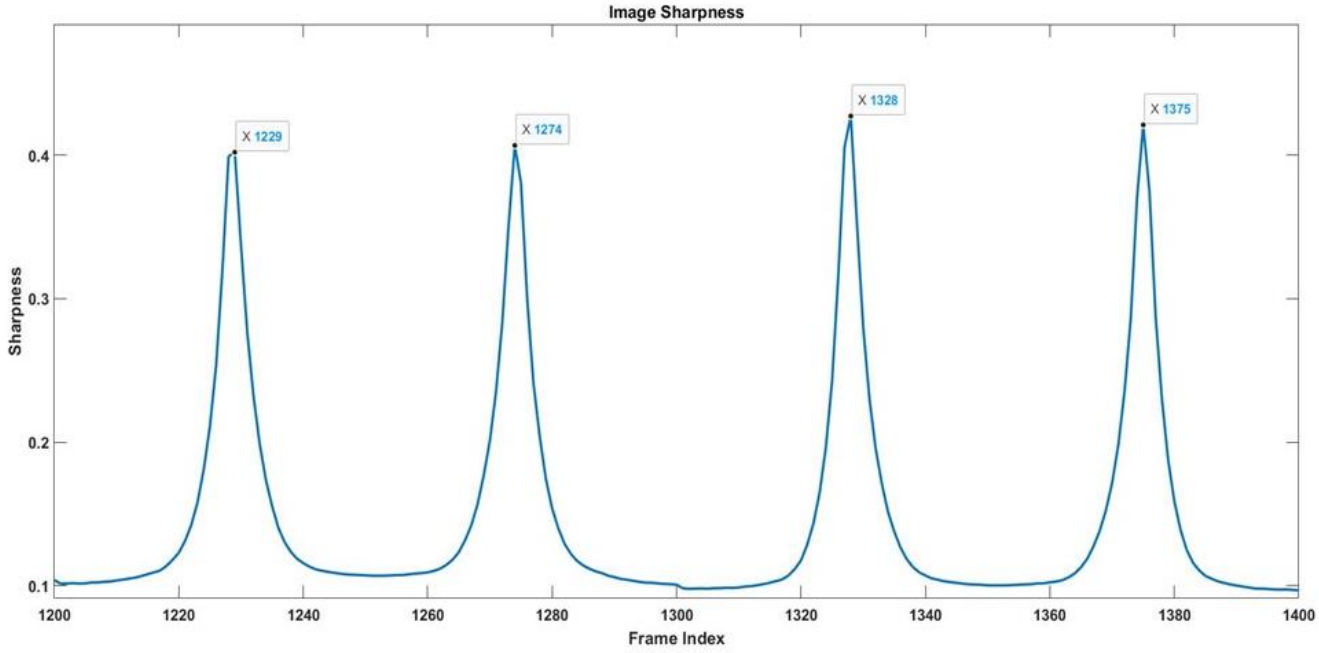

Figure 32. Nonsymmetric sharpness locations in sine wave for 13th and 14th volumes. The middle of the sine wave is at the 51st index frame.

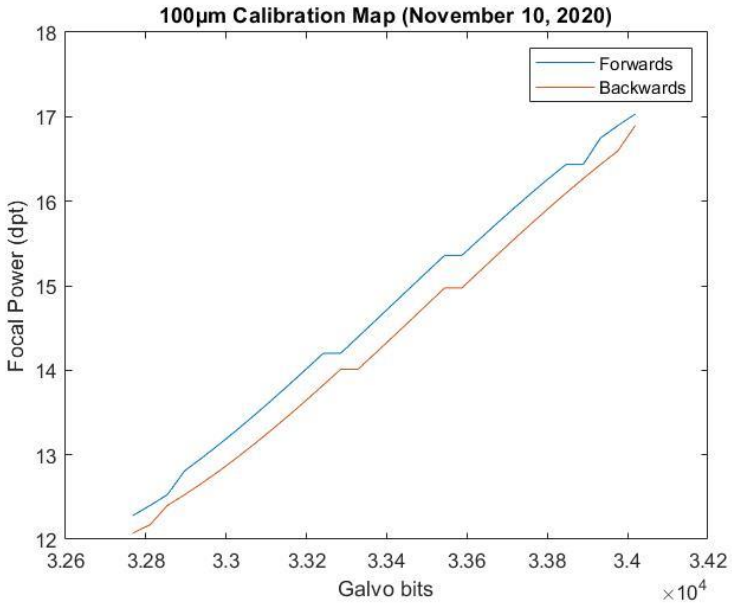

Figure 33. Calibration curve of forwards and backwards waves for 100µm. The raw data of best frame position is displayed in the graph.

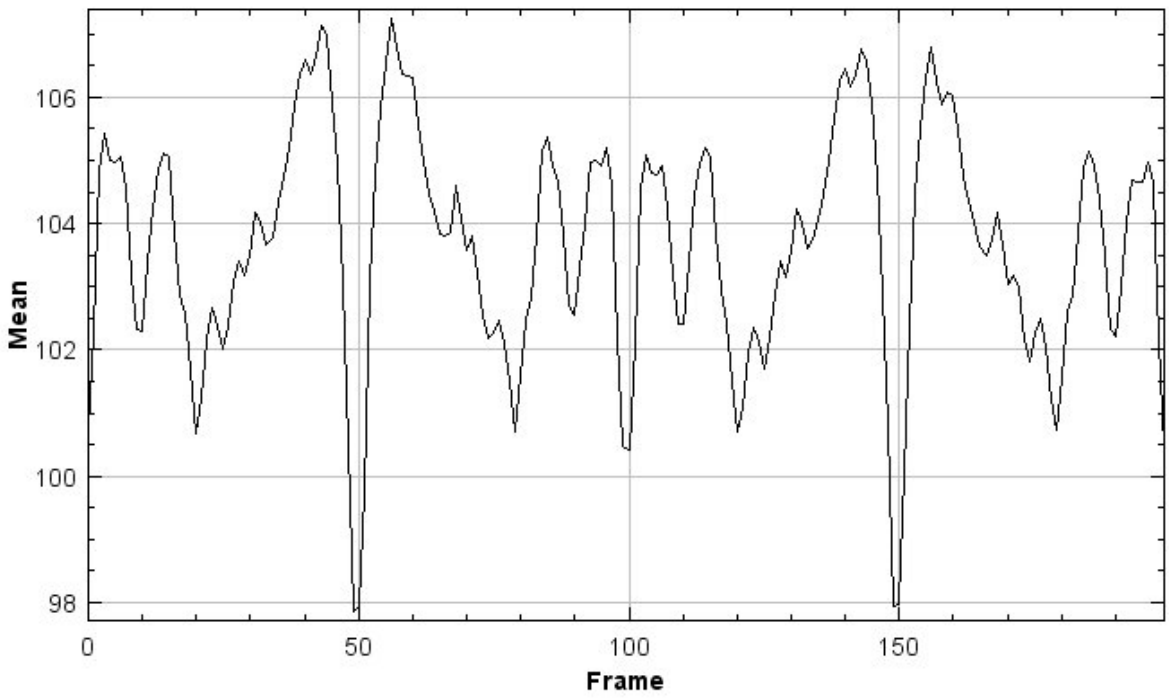

Figure 34. Test procedure of mean intensity across 4 volumes of 50 frames. The intensity across all the frames shows that the beads were focused nearly the entire run of the calibration map. The drop in mean intensity ~107 to ~98 is not nearly as great as the intensity drop across the hardware test. Exposure time was 5ms, galvo parameters = 32767-34019 (100µm). Volume time was 2.56 vol/sec.

Figure 34 shows that the calibration map was repeatable for both curves, meaning that it could scan multiple volumes of beads. The calibration shows that both curves have similar slopes but the best frames occurred at different axial positions corresponding with the galvo mirrors. Once the software calibration provided successful test runs on the beads, multiple tests runs of volumetric imaging were taken with the ETL in the system as described in Chapter 4.

Hardware Control

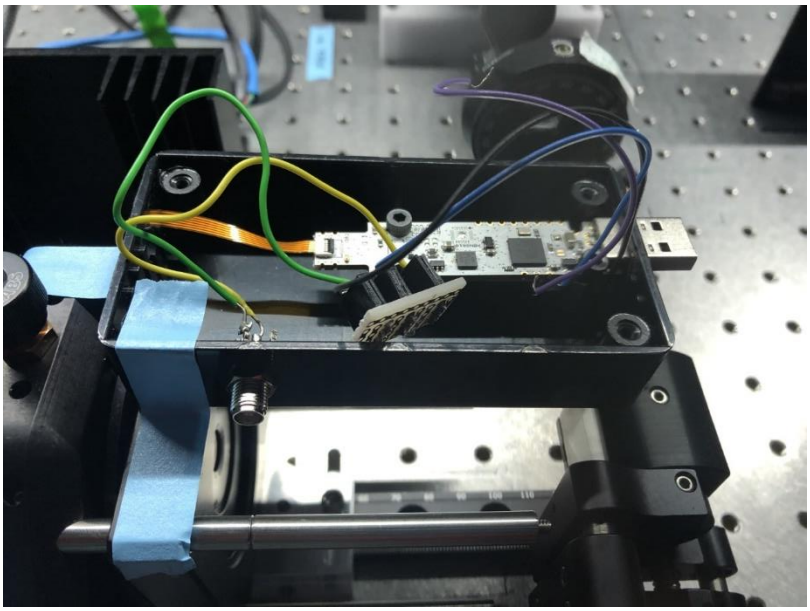

Figure 35. ETL USB driver opened for hardware access of voltages from DACboard.

The ETL can also be controlled by an analog input signal. This approach can potentially drive the ETL faster because it eliminates software delays. The software control results in delays due to the communication with the device and due to the step response of the ETL which much be accounted for each time the ETL position is changed. To send a hardware sinewave signal to the ETL, a BNC cable was used to deliver the needed voltage to the ETL. The ETL driver contained pins that could be soldered for hardware access (Figure 35) for 10-bit analog-to-digital conversion. This voltage was then converted from an analog signal into a digital signal through a built-in 12-bit ADC in the ETL driver. The ETL driver read the voltage into its software with the following conversion:

$$Analog\ Voltage = \frac{V_{in}}{5V}(1023),$$

where V_{in} is the input voltage into the ETL driver. Once the input voltage from the DAC board (Digilent, Analog Shield) is read, it can be mapped through the software. The mapping

feature allowed the device to use the analog voltage and relate a specific input into a current. The Optotune software required a minimum of 2 mapping points to function. For simplicity, all points were scaled from 0-1023 with 0 corresponding to the minimum current and 1023 corresponding to the maximum current. Having these two mapped positions ensured the tunable lens could be within specified boundaries. To understand the axial distance between these two boundaries, a calibration process would be needed to properly map the ETL.

ETL Hardware Sinewave Calibration

The ETL was placed in the system and the maximum and minimum boundaries were found by repeatedly moving both the galvo values and ETL values to correspond with it. When the beads were barely in focus, that point would be marked as the ETL and galvo boundaries. For example, the lower boundary for the ETL was 11.66mA, corresponding to a galvo position of 32178. The upper boundary of focus was the ETL at a value of 159.69mA, corresponding with a galvo setting of 34275. The ETL values were widened to allow the calibration method to sweep a wider range. For this example, they were changed to 4.76mA and 166.53mA. This was done to make sure the beads were in focus due to the best point being found by eye. A separate MATLAB code was used to generate a sine table with precise galvo and ETL currents.

We sent the generated sinewave voltages from our digital-to-analog (DAC) board to the ETL and galvo. This DAC board is the same board that controls the galvo mirrors with 16-bit voltage values. The ETL sinewave had a peak-to-peak amplitude of 1.12V (which was well under the Optotune ETL driver manual specified the voltage maximum of 5V). The advantage of sending a voltage from the DAC board was the ability to sync the timing of the galvo, ETL, and camera. This method used a sinewave to drive the ETL without encountering high frequency

components. This can be visualized in Figure 36. The black line represents the parked galvo laser.

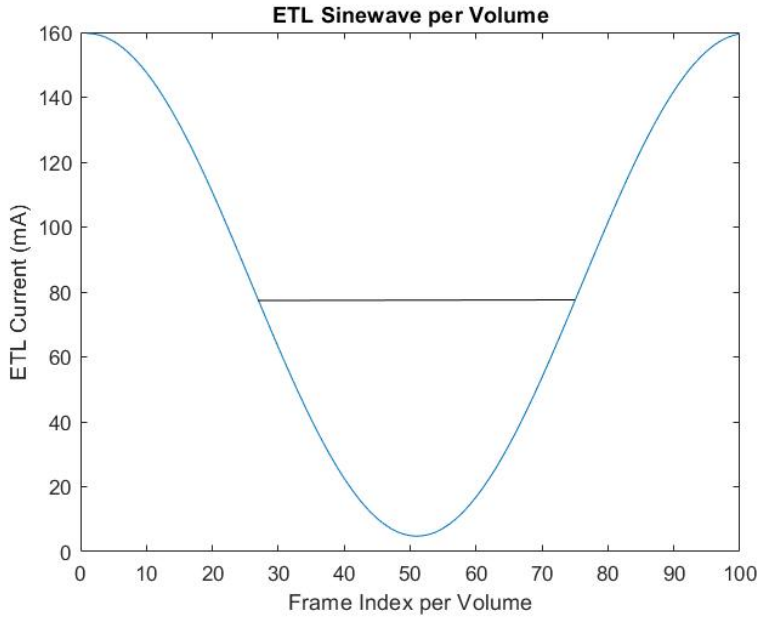

Figure 36. ETL sinewave displayed in current mode. Lower boundary = 4.76mA. Upper boundary = 166.53mA.

The Optotune mapping software (Figure 37) allows for precise current settings of analog inputs that would effectively create a map. To ensure the correct voltages were used for calibration, we connected an oscilloscope to the ETL to monitor the exact voltages being sent into the ETL (Figure 38).

Figure 37. Optotune ADC mapping table. This is an example of analog inputs being used for the mapping feature.

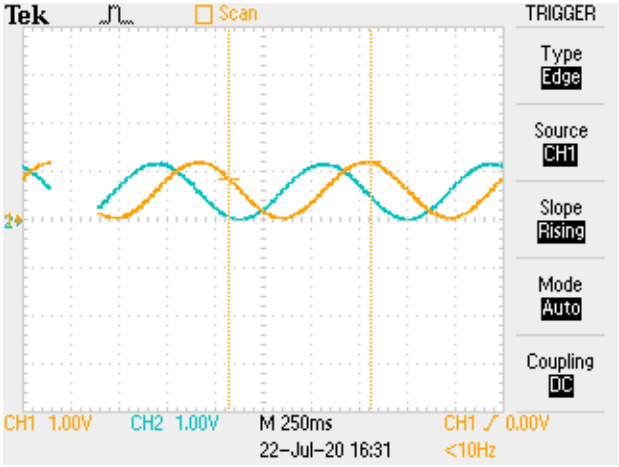

Figure 38. ETL (blue) and x-Galvo (orange) sinewaves generated from DAC board. Phase offset = ¾.

The hardware calibration showed the beads in focus for a portion of the sinewave cycle. Partial focus is undesirable due to photobleaching, phototoxicity, and the waste of light in the detection path from the mismatched focus and galvo position.

CHAPTER 4 - RESULTS

In this chapter, I will discuss the volumetric data acquired from the sinewave calibration maps described in Chapter 3. The volumetric bead data validated the axial range of the ETL could be achieve 167µm. This range proved to be more than enough distance to cover the CNS of zebrafish larvae, which could fit inside 100µm volumes. Volumetric data of zebrafish were taken across a FOV of 400 x 400 x 100µm^3 at a rate of 0.6Hz. The zebrafish data displayed in this chapter show that the 0.6Hz volumetric imaging rate was enough to capture the calcium expressions and provide 3D reconstruction.

Volumetric Bead Data Validation

We first took volumetric data of beads embedded in agar. The primary goal of these measurements was to ensure that the ETL's focus was at the beam waist of the light sheet at every plane of the volume. The second goal was to determine the axial range of volumetric imaging and determine the largest possible axial range of the microscope system. The goal of our system was to image the entire zebrafish CNS at a rate greater than 1 volume per second (1Hz).

The calibration described in chapter 3 was run with a sinewave and determined the linear relationship between ETL power and galvo position. A LabVIEW program was written to take the linear fit equations generated from the calibration map and drive the ETL focal power to the corresponding galvo points (Figure 39). The LabVIEW programed required an input of the galvo range so that the corresponding ETL focal powers could be generated from the linear fit.

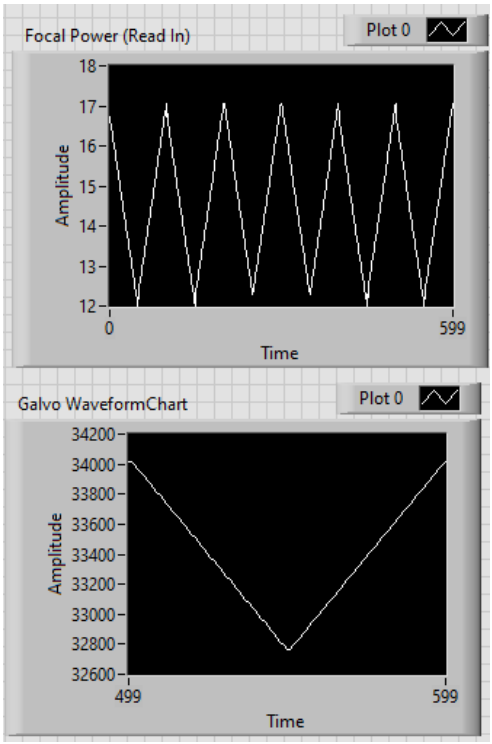

Figure 39. Triangle waves were used to drive the ETL and galvo. The galvo range was 100 microns (from 32767 to 34019 bits). These waves were built from the sinewave calibrated map.

One of the first calibration validity tests on the bead samples took place on a dense bead set (1:20 concentration). 4 volumes of 50 frames were acquired at a rate of 2.56 seconds per volume (0.39Hz) across a range of 100µm. Each frame took about 51ms to acquire. The camera exposure time for each frame was 5ms and the settling time for the ETL was 5ms. The software required 30ms per focal power adjustment. The remaining 11 milliseconds per frame were attributed to the time required for communication between the LabVIEW program and the lab equipment.

The images from this calibration test showed most of the beads in-focus for every frame. The left side of the frame in Figure 40 seems slightly out-of-focus because the ETL's aperture is misaligned with the detection axis due to the position of the CXY2 cage system. This calibration map that drove the ETL and galvo is shown in Figure 41.

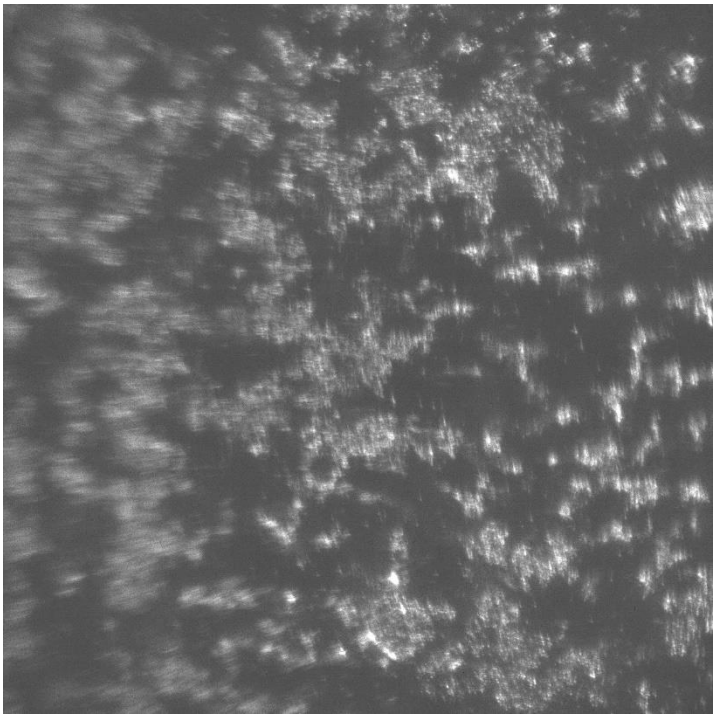

Figure 40. Frame 17 of 200 from 100µm volumetric bead test taken November 10, 2020. 4 volumes of 50 frames were acquired. Camera exposure time was 5ms. Volume time was 2.56 seconds per volume.

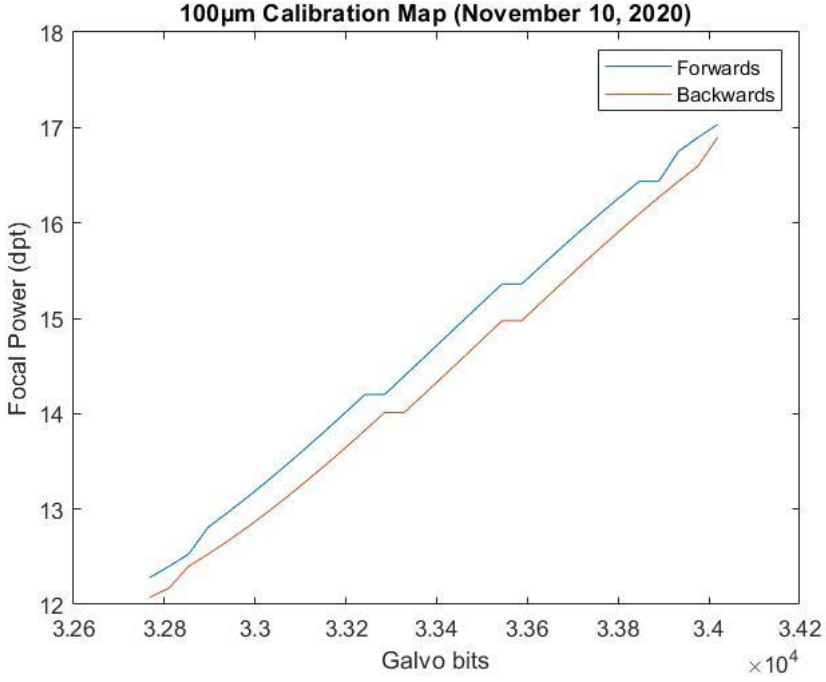

Figure 41. 100µm calibration map (November 10, 2020). X-axis is the galvo position in bits. Y-axis is the focal power in diopters.

The calibration map produced from the dense set of fluorescent beads showed a strong hysteresis (Figure 41). When the ETL was calibrated with a sparser bead sample (1:200 concentration), the hysteresis was reduced, and the linear calibration curves largely overlapped as seen in Figure 42. 4 volumes of 50 frames were taken across 167 µm. The volume acquisition time was about 1.8 seconds per volume (0.55Hz). The laser power was set to 20mW and the exposure time of the beads was set to 5ms. Although the frames, volumes, and exposure time parameters remained the same for the 167µm sample, the speed was increased by binning the pixels 4x4.

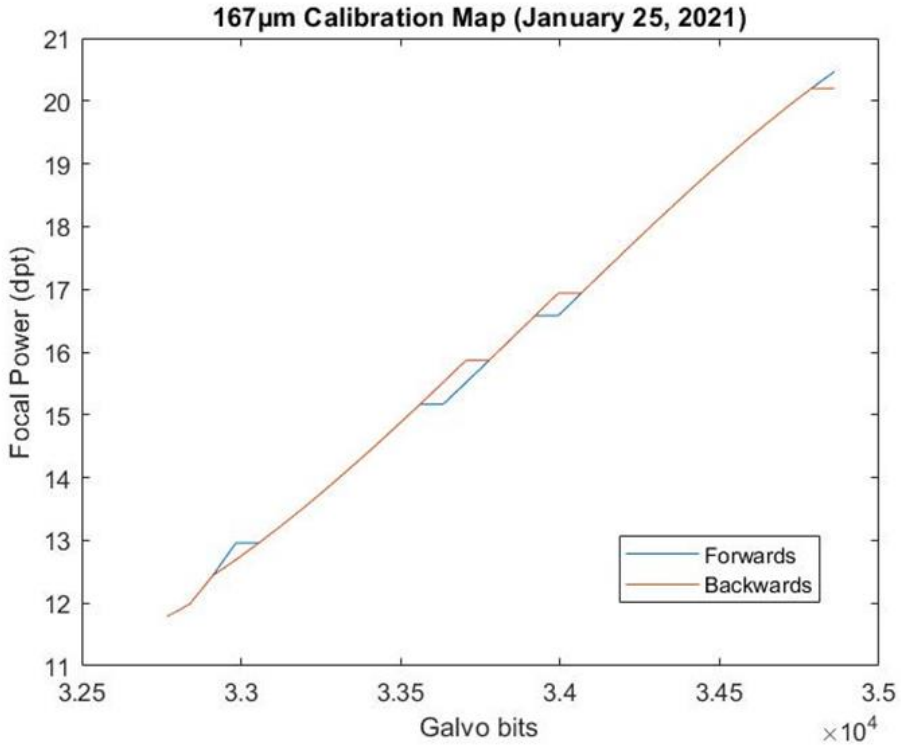

Figure 42. 167µm calibration map. The reduction of hysteresis is displayed by the near overlap of the forwards and backwards curves. Data taken on January 25, 2021.

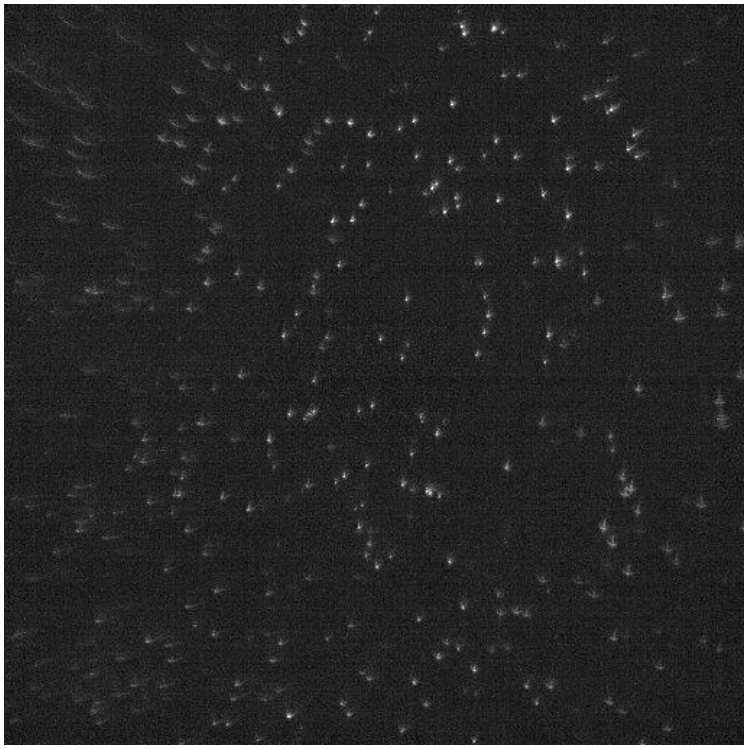

Figure 43. Frame 82 of 200 from 167µm bead calibration taken January 25, 2021. 4 volumes of 50 frames were acquired. Volume speed of 1.86 seconds per volume. Exposure time was 5ms per frame. Laser power was 20mW.

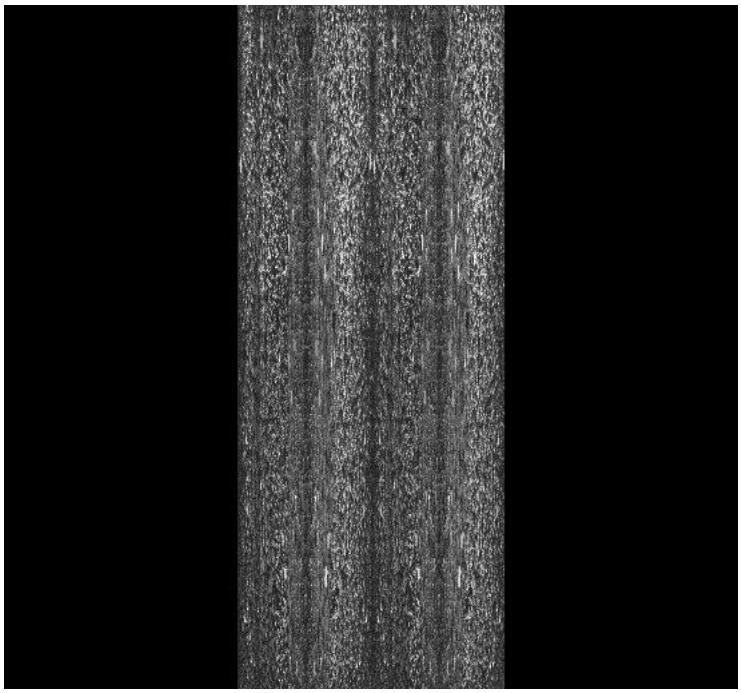

Figure 44. 3D Projection of sparse bead data. All 4 volumes displayed.

After these two volumetric bead validation tests, we learned that sparser bead samples provided better calibration maps. Another result of these tests was that the ETL's axial range limit was determined to be 167 µm. The theoretical range of the ETL in our system was calculated to be a range of 180 µm based on the ETL optical power assumptions from the Optotune manual. We were not able to achieve the full axial range due to the imposed boundary limits of the ETL software during calibration. The lower and upper limits of the calibration were respectively 9.77 and 22.16 diopters. When the focal power exceeded the boundaries, the software would give a warning that the focal power could not be constantly kept at the inputted focal power.

The acquisition of volumetric high-speed fluorescent bead data shows that the ETL could achieve a large scanning range of 167 µm. This range exceeds the average dimensions of the zebrafish larvae central nervous systems (CNS). In the next section, high-speed volumetric imaging will be applied to zebrafish larvae to capture neuronal seizure events occurring within the brain.

Volumetric Zebrafish Data

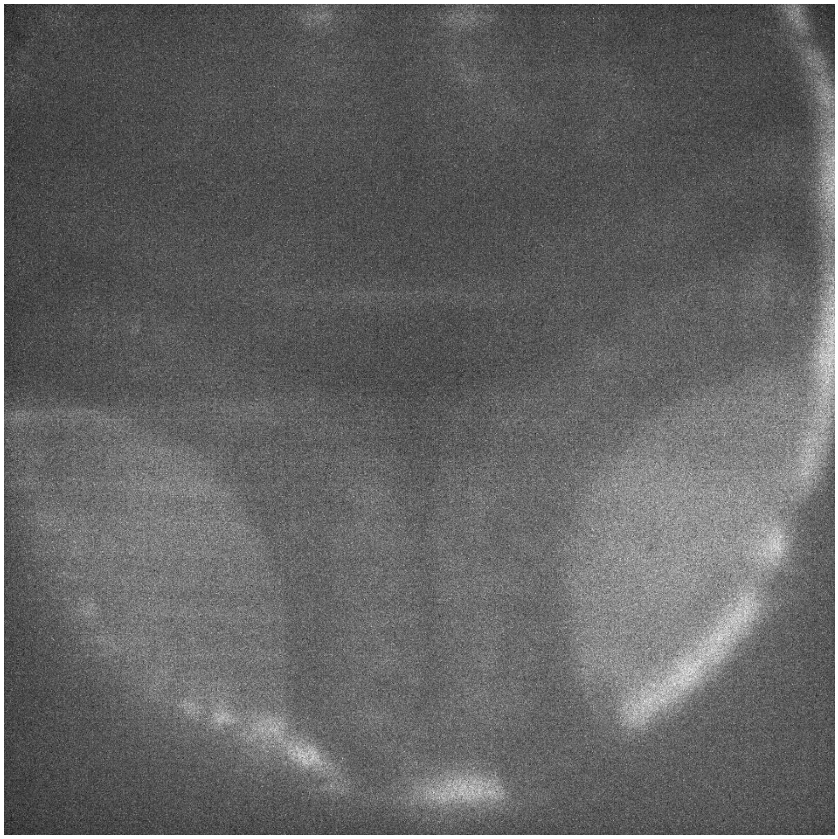

Figure 45. Frame 17 of 30 from ETL zebrafish volume. Volume was scanned 100µm with a step size of 3.44 µm. Four volumes of 30 frames were captured with a 40ms exposure time for the camera.

*Figure 45. Frame 17 of 30 from ETL zebrafish volume. Volume was scanned 100µm with a step size of 3.44 µm. Four volumes of 30 frames were captured with a 40ms exposure time for the camera.*Figure 45 shows a single frame from one of the first zebrafish volumes acquired with the ETL. The volume spanned a 100µm axial sweep along the z-axis with a spacing of 3.4 microns between planes. 4 volumes were taken at a rate of 2.7 seconds per volume (0.37Hz). A long image exposure time of 40ms was used to increase the signal because the fish have much lower fluorescence intensity than the bead samples. A potential reason for the fish being so dim was that it possibly died during the mounting and transferring process.

A different and brighter zebrafish (Figure 46) was used to observe large datasets of neuronal activity. This zebrafish was imaged for 1125 volumes with 30 frames per volume. Each volume was acquired at a rate of 1.6 seconds per volume (0.6Hz). The step size between each frame was 3.4µm and the lateral field of view of each frame was 400 x 400 microns^2 (1024x1024 pixels). Each volume spanned 100µm along the detection axis. A laser power of 20mW and camera exposure time of 20ms were used to capture this volume.

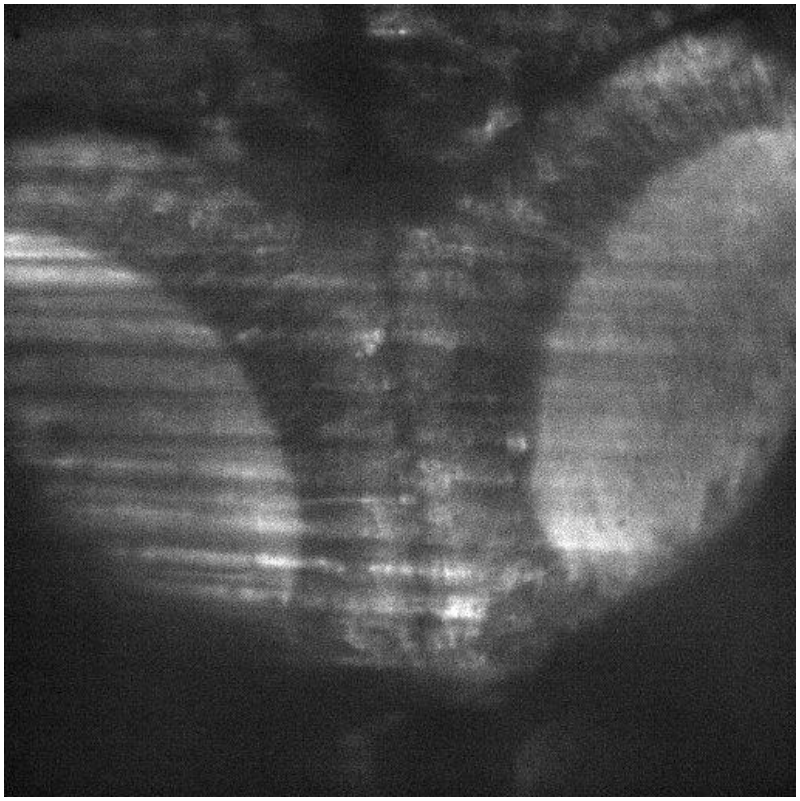

Figure 46. A 400 µm x 400 µm (1024 x 1024 pixels) frame of a zebrafish larvae. Bright neuronal structures can be seen connected to the eyes. 1125 volumes of 30 frames were recorded at a rate of 1.6 seconds per volume (0.6Hz) across 100µm. Laser was set to 20mW and exposure time was 20ms per frame.

A 3D reconstruction of the fish in Figure 46 can be seen in Figure 47. The frame in this figure was the first one acquired in the volumetric stack. The 20mW laser provided the immediate bright neuronal events as seen in the figure.

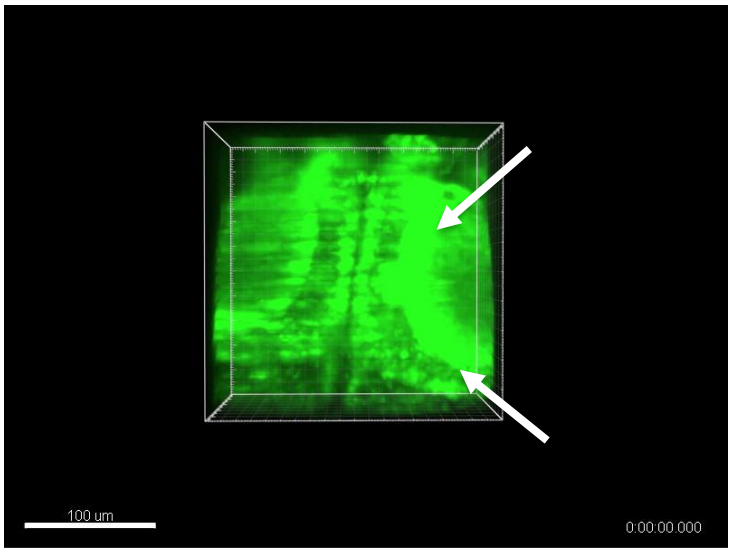

Figure 47. First frame of zebrafish capture. White arrows point to neuronal events (the bright/excited portions of the fish). This frame was captured as the laser excited the zebrafish larvae. The 100 µm scale bar is for reference. 1125 volumes of 30 frames were recorded at a rate of 1.6 seconds per volume (0.6Hz) across 100µm. Laser was set to 20mW and exposure time was 20ms per frame.

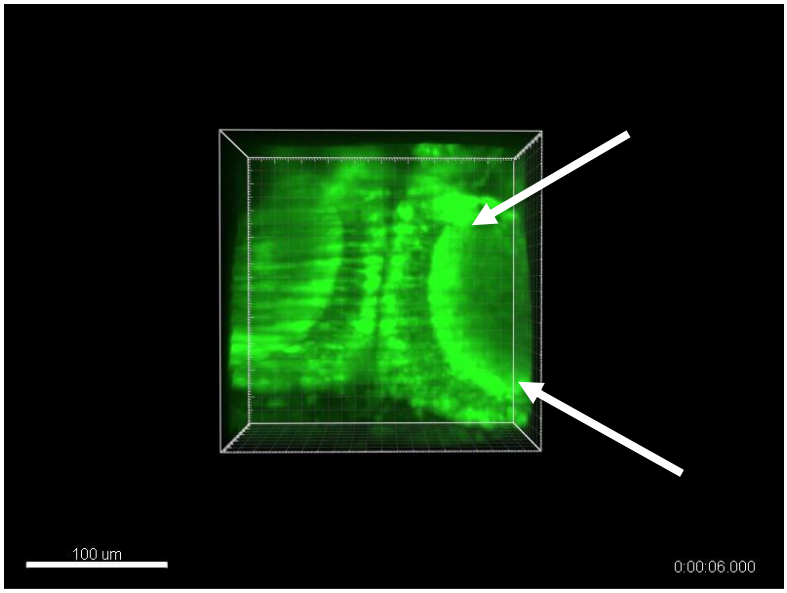

Figure 48. 6 minutes after the first image capture. The initial brightness of the fish diminishes after the beginning of the laser excitation. White arrows point to areas where the initial neuronal activity dimmed. 1125 volumes of 30 frames were recorded at a rate of 1.6 seconds per volume (0.6Hz) across 100µm. Laser was set to 20mW and exposure time was 20ms per frame.

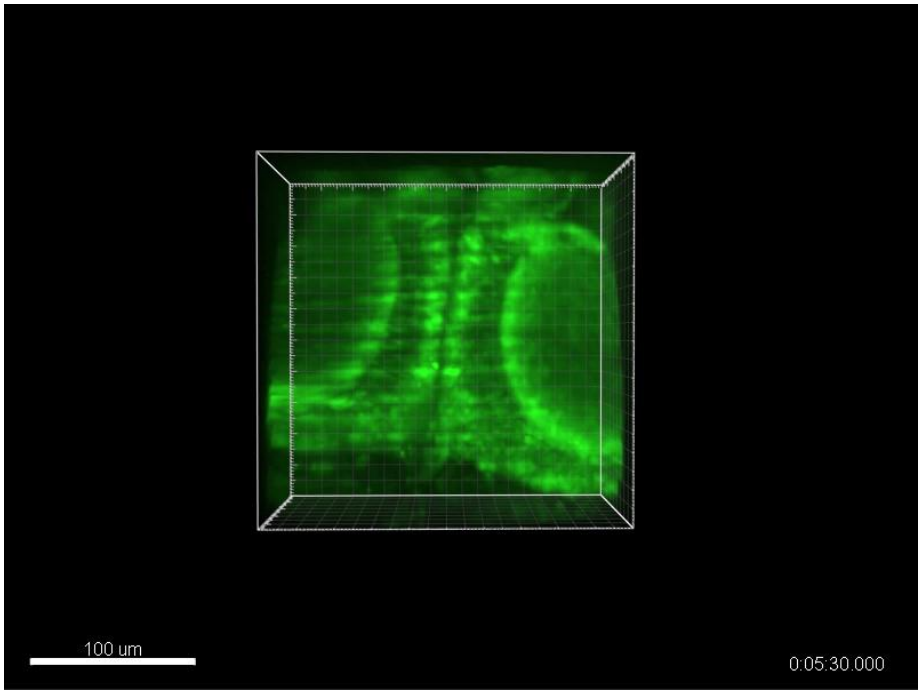

Figure 49. Zebrafish neuronal events imaged 5 minutes and 30 seconds after initial capture.

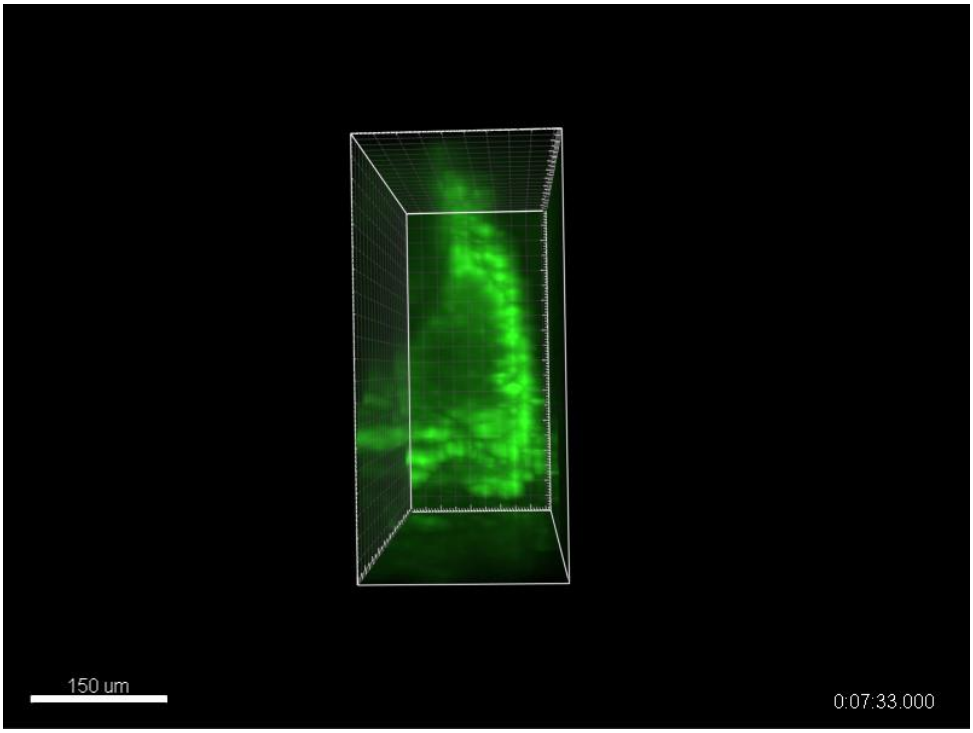

Figure 50. Side view of 3D reconstructed zebrafish larvae. Scale bar is for comparison.

Volumetric Plane Validation Analysis

To confirm the ETL was calibrated correctly, we compared the volumetric dataset taken with the ETL to the volumetric dataset acquired with the stage moving the sample throughout the detection objective's focal plane. To analyze the data, a 2D normalized cross-correlation analysis was used on the fish volumes. This analysis would take a user-defined subset of pixels (Figure 52) from a reference volume (stage movement volume) and compare them to ETL volume. The goal of the cross-correlation analysis was to relate the ratio of step sizes from the two acquisitions accurately. The stage movement volume had a step size of 1.5μm and the ETL volume had a step size of 3.44μm. The ratio of these step sizes is $\frac{1.50}{3.44} = 0.436$, so for every step taken in the reference volume, the ETL volume would move 0.436 steps.

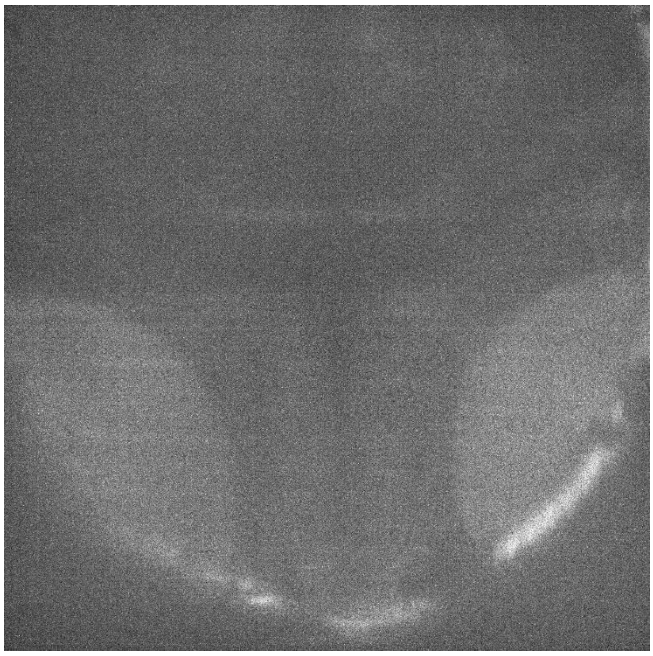

Figure 51. Frame 29 of 62 from the volume acquired by moving the 4D stage. Step size is 1.5μm per frame. The frame shown corresponds to 42μm axial translation from the first frame.

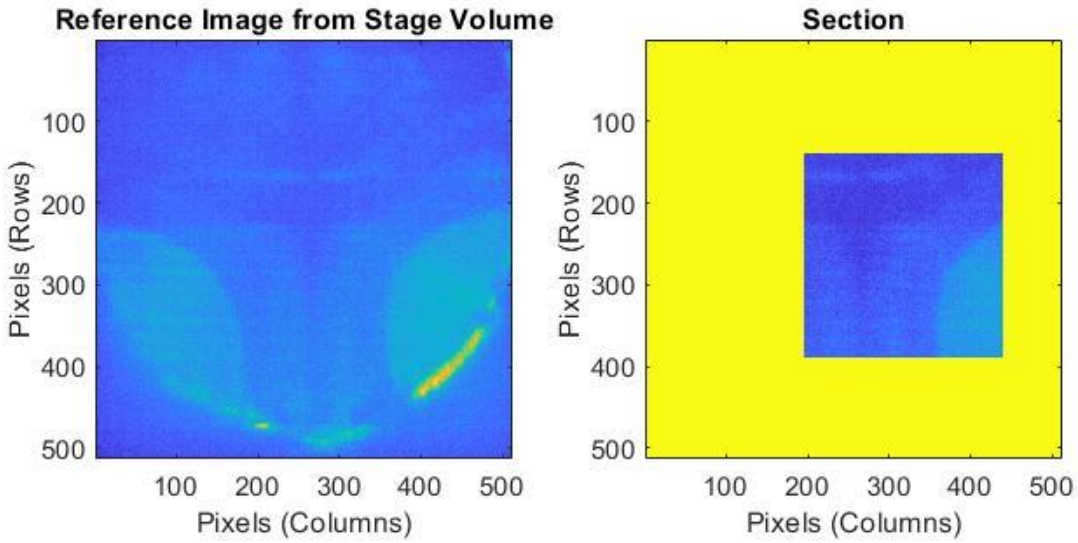

Figure 52. Reference image and subsection for 2D normalized cross correlation analysis. In this photo, frame 29 (and its corresponding subsection) of the reference volume can be seen here. The subsection of pixels was composed of rows 140-388 and columns 197-440.

As Figure 52 shows, frame 29 from the static stack of images was used for comparison. The whole frame of each image (from both the static stack and ETL) were scaled to 512x512 pixels. Each subsection from the reference volume, which was 244x249 pixels large, was compared against 50 frames of the 512x512 images from the ETL volume. The resulting matrix, which in this case was 755x760 pixels, can be seen in Figure 53 and Figure 54.

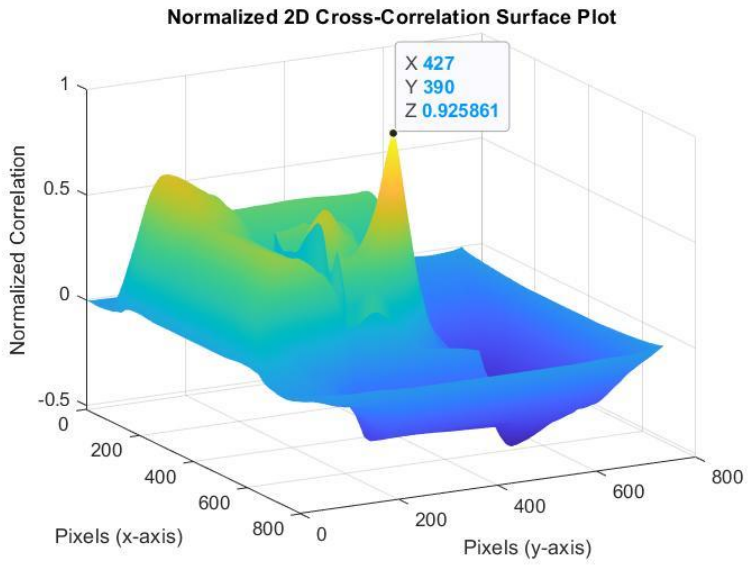

Figure 53. Normalized cross-sectional analysis surface plot from a 3D perspective. Maximum normalized cross-correlation value is 0.925861. This surface plot shows analysis between reference image 40 and ETL image 21.

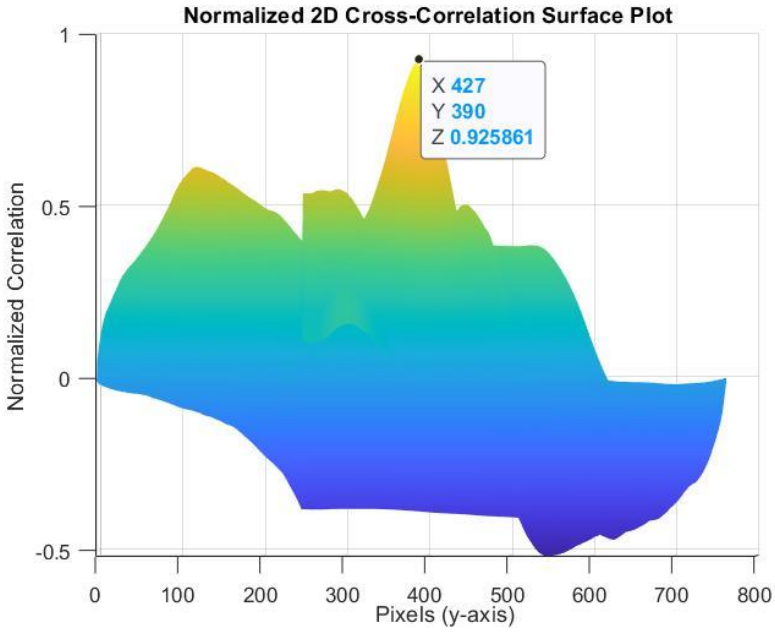

Figure 54. Normalized cross-sectional analysis surface plot from a 2D perspective. Maximum normalized cross-correlation value is 0.925861. This surface plot shows analysis between reference image 40 and ETL image 21.

The highest normalized peak value of 0.925861 and its location have been noted in

Figure 53 & Figure 54. All the correlation data was compiled into a plot that took the frame

index of the matching reference subsection and graphed it with the ETL frame index that corresponded with it. The frame index correlation plot (Figure 55) shows the graphical comparison of step sizes. The slope of 0.4331 nearly matches the step size ratio $\left(\frac{1.50}{3.44} = 0.436\right)$ of the two methods.

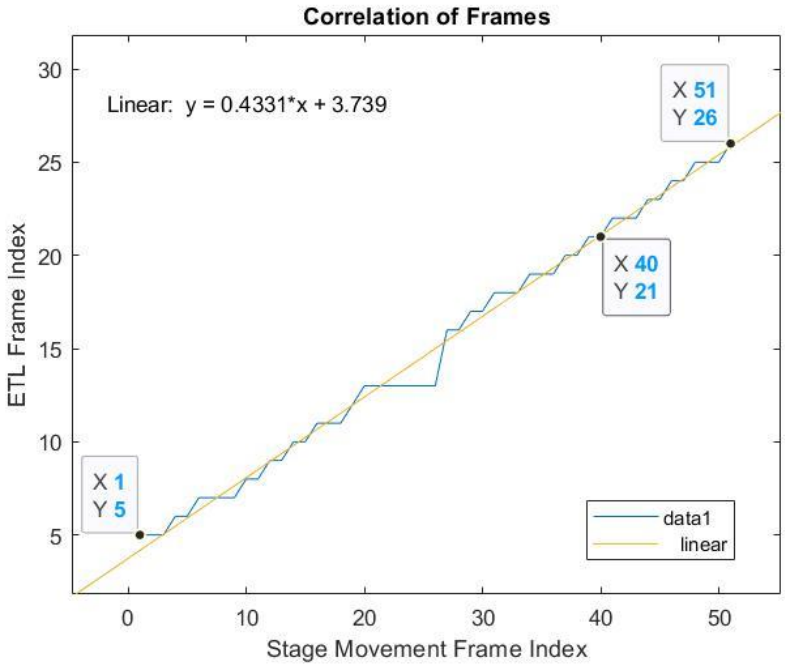

Figure 55. Correlation of all frames. Each image consisted of 512x512 pixels. The subsection was taken from rows 140-388 and columns 197-440. The slope of the correlation is nearly identical to the ratio of the step sizes (1.5/3.44 = 0.436).

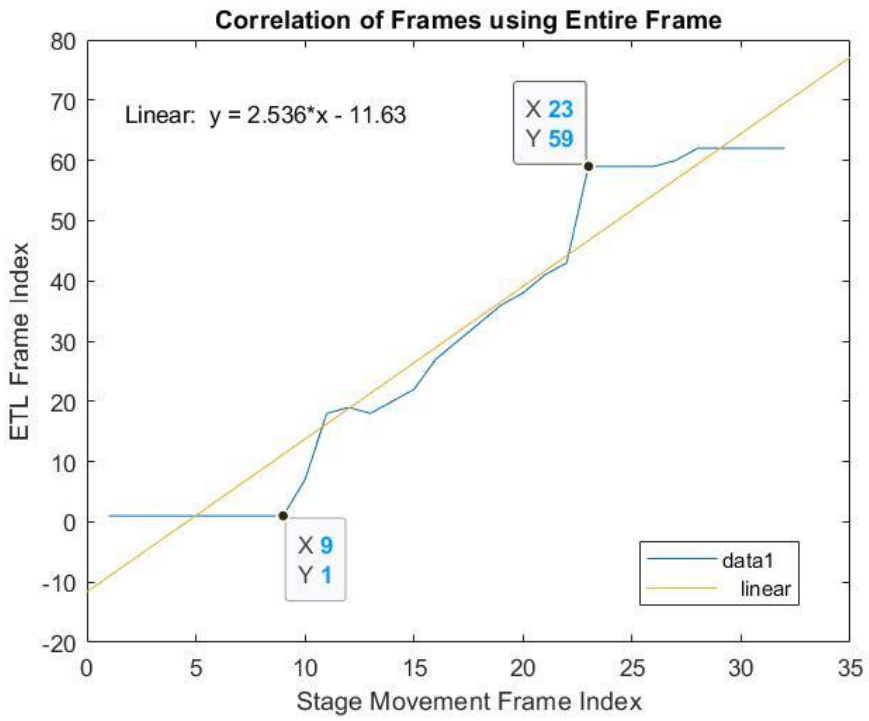

Figure 56. The correlation of all reference frames applied all ETL frames.

No subsection was used for analysis. Another normalized 2D cross-correlation analysis was applied to the same fish dataset, but this time the entire frame was analyzed instead of subsections. The whole-frame analysis did not provide the same slope as the analysis with subsections. The whole frame analysis did not work as well because the MATLAB® function [45] could not generate matrices with meaningful normalizations when the images were large.

CHAPTER 5 - DISCUSSION

The goal of this thesis project was to capture high-speed volumetric imaging over a wide field of view for the purpose of studying neuronal events in a zebrafish for biological analysis. The ETL that was placed within the system increased the volumetric imaging speed of the light sheet microscope from 0.147Hz (40 frames, 20ms exposure time, 150ms stage time) to 0.6Hz over a field of view of 400 x 400 x 100μm^3 (1024 x 1024 pixels). The addition of the ETL added the ability to capture volumetric images fast enough to observe neuronal activity throughout the zebrafish larvae.

Several factors such as the number of image planes, axial steps, and pixels contributed to the volumetric imaging rate. Although other systems have achieved faster volumetric imaging rates, it should be noted that our system used more pixels and more slices per volume than most of the volumetric imaging methods listed in Table 1. The extra pixels and smaller step size were used to achieve decent optical sectioning of the neuronal activity. Table 1 lists the volumetric factors that compare our lab group with the work of others.

Group	Axial Range, Δz (μm)	Number of Frames	Distance between frames(μm)	Frame Size(μm^2)	Frame size (Pixels)	Speed	Exposure Time per frame (ms)
Kner Advance Imaging Lab	100	30	3.4	400 x 400	1024 x 1024 = 1048576	0.6Hz	20
Huisken (ETL) [30]	~92.8	17	5.8	218 x 148	600 X 408 = 244800	30Hz	1.96
Keller (2013) [27]	200	41	5	800 × 600	617 x 247 = 152,399	0.8Hz	5
Loza-Alvarez et al. [46]	44	22	2.09	~75 x 50	2048 x 128 = 262144	73Hz	0.623

Table 1. Volumetric Comparison among Kner, Huisken, Keller, and Loza-Alvarez lab groups. The axial range, number of frames, spacing between frames, frame size, speed, and exposure time are listed for comparison.

The axial range of a volume is one of the most important aspects of volumetric imaging because it defines how far the microscope focus must be shifted. This parameter is dependent upon the size of the specimen or structure being observed. For example, the 100µm axial range our lab group used was appropriate for imaging the zebrafish brain. In the Loza-Alvarez group's work, a smaller range of 44µm was appropriate for tracking the trajectories of several microbeads (1µm in diameter) throughout the volume [46].

The step size between each image is another important factor for volumetric imaging. For decent optical sectioning of the zebrafish brain, we chose a spacing between the frames of 3.4µm. For comparison, the Huisken group's 2013 ETL paper called for a relatively large spacing of 5.8 µm. This wide distance between planes was used because their group was observing a beating zebrafish heart. Because the blood cells and muscle cells inside the heart could be discerned without fine axial spacing, the distance between frames could remain large and the images could be reconstructed properly. On the other hand, neurons and smaller biological structures require a smaller step distance between frames to avoid leaving out the structures between frames. For instance, the Keller group achieved cellular imaging across the brain of their zebrafish by stepping each plane 5µm [27]. The average diameter of the cells in the CNS was 6.62 ± 0.14µm, mean ± s.e.m., n = 298, while the light sheet thickness was 4.25 ± 0.80 µm [27]. Although their step size and light sheet thickness were more than double the average diameter, the Keller group was mostly able to discern neurons within one optical section due to the fish being highly transparent [27]. Another caveat to consider about step sizes is the settling time that comes with it. The Keller group mechanically moved their objective lens and needed

30ms to allow the objective lens to stop moving. This settling time can slow down the volumetric imaging rate if many planes are required.

The number of pixels used for imaging can also affect the volume acquisition time. Using more pixels to capture an image takes more time because a larger sensing area is being used. To illustrate this idea, consider the Loza-Alvarez group's rapid image acquisition approach. This group was able to achieve a fast imaging speed of 73Hz to capture images of beads, but they did so by cutting down the amount of pixels being captured. Since this group used their microscope for bead tracking, their approach of using fewer pixels was appropriate. The number of pixels directly translates to the size of the FOV. When fewer pixels are being used, the FOV is smaller. Our microscope was able to image a large FOV with many pixels.

We plan to make improvements to our light sheet microscope system to optimize its performance for speed. The ETL was driven by LabVIEW and the software communicated with the ETL driver through a USB cable connected to the computer's COM port. The LabVIEW custom coded software took between 50 and 57ms to capture each frame in the volume acquired at 0.6Hz. The camera exposure time was set to 20ms. A wait time of 5ms was imposed to make sure the ETL and galvo could remain in sync. In addition to the wait time, it took up to 25ms to update the focal power of the ETL. The last 5-7ms was attributed to the data communication between the ETL and computer not being optimized. The speed of the ETL can be improved by driving it with a hardware signal from the DACboard. The speed of our microscope can be improved by demagnifying the image plane in the detection path of our system onto a smaller area of our high-speed camera. Cutting down the number of pixels needed for image capture would allow the system to also speed up. The addition of the ETL to the light sheet microscope

has greatly increased the volumetric acquisition performance and additional improvements are highly desired for better biological data.

REFERENCES

[1] P. A. Santi, "Light Sheet Fluorescence Microscopy: A Review," *Journal of Histochemistry & Cytochemistry,* vol. 59, no. 2, pp. 129-138, 2011.

[2] P. J. Keller and H.-U. Dodt, "Light sheet microscopy of living or cleared specimens," *Current Opinion in Neurobiology,* vol. 22, no. 1, pp. 138-143, 2011.

[3] A. V. Kalueff, A. M. Stewart and R. Gerlai, "Zebrafish as an emerging model for studying complex brain disorders," *Trends in Pharmacological Sciences,* vol. 35, no. 2, pp. 63-75, February 2014.

[4] J. Liu and S. C. Baraban, "Network Properties Revealed during Multi-Scale Calcium Imaging of Seizure Activity in Zebrafish," *eNeuro,* vol. 6, no. 1, 2019.

[5] J. W. Lichtman and J.-A. Conchello, "Fluorescence microscopy," *Nature Methods,* vol. 2, no. 12, pp. 910-919, 2005.

[6] J. Andilla, O. E. Olarte, E. J. Gualda and P. Loza-Alvarez, "Light-sheet microscopy: a tutorial," *Advances in Optics and Photonics,* pp. 111-179, 2018.

[7] R. Rottenfusser, E. E. Wilson and M. W. Davidson, "Introduction to Fluorescence Microscopy," ZEISS, [Online]. Available: http://zeiss-campus.magnet.fsu.edu/print/basics/fluorescence-print.html. [Accessed 5 November 2020].

[8] T. Terai and T. Nagano, "Small-molecule fluorophores and fluorescent probes for bioimaging," *Pflügers Archiv-European Journal of Physiology,* vol. 465, no. 3, pp. 347-359, 2013.

[9] R. M. Hoffman, "Advantages of multi-color fluorescent proteins for whole-body and in vivo cellular imaging," *Journal of Biomedical Optics,* vol. 10, no. 4, 2005.

[10] M. Gu, Advanced Optical Imaging Theory, Springer, 2000.

[11] M. Abramowitz and M. W. Davidson, "Anatomy of a Microscope - Image Formation," Olympus, [Online]. Available: https://www.olympus-lifescience.com/fr/microscope-resource/primer/anatomy/image/. [Accessed 26 October 2020].

[12] J. W. Goodman, Introduction to Fourier optics, 2nd Edition ed., New York: McGraw-Hill, 1996.

[13] "Capturing images," [Online]. Available: http://microscopy.berkeley.edu/courses/dib/sections/02Images/sampling.html. [Accessed 26 January 2021].

[14] E. H. K. Stelzer, "Contrast, resolution, pixelation, dynamic range and signal-to-noise ratio: fundamental limits to resolution in fluorescence light microscopy," *Journal of Microscopy,* vol. 189, no. 1, pp. 15-24, 1998.

[15] Hamamatsu, "Resources," 1 March 2012. [Online]. Available: https://www.hamamatsu.com/resources/pdf/sys/e_flash4_whitepaper.pdf. [Accessed 13 December 2020].

[16] S. E. Webb, Y. Gu, J. S. Lévêque-Fort, M. J. Cole, K. Dowling, R. Jones, P. M. French, M. A. A. Neil, R. Juškaitis, L. O. D. Sucharov, T. Wilson and M. J. Lever, "A wide-field time-

domain fluorescence lifetime imaging microscope with optical sectioning," *Review of Scientific Instruments,* vol. 73, no. 4, pp. 1898-1907, 2002.

[17] J. Huisken and D. Y. R. Stainier, "Selective plane illumination microscopy techniques in developmental biology," *Development,* vol. 136, no. 12, pp. 1963-1975, 2009.

[18] V. Centonze and J. B. Pawley, Tutorial on practical confocal microscopy and use of the confocal test specimen, Boston, Massachusetts: Springer, 2006, pp. 627-649.

[19] J. Jonkman, C. M. Brown and R. W. Cole, "Quantitative confocal microscopy: Beyond a pretty picture," *Methods in cell biology,* vol. 123C, pp. 113-134, 06 2014.

[20] S. Choi, P. Kim, R. Boutilier, M. Y. Kim, Y. J. Lee and H. Lee, "Development of a high speed laser scanning confocal microscope with an acquisition rate up to 200 frames per second," *Optics Express,* vol. 21, no. 20, pp. 23611-23618, 2013.

[21] S. M. Choi, W. H. Kim, D. Côté, C.-W. Park and H. Lee, "Blood cell assisted in vivo Particle Image Velocimetry using the confocal laser scanning microscope," *Optics Express,* vol. 19, no. 5, pp. 4357-4368, 2011.

[22] C. J. Engelbrecht and E. H. K. Stelzer, "Resolution enhancement in a light-sheet-based microscope (SPIM)," *Optics Letters,* vol. 31, no. 10, pp. 1477-1479, 15 May 2006.

[23] J. Wu, J. Li and R. K. Chan, "A light sheet based high throughput 3D-imaging flow cytometer for phytoplankton analysis," *Optics Express,* vol. 21, no. 12, pp. 14474-14480, 10 June 2013.

[24] J. Icha, M. Weber, J. C. Waters and C. Norden, "Phototoxicity in live fluorescencemicroscopy, and how to avoid it," *BioEssays,* vol. 39, no. 8, pp. 1-15, 27 07 2017.

[25] A. Kaufmann, M. Mickoleit, M. Weber and J. Huisken, "Multilayer mounting enables long-term imaging of zebrafish development in a light sheet microscope," *Development,* vol. 139, no. 17, pp. 3242-3247, 14 June 2012.

[26] L. Godinho, "Live Imaging of Zebrafish Development," *Cold Spring Harbor Protocols,* pp. 770-777, 2011.

[27] M. B. Ahrens, M. B. Orger, D. N. Robson, J. M. Li and P. J. Keller, "Whole-brain functional imaging at cellular resolution using light-sheet microscopy," *Nature Methods,* vol. 10, no. 5, pp. 413-420, 18 03 2013.

[28] J. Swoger, M. Muzzopappa, H. López-Schier and J. Sharpe, "4D retrospective lineage tracing using SPIM for zebrafish organogenesis studies," *Journal of Biophotonics,* vol. 4, no. 1-2, pp. 122-134, 2011.

[29] S. Kumar, D. Wilding, M. B. Sikkel, A. R. Lyon, K. T. MacLeod and C. Dunsby, "High-speed 2D and 3D fluorescence microscopy of cardiac myocytes," *Optics Express,* vol. 19, no. 15, pp. 13839-13847, 2011.

[30] F. O. Fahrbach, F. F. Voigt, B. Schmid, F. Helmchen and J. Huisken, "Rapid 3D light-sheet microscopy with a tunable lens," *Optical Society of America,* vol. 21, no. 18, pp. 21010-21026, 30 August 2013.

[31] M. Weber, M. Mickoleit and J. Huisken, "Chapter 11 Light sheet microscopy," *Methods in Cell Biology Quantitative Imaging in Cell Biology,* vol. 123, pp. 193-215, 2014.

[32] R. Candelier, T. Panier, S. Romano, R. Olive, T. Pietri, G. Sumbre and G. Debrégeas, "Fast functional imaging of multiple brain regions in intact zebrafish larvae using Selective Plane Illumination Microscopy," *BMC Neuroscience,* vol. 14, pp. 1-11, 2013.

[33] J. Huisken and D. Y. Stainier, "Even fluorescence excitation by multidirectional selective plane illumination microscopy (mSPIM)," *Optics Letters,* vol. 32, no. 17, pp. 2608-2610, 2007.

[34] L. Tao, J. D. Lauderdale and A. T. Sornborger, "Mapping functional connectivity between neuronal ensembles with larval zebrafish transgenic for a ratiometric calcium indicator," *Frontiers in neural circuits,* vol. 5, 2011.

[35] K. Bergmann, P. M. Santoscoy, K. Lygdas, Y. Nikolaeva, R. B. MacDonald, V. T. Cunliffe and A. Nikolaev, "Imaging Neuronal Activity in the Optic Tectum of," *Journal of developmental biology,* vol. 6, no. 1, pp. 1-14, 2018.

[36] J. Huisken, J. Swoger, F. Del Bene, J. Wittbrodt and E. H. K. Stelzer, "Optical Sectioning Deep Inside Live Embryos by Selective Plane Illumination Microscopy," *SCIENCE,* vol. 305, no. 5686, pp. 1007-1009, 2004.

[37] M. B. Ahrens, M. B. Orger, D. N. Robson, J. M. Li and P. J. Keller, "Whole-brain functional imaging at cellular resolution using light-sheet microscopy," *Nature Methods,* vol. 10, no. 5, pp. 413-420, 2013.

[38] P. Annibale, A. Dvornikov and E. Gratton, "Electrically tunable lens speeds up 3D orbital tracking," *Biomed. Opt. Express* , vol. 6, no. 6, pp. 2181-2190, 2015.

[39] "GVSM002-US," 24 October 2019. [Online]. Available: https://www.thorlabs.com/drawings/4db17f732887f1ce-EF4E5631-916D-D07D-F3841EB980C0B97E/GVSM002-US-GalvanometerManual.pdf. [Accessed 17 February 2021].

[40] K. Keomanee-Dizon, S. E. Fraser and T. V. Truong, "A versatile, multi-laser twin-microscope system for light-sheet imaging," *Review of Scientific Instruments,* vol. 91, no. 5, 27 May 2020.

[41] Boston Micromachines Corporation, "Standard Deformable Mirrors," [Online]. Available: https://bostonmicromachines.com/standard-deformable-mirrors/. [Accessed 4 April 2021].

[42] Optotune, "EL-10-30-TC-Lens," [Online]. Available: https://www.optotune.com/el-10-30-tc-lens. [Accessed 9 February 2021].

[43] Optotune, "EL-10-30-TC Lens Driver 4 Manual," Optotune, [Online]. Available: https://www.optotune.com/el-10-30-tc-lens.

[44] Optotune, "EL-10-30-TC," 2019.

[45] MathWorks, "normxcorr2," [Online]. Available: https://www.mathworks.com/help/images/ref/normxcorr2.html.

[46] O. E. Olarte, J. Andilla, D. Artigas and P. Loza-Alvarez, "Decoupled illumination detection in light sheet microscopy for fast volumetric imaging," *Optica ,* vol. 2, no. 8, pp. 702-705, 2015.

[47] Y. Liu, S. Dale, R. Ball, A. J. VanLeuven, A. Sornborger, J. D. Lauderdale and P. Kner, "Imaging neural events in zebrafish larvae with linear structured illumination light sheet fluorescence microscopy," *Neurophoton,* vol. 6, no. 1, 5 March 2019.

[48] M. Weber, M. Mickoleit and J. Huisken, "Multilayer Mounting for Long-term Light Sheet Microscopy of Zebrafish," *Journal of Visualized Experiments,* no. 84, pp. 1-8, 27 February 2014.

[49] A. Graves and A. Schlaeppi, "Sample Mounting," WordPress, [Online]. Available: https://involv3d.org/sample-mounting/. [Accessed 29 March 2021].

[50] R. Rottenfusser, E. E. Wilson and M. W. Davidson, "Education in Microscopy and Digital Imaging," [Online]. Available: http://zeiss-campus.magnet.fsu.edu/articles/basics/resolution.html. [Accessed 18 June 2020].

[51] B. O. Leung and K. C. Chou, "Review of Super-Resolution Fluorescence Microscopy for Biology," *Applied Spectroscopy*, vol. 65, no. 9, pp. 967-980, 29 June 2011.

[52] D. J. Stephens and V. J. Allan, "Light Microscopy Techniques for Live Cell Imaging," *Science*, vol. 300, no. 5616, pp. 82-86, 4 April 2003.

[53] N. D. Lawson and B. M. Weinstein, "In Vivo Imaging of Embryonic Vascular Development Using Transgenic Zebrafish," *Developmental Biology*, vol. 248, no. 2, pp. 307-318, 15 August 2002.

[54] D. Semwogerere and E. R. Weeks, "Confocal Microscopy," *Encyclopedia of biomaterials and biomedical engineering*, vol. 23, pp. 1-10, 2005.

[55] S.-i. Higashijima, M. A. Masino, G. Mandel and J. R. Fetcho, "Imaging neuronal activity during zebrafish behavior with a genetically encoded calcium indicator," *Journal of neurophysiology*, vol. 90, no. 6, pp. 3986-3997, 2003.

[56] R. Heintzmann, "Band Limit and Appropriate Sampling in Microscopy," in *Cell Biology (Third Edition)*, vol. 3, J. E. Celis, Ed., Academic Press, 2006, pp. 29-36.

[57] Y. Liu, S. Dale, R. Ball, A. J. VanLeuven, A. Sornborger, J. D. Lauderdale and P. Kner, "Imaging neural events in zebrafish larvae with linear structured illumination light sheet fluorescence microscopy," *Neurophotonics*, vol. 6, no. 1, p. 015009, 2019.

APPENDIX

Appendix A

Ray Tracing Rules

CSEE 4530 Introduction to Optical Engineering

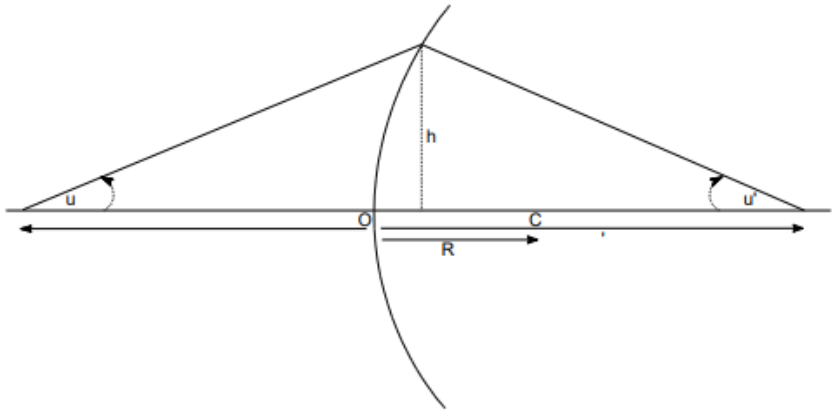

Ray tracing formulas

$$n_i' u_i' - n_i u_i = -h_i c_i (n_i' - n_i)$$

$$h_{i+1} = h_i + d u_i'$$

$$u_{i+1} = u_i'$$

Sign Conventions:

1. Unless otherwise stated, light travels from left to right.
2. The point of intersection between the surface and the axis is taken as the local origin of coordinates, O.
3. All distances are measured from O; distances to the top and right of O are taken as positive.
4. Angles are measured from the axis to the ray and are positive if counterclockwise. Similarly, the angles of incidence and refraction are measured form the surface normal, and are positive if counterclockwise.
5. For light going from right to left, the refractive index is taken as negative. Distances are also negative for light going from right to left.

For a thin lens of power K_i between media with refractive indices n and n', we can write

$$n_i' u_i' - n_i u_i = -h_i K_i$$

The effective focal length is $1/K_i$.

Appendix B

ETL Ray Tracing Formula

ETL Ray Tracing Derivation

John Green II

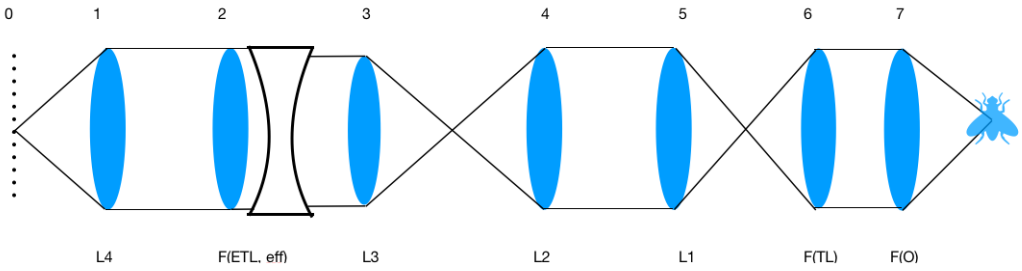

1 ETL Ray Tracing Formula

0) $u_0 = u_0$
$h_0 = 0$
The height of the rays coming into the camera is 0. The angle is arbitrary.

1) $u_1 = u_0$
$h_1 = u_1 L_4$

$u_1' = u_0 - \frac{u_0 L_4}{L_4} = 0$
$h_1' = u_0 L_4$
The rays are collimated after passing through L_4 (200mm).
The height after passing through L_4 is $u_0 L_4$.

2) $u_2 = 0$
$h_2 = u_0 L_4$

$u_2' = \frac{-u_0 L_4}{F_{ETL}}$
$h_2' = u_0 L_4$
The rays are collimated before they arrive at the ETL offset lens. After passing the ETL and offset lens, the angle is u_2', which is negative.
The height of the rays remains the same.

3) $u_3 = \frac{-u_0 L_4}{F_{ETL}}$
$h_3 = u_0 L_4 - \frac{u_0 L_4}{F_{ETL}} L_3$

$u_3' = \frac{-u_0 L_4}{F_{ETL}} - (\frac{1}{L_3})(u_0 L_4 - \frac{u_0 L_4}{F_{ETL,eff}} L_3) = \frac{-u_0 L_4}{F_{ETL,eff}} - \frac{u_0 L_4}{L_3}(1 - \frac{L_3}{F_{ETL,eff}}) = \frac{-u_0 L_4}{L_3}$
$h_3' = u_0 L_4 (1 - \frac{L_3}{F_{ETL}})$
The rays have a negative angle after L_3(300mm).
Height of the rays is h_3'.

4) $u_4 = \frac{-u_0 L_4}{L_3}$

$h_4 = u_0 L_4(1 - \frac{L_3}{F_{ETL,eff}}) - \frac{u_0 L_4}{L_3}(L_3 + L_2)$

$= u_0 L_4 - \frac{u_0 L_4 L_3}{F_{ETL,eff}} - u_0 L_4 - \frac{u_0 L_4 L_2}{L_3} = -u_0 L_4(\frac{L_3}{F_{ETL,eff}} + \frac{L_2}{L_3})$

$u'_4 = \frac{-u_0 L_4}{L_3} + \frac{u_0 L_4}{L_2}(\frac{L_3}{F_{ETL,eff}} + \frac{L_2}{L_3})$

$h'_4 = -u_0 L_4(\frac{L_3}{F_{ETL,eff}} + \frac{L_2}{L_3})$

The ray angle after L_2(200mm) is u'_4. It is a positive angle.
Height after L_2(200mm) is h'_4.

5) $u_5 = u_0(\frac{L_4 L_3}{L_2 F_{ETL,eff}})$

$h_5 = -u_0 L_4(\frac{L_3}{F_{ETL,eff}} + \frac{L_2}{L_3}) + u_0 \frac{L_4 L_3}{L_2 F_{ETL,eff}}(L_2 + L_1) + u_0(\frac{L_4 L_3}{F_{ETL,eff}})$

$= u_0(\frac{L_4 L_3 L_1}{L_1 F_{ETL,eff}})$

$u'_5 = -u_0(\frac{L_4 L_3}{L_2 F_{ETL,eff}} - \frac{L_4 L_2}{L_1 L_3}) + u_0(\frac{L_4 L_3}{L_2 F_{ETL,eff}}) = u_0(\frac{L_4 L_2}{L_1 L_3})$

$h'_5 = -u_0(\frac{L_4 L_2}{L_3}) + u_0(\frac{L_4 L_3 L_1}{L_2 F_{ETL,eff}})$

The angle after passing through is L_1 (80mm) is u'_5. Angle is positive.
Height after passing through L_1 (80mm) is h'_5.

6) $u_6 = u_0(\frac{L_4 L_2}{L_1 L_3})$

$h_6 = -u_0(\frac{L_4 L_2}{L_3}) + u_0(\frac{L_4 L_3 L_1}{L_2 F_{ETL,eff}}) + u_0(\frac{L_4 L_2}{L_1 L_3})(L_1 + F_{ETL,eff})$

$= u_0(\frac{L_4 L_3 L_1}{L_2 F_{ETL,eff}}) + u_0(\frac{L_4 L_2 F_{TL}}{L_1 L_3})$

$u'_6 = u_0(\frac{L_4 L_2}{L_1 L_3}) - u_0(\frac{L_4 L_3 L_1}{L_2 F_{TL} F_{ETL,eff}}) - u_0(\frac{L_4 L_2}{L_1 L_3}) = -u_0(\frac{L_4 L_3 L_1}{L_2 F_{TL} F_{ETL,eff}})$

$h'_6 = u_0(\frac{L_4 L_3 L_1}{L_2 F_{ETL,eff}}) + u_0(\frac{L_4 L_2 F_{TL}}{L_1 L_3})$

Ray angle after passing through the tube lens (180mm) is u'_6. Angle is negative.
Height after passing through the tube lens (180mm) is h'_6.

7) $u_7 = -u_0(\frac{L_4 L_3 L_1}{L_2 F_{TL} F_{ETL,eff}})$

$h_7 = u_0(\frac{L_4 L_3 L_1}{L_2 F_{ETL,eff}}) + u_0(\frac{L_4 L_2 F_{TL}}{L_1 L_3}) - u_0(\frac{L_4 L_3 L_1}{L_2 F_{TL} F_{ETL,eff}})(F_{TL} + F_{obj})$

$= u_0(\frac{L_4 L_2 F_{TL}}{L_1 L_3}) - u_0(\frac{L_4 L_3 L_1 F_{obj}}{L_2 F_{TL} F_{ETL,eff}})$

$u'_7 = -u_0(\frac{L_4 L_3 L_1}{L_2 F_{TL} F_{ETL,eff}}) - u_0(\frac{L_4 L_2 F_{TL}}{L_3 L_1 F_{obj}}) + u_0(\frac{L_4 L_3 L_1}{L_2 F_{TL} F_{ETL,eff}}) = -u_0(\frac{L_4 L_2 F_{TL}}{L_3 L_1 F_{obj}})$

To obtain the axial displacement, use the ray tracing equations to obtain the distance from the angle and height. Axial displacement, $\Delta z = -F_{obj} + \frac{h'_7}{u'_7}$.

The magnification, M = $\frac{F_{TL}}{F_{obj}}$.

$$\Delta z = -F_{obj} + \frac{(\frac{L_4 L_2 F_{TL}}{L_1 L_3} - \frac{L_4 L_3 L_1 F_{obj}}{L_2 F_{TL} F_{ETL,eff}})}{\frac{L_4 L_2 F_{TL}}{L_3 L_1 F_{obj}}}$$

$$= -F_{obj} + \frac{L_4 L_2 F_{TL}}{L_1 L_3} \frac{L_3 L_1 F_{obj}}{L_4 L_2 F_{TL}} - \frac{L_4 L_3 L_1 F_{obj}}{L_2 F_{TL} F_{ETL,eff}} \frac{L_3 L_1 F_{obj}}{L_4 L_2 F_{TL}}$$

$$= -(\frac{F_{obj}}{F_{TL}})^2 \frac{1}{F_{ETL,eff}} (\frac{L_1}{L_2})^2 L_3^2$$

$$= -(\frac{1}{M})^2 \frac{1}{F_{ETL,eff}} (\frac{L_1}{L_2})^2 L_3^2$$

Appendix C

Temperature Considerations of the ETL

The Optotune manual specifies the guaranteed range (+50 to +120mm) at 30° C. The manual also states increasing the temperature of the lens will decrease the focal length of the ETL by a factor of 0.67 diopters per 10° C [43]. This varying of temperature was a concern, therefore the ETL was run in the temperature independent Focal Power mode.

Appendix D

ETL Calibration & Imaging Procedure

Purpose: For future members of the Kner Lab to learn to operate and implement the ETL

Goal: To successfully calibrate and image for the ETL inside the light sheet microscope

Initial Light Sheet Setup

1. Turn on Light sheet system (Camera, lasers, multi-driver, and galvo power supply)
2. Add DI water to the specimen chamber and make sure the band is around the rotating wheel of the stage
3. Plug in ETL USB into the ETL Driver. Do not put the ETL in the detection path of the light sheet yet
4. Open the following Arduino files and sync them to the right ports:
    a. Laserpulse_board20190809_staticlightsheet to **COM6**, board should be synced to **Arduino Due (Programming Port)**
    b. Camtrigboard_20180717_arduinoboard to **COM7**, board should be synced to **Arduino/Genuino 101**
    c. Chipkitu32_sinwave to **COM5**, board should be synced to **chip KIT u32**
5. Open LabVIEW. Open the code **for LSM_GUI_Top16.** Run all 3 Arduino's in the block diagram labeled **ArduinoInitialize.** If there is an error, repeat steps 4 and 5. If there is still an error, unplug and replug the COM port USB and try again.

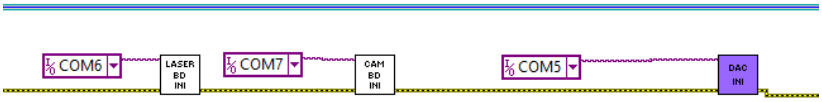

6. Go back to the front panel of LSM_GUI_Top16 and run the code**.** Place a sparse bead sample in stage and find them in the microscope and find the beads. Immediately hit the set camera button

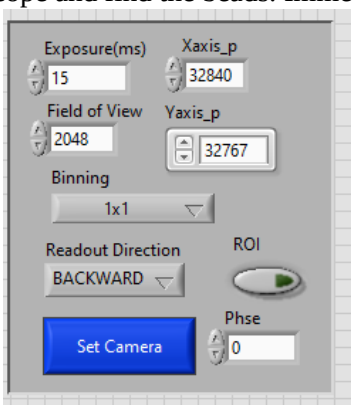

7. Turn on the laser to find the beads. Remember to type in the laser power> **click Set Laser**> and click the button under **488 Laser On**.

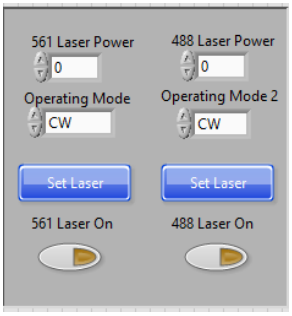

8. Find the middle of the bead tube in the x and z directions. Use the control panel below to move the stage.

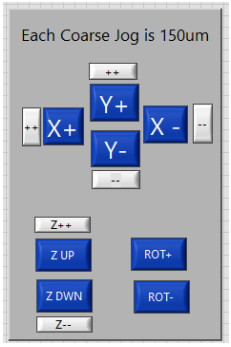

   a. To find the middle of the bead stack, find one edge of the bead stack in the z direction first and write down the z coordinate (it should be four digits long). Next, go to the back of the tube where the other end of the z range is and mark it down. Find the middle of the stack with the following equation: $\frac{z_{Max}-z_{Min}}{2} + z_{Min}$
   b. Send the 4D stage to the middle z coordinate.
   c. Next, find the two edges of the tube in the x direction. Compute where the middle of the tube is with the following equation: $\frac{x_{Max}-x_{Min}}{2} + x_{Min}$. It's important to do this step after finding the middle of the z stack because if taken in the wrong spot, calibration will be inaccurate.
   d. The y direction typically does not need to be changed unless not enough beads are in the frame of the camera.
   e. Send the stage to the coordinates of x,y, z. You input them here:

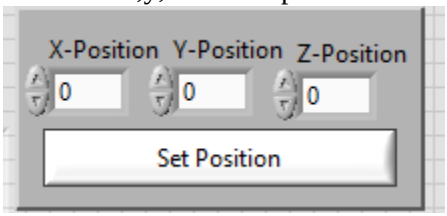

   f. Rotate the beads once in one direction and then rotate the beads in the opposite direction. This will make sure the stage is in the right place. The stage coordinates usually show up incorrectly until they are refreshed with this method. You can find the x, y, and z coordinates here.

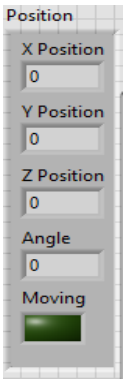

9. Keep the LSM_GUI_Top16 up and running. Make sure the x-galvo coordinate is in the middle position (it will be near 32767 but it could change depending on the illumination path was aligned). Turn off the laser to avoid exciting the beads unnecessarily.

ETL Calibration Part 1

The purpose of this section is to find the correct axial range to calibrate for.

1. Place ETL at the back pupil plane and turn on the lens driving software (should be called “Lens Driver Controller”). This means that the ETL should be placed where the image is sharpest in the BPP. If this is not done correctly, imaging calibration will not work. Plug in the USB into the ETL
2. Load the ETL driver software. The software can be found by clicking the windows home button and typing “lens”. It is the first software to pop up.

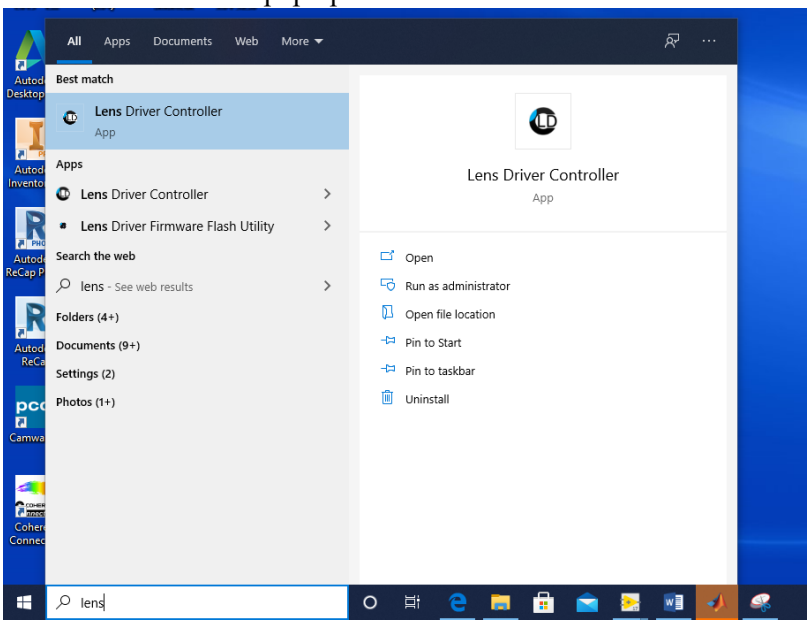

3. Switch the ETL Operation mode from current mode to **focal power mode**. Focal Power mode is temperature invariant. There will be a yellow (sometimes red warning sign) about the ETL being out of range. This is fine. Drag the ETL to the right so it can be in range.

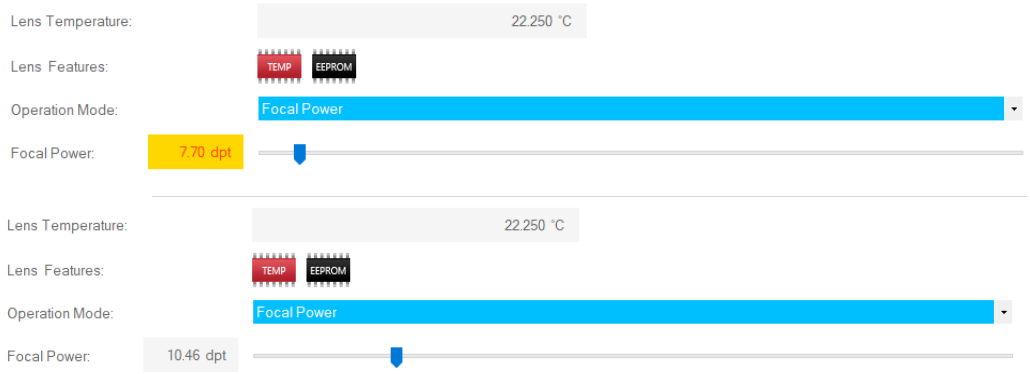

4. Turn on the laser in the LSM_GUI_Top16 LabVIEW code. Slide the ETL focal power until the beads can be see relatively focused. Move the x-galvo position to the front of the bead stack. This means the galvo position should be decreased.
    a. Drag the ETL focal power in the driving software from RIGHT to LEFT until the beads are found. Repeat this process until the front of the bead stack is found. Mark down the x-galvo position and the corresponding ETL Power needed to focus it. **(ex. Galvo = 32860; ETL = 12.16)**
5. Find the far end of the beads in the tube in the opposite x-galvo position. That means increase the x-galvo and slide the ETL driver from LEFT to RIGHT. At the far edge of the tube, record both the ETL and x-galvo positions. The far end positions should look like this (**ex. Galvo = 34860; ETL = 22.20**)
6. Keep in mind the inner diameter of the tube is 760 microns [47]. Write down the extended lower and upper bounds of the ETL. Usually I subtract 1 dpt from the lower and add 1 dpt to the upper bound (**ex. ETL1 =11.16, ETL2 = 23.20**). *THE EXTENDED RANGES ARE WHAT'S USED IN THE CALIBRATION*.
7. DO NOT MOVE THE STAGE AT THIS POINT
8. Click "**Quit**" in the LSM_GUI_Top16 code to make it stop running. Go to the Lens Driver Controller software and click **Disconnect**. Close the ETL software and close that program.

ETL Calibration Part 2

This purpose of this section is to correctly run the calibration code that gathers the image data.

1. Open the **FocalPowerSinewave Calibration** code
2. Make certain that the ETL software is closed and the LSM_GUI_Top16 code is not running. If either the ETL or camera are being accessed when this code is ran, there will be an error.
3. Input the base path. This is where the images that are captured will be saved. Make sure the name has not been already used. Note where this path is so that you can find it when it's time to convert then pictures from .dcimg to something useable like a .tif/.tiff file.
4. Input the laser COM number and laser power. Click on **Visa resource** name in the picture below to input the laser COM. The power input is next to it. The laser COM for the blue light is COM8. For the fluorescent beads, usually 20mW is used for imaging but it can range depending on how bright the beads need to be. The laser will only turn on while the for loop is running. It will turn

off once the loop is finished. Remember that the ND filters decrease the actual amount of power that makes its way into the sample.

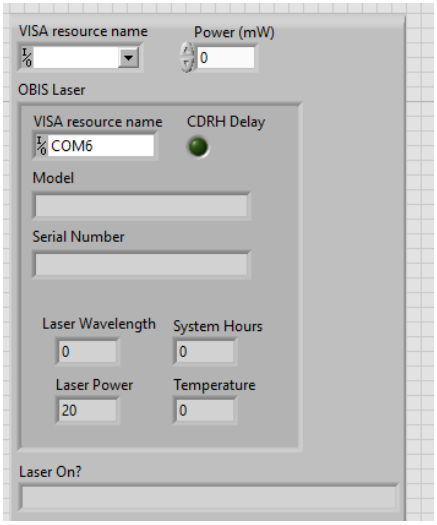

1. Input the amount of **Warm-up Volumes** for the ETL to warm up. This loop was implemented when the ETL was not being temperature compensated, but it has been kept as a precaution. This purpose of this loop is to drive the ETL a few times to get it ready. Usually, I use 5 or 10 loops. Next, select the **Volume(s) Desired**, **Frame(s) Desired**, and **exposure(ms)**. The exposure time directly controls how fast the images are required. Typically, the number of volumes is 30, and the number of frames is 100. This will mean that 3,000 images in total will be acquired.

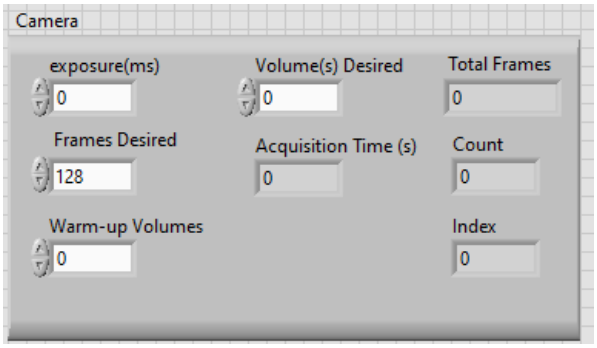

2. Input the start galvo and end galvo positions. The bounds determined in Part 1 of the ETL calibration. Use the same y-axis galvo position as from the calibration (in this case it would be **32860** for **Xaxis_ini**, and **34860** for **Xaxis_end**.

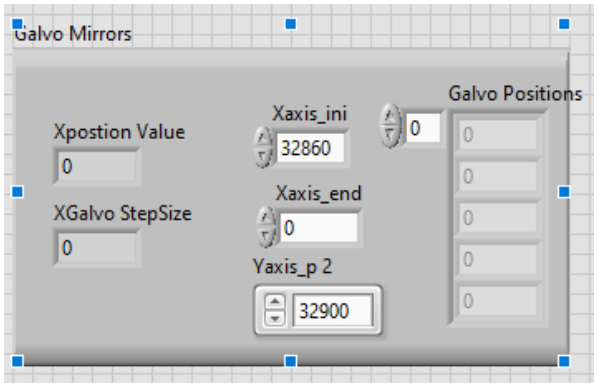

3. Input the ETL range that was acquired in Part 1 of the calibration into **Start Diopter** and **End Diopter**. This range is the extended one for both ends (In this case, **Start Diopter = 11.16** and **End Diopter = 23.20**). The purpose for extending the range was to give a better chance of capturing the bead data on both ends. The ETL will be driven sinusoidally between the bounds of the start and end diopters. The curve below is an example.

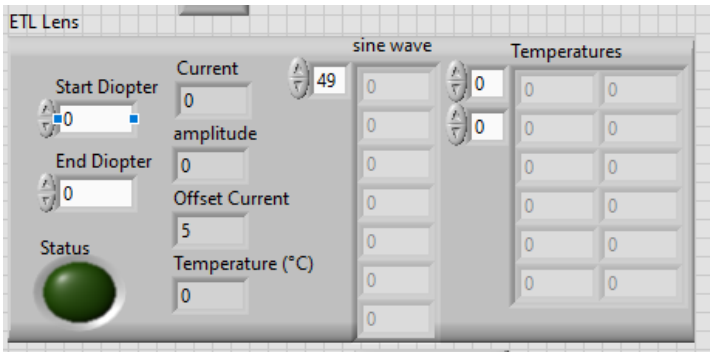

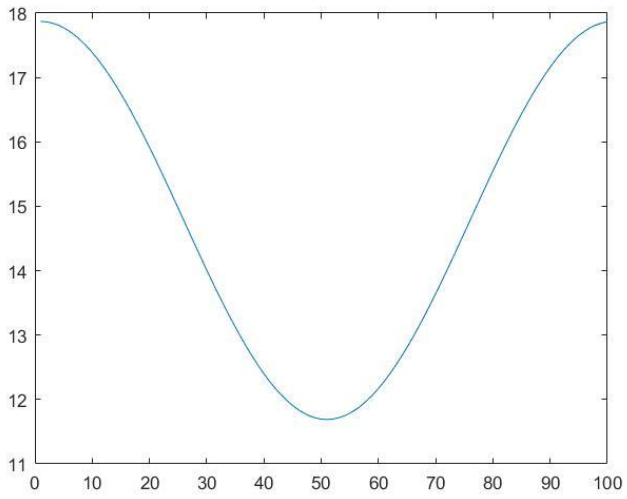

4. Run the code and wait for it to finish. The index of the images being acquired can be seen at the counter. Check the charts below to make sure the system is running correctly. The galvo chart

will show the galvo stepping after every volume. The focal power and diopter charts should look like sinewaves.

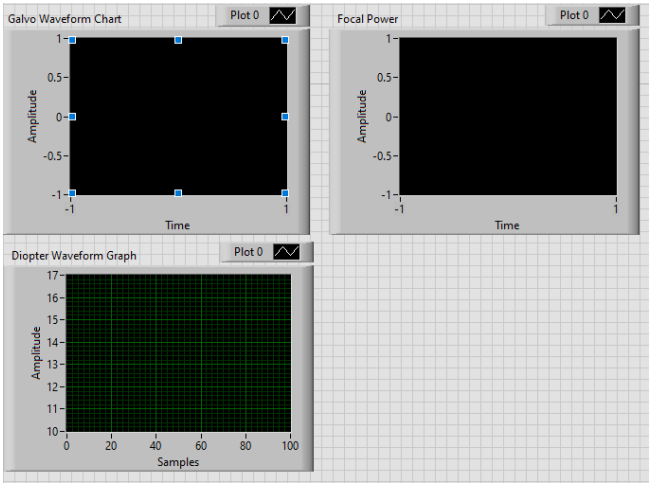

Image Conversion and Analysis

1. Hit the windows button, type in “hc” and select **HCImagingLive (x64)**. This program will convert the images into useable files.

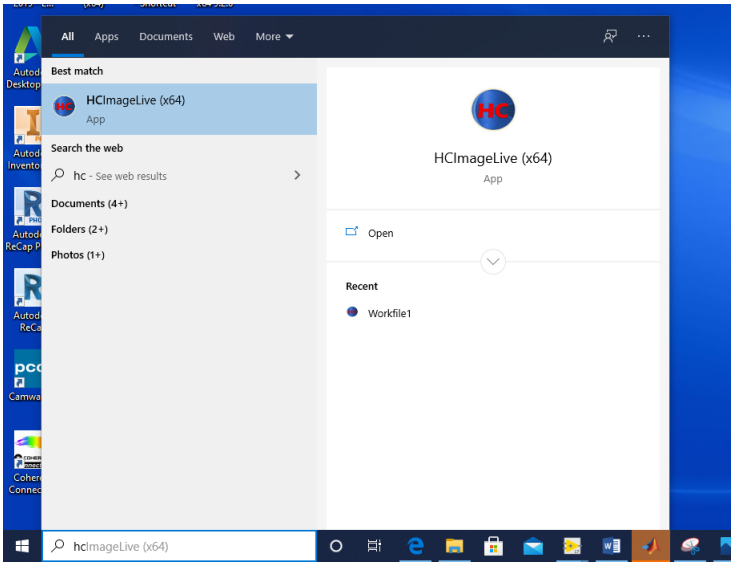

2. File>Batch Export
3. Under **Source**, browse to where the batch files were sent at the beginning of **ETL Calibration Part 2**.
4. The file names in the box below are what will be converted. Highlight any files not desired for conversion and hit the remove file. When the desired files are left in the box, look under the **Destination** side of the box and click **Browse** to find the conversion location you want. Select the file **Type**. I usually select **Tiff Files** (faster) or **Multi-Page Tiffs**

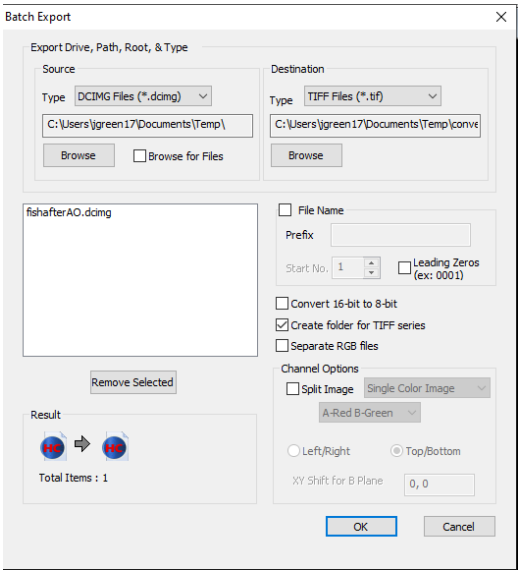

5. Convert the photos. Depending on the number of photos, the conversion process will take a several minutes.
6. When finished, close the **HCImagingLive (x64)**. This is important because it directly uses the camera's resources and can cause an error for the next time the camera is used.
7. Open **ImageJ** and drag the converted files into the program to open them.
8. If there are multiple files, concatenate them. Make sure all the photos are concatenated (check to make sure the number of photos taken in the calibration matches the total frame index in ImageJ.
9. Go to a bright frame in the image stack.
10. Control+Shift+C. This will open the box below. Hit "reset" to make sure the brightness doesn't saturate the images. Go to other images in ImageJ and make sure they are not saturated or too dark. You might need to switch between the **Auto** and **Reset buttons** or drag the brightness and contrast bars to get most of the beads in the stack to appear.

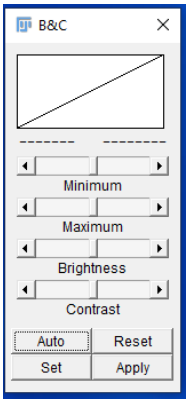

11. If most of the beads in the indexes are somewhat viewable, convert the index into 8-bit.
12. Save the image stack as a **TIFF**. *Move it to the same folder as the MATLAB code for sinewave calibration.*
13. Open MATLAB code named **FocalPowerSinewaveCalibration.m**
14. Make sure the **fname** in the MATLAB code matches the name of the stack saved from ImageJ.

15. Input the same start and end galvo points into **Galvo_Start** and **Galvo_End**. Enter the frame number into **frames_per_volume**. The code will automatically figure out how many volumes exist based off the frames input. Enter the start and ending diopters into **ETL_Start** and **ETL_End**
16. Run the MATLAB Script. The script will output some plots. There usually is hysteresis that shows up. The hysteresis means that when the ETL is being driven up and down, the ETL will image at different places even when the values are the same. Signs of a successful calibration look like the one below. Sometimes the forwards and backwards curves are closer together.

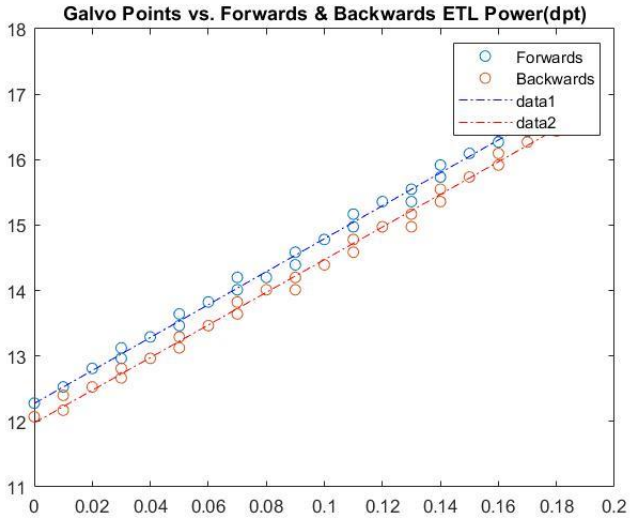

17. The MATLAB code will create a txt file called **FocalCalibration.txt** with the raw data of the forwards and backwards curves. The curves are used in the LabVIEW code for live imaging.

Testing the Calibration Curve

1. Open the live imaging code in LabVIEW named **ETL live and recording.**
2. Make sure no other programs are using the ETL and camera otherwise an error occur.
3. Make sure the file input to **Calibration File** is **FocalCalibration.txt**. It is the same name as the one generated by the MATLAB code.
4. Input the Laser COM as **COM8** and input the power. Input the base path and desired galvo range into **Galvo Start** and **Galvo End**.
    a. Note: the ETL is calibrated for specific range. It is possible to use a different galvo range than the one the system is calibrated for, but it is not necessarily guaranteed.
5. To get a live view of the beads and make sure the calibration works, make sure the button labeled **Recording** is not on. It should not be green. This code will run the camera in a while loop until told to stop. Hit the stop button when finished viewing.
6. To record images, click **Recording** and make sure its green. Make sure the file name is unique.
7. Run the code.
8. Convert the photos like described in the image conversion part of the document.

Appendix E

Code

Focal Power Code

```
%Image Evaluator
%John Green II August 2020
%Code to evaluate sharpness in images for sine sweeps

%Step 1 Import Stack
%Step 2 Apply Analysis
%Step 3 Put Values into an Excel Table

% Import Image
close all;
clear all;
fname = 'Nov102020Calibration1.tif'; %Assign tif a variable name
info = imfinfo(fname); %Assigns image info from all frames to a variable in a frame x
1 row
num_images = numel(info); %Gives total number of images
width = info.Width;
height = info.Height;
frames_per_vol = 100; %input('Enter the number of frames per volume: ');
volume_first_frame = 1:frames_per_vol:num_images; %displays first frame of new volume
volume_last_frame = volume_first_frame +(frames_per_vol-1);%displays final frame of
volume
total_volumes = length(volume_first_frame); %Displays total number of volumes

Galvo_Start=32767;
Galvo_End=34019;
GalvoStepSize= round((Galvo_End-Galvo_Start)/(total_volumes-1));
galvox_array = linspace(Galvo_Start, Galvo_End,total_volumes); %use this one if theres
an error in index
%galvox_array = Galvo_Start:GalvoStepSize:Galvo_End; %old way
%galvox_array = Galvo_Start:GalvoStepSize:Galvo_Start+GalvoStepSize*(total_volumes-1);
ETL_Start = 11.69;
ETL_End = 17.87;
ETL_Step_Size = (ETL_End-ETL_Start)/frames_per_vol;

ETL_Index=0:frames_per_vol-1;
ETL_Amplitude = (ETL_End - ETL_Start)/2;
Offset_Diopter= ETL_Start+ETL_Amplitude;
ETL_Wave = ETL_Amplitude*cos(2*pi/frames_per_vol*ETL_Index) + Offset_Diopter;
ETL_WaveF = ETL_Wave(1:frames_per_vol/2+1);
ETL_WaveB = ETL_Wave(frames_per_vol/2:frames_per_vol);
%cos by definition is pi/2 phase shift so that's why i used it
%plot(y)
ETL_array = ETL_Start:ETL_Step_Size:(ETL_End -ETL_Step_Size);
table = zeros([length(num_images/frames_per_vol),2]);

%Image Intensity Import
for i = 1:total_volumes
   for k = volume_first_frame(1,i):volume_last_frame(1,i)
       A = imread(fname, k, 'Info', info);
```

```
        Avg = mean(A(:));
        Sharpness(k) = std2(A)/Avg;
    end
end

%Read Values
for z = 1:total_volumes %length(volume_ref_end);

    Stack = Sharpness(1,(z-1)*frames_per_vol+1:z*frames_per_vol);%breaks Image
intensity into stacks
    StackF(z,:) = Stack(1,1:frames_per_vol/2);
    StackB(z,:) = flip(Stack(1,(frames_per_vol/2)+1:frames_per_vol));

    %Sharpness
    [S(z),Sindx(z)]=max(Stack); %Extracts best intensity values and index from each
stack
    Intensity_xposition(z) = galvox_array(z);
    Intensity_ETLposition(z) = ETL_array(Sindx(z));
    Intensity_Volume(z,:) = Stack; %Stores volume of intensity values

    %Forward Sharpness Index and Measurement
     [F(z),StackFindx(z)]=max(StackF(z,:));
     Forward_Intensity_ETLposition(z) = ETL_WaveF(StackFindx(z));
     ForwardsVolume(z,:)=StackF(z,:);
    %Backwards Sharpness Index and Measurement
     [B(z),StackBindx(z)]=max(StackB(z,:));
     Backwards_Intensity_ETLposition(z) = ETL_WaveB(StackBindx(z));
     %Backwards_Intensity_ETLposition(z) = ETL_WaveB((frames_per_vol/2)-
StackBindx(z));
     BackwardsVolume(z,:)=StackB(z,:);
    %Plots
    %Fit Points
    table(z,1) = Intensity_ETLposition(z);%position of best intensity of galvo
    table(z,2) = S(z);
    table(z,3)=galvox_array(z);
end
CompleteTable =
[galvox_array();Forward_Intensity_ETLposition();Backwards_Intensity_ETLposition()];
writematrix(CompleteTable,"FocalCalibration.txt");
figure(z+1)
Graph((z+1)) = plot(Sharpness);
title('Sharpness Across All Frames')
figure(z+2)
plot(table(:,3),Forward_Intensity_ETLposition(),table(:,3),flip(Backwards_Intensity_ET
Lposition())),legend('Forwards','Backwards');
title('Galvo Points vs. Forwards & Backwards ETL Power(dpt)')
Galvo_Angle = round(table(:,3)*10/65535,2)-5;
P_forwards = polyfit(Galvo_Angle,Forward_Intensity_ETLposition(),1);
yfit_forwards = P_forwards(1)*Galvo_Angle+P_forwards(2);

P_backwards = polyfit(Galvo_Angle,flip(Backwards_Intensity_ETLposition()),1);
yfit_backwards = P_backwards(1)*Galvo_Angle+P_backwards(2);
figure(z+3)
plot(Galvo_Angle,Forward_Intensity_ETLposition(),'o',Galvo_Angle,flip(Backwards_Intens
ity_ETLposition()),'o'),legend('Forwards','Backwards');
hold on
plot(Galvo_Angle,yfit_forwards,'b-.')
plot(Galvo_Angle,yfit_backwards,'r-.')
title('Galvo Points vs. Forwards & Backwards ETL Power(dpt)')
```

Normalized 2D Cross Correlation Code

```
%FishCrossCorrelation2
%March 8th, 2021
%This code runs a 2D normalized cross-correlation of all reference frames
%with ETL frames
close all;
clear all;
%import reference images (Static Volume) and Test Images (ETL Volume)
RefStack = 'FishStaticSubstackScale512.tif'; %put reference stack here
ETLStack = 'FishETLSubStackScale512.tif'; %put etl stack here


ref_info = imfinfo(RefStack); %Grabs all reference image info
ref_width = ref_info.Width;
ref_height = ref_info.Height;
ref_num_images = numel(ref_info); %Gives total number of reference images

ETL_info = imfinfo(ETLStack);%Grabs all ETL image info
ETL_width = ETL_info.Width;
ETL_height = ETL_info.Height;
ETL_num_images = numel(ETL_info); %Gives total number of ETL images

%Select Subsection of reference image. Want that subsection consisten with
%rest of reference images
x = 382;
X = 506;
szx = x:X;%coordinate of subsection in x

y = 312;
Y = 403;
szy = y:Y;%coordinate of subsection in y
   %Read in Reference Frame Data
   for i = 1:ref_num_images
       A = imread(RefStack, i, 'Info', ref_info);
       Ref_Frame(:,i) = {A};
       RefSubSect(:,i) = {A(szx,szy)}; %subsection

   end

   %Read in ETL frame data (i.e. the pixels)
   for j = 1:ETL_num_images
       B = imread(ETLStack, j, 'Info', ETL_info);
       ETL_Frame(:,j) = {B}; %store each frame's pixels in a cell array for
verification if needed
       %ETLSubSect(:,j) = {B(szx,szy)}; %subsection
   end
%Compute 2D Normalized Cross-Correlation normxcorr2(Ref,ETL
%will need two for loops. 1) for cross referencing 1 ref against all ETL
%and 2) for incrementing ref image

for l = 1:ref_num_images
   for k = 1:ETL_num_images
         c = normxcorr2(cell2mat(RefSubSect(1,l)),cell2mat(ETL_Frame(1,k)));
         %The above line runs a normalized 2D cross correlation

         crossdata{l,k} = c; %stores 2d normalized cross-correlations of stack
         MaxCorr(l,k) = max(max(c)); %stores max correlation coefficient of each
matrix

         [ypeak,xpeak] = find(c==max(c(:)));
```

```
   end
          %figure(l)
          %plot(MaxCorr(l,:)) %makes a plot of each frame where the
          %correlation is the strongest for every l row

   counter = l
end


for p = 1:ref_num_images
   BestCorr(p,1) =  max(MaxCorr(p,:)); %stores max correlation for each reference

   [row,col]=find(MaxCorr(p,:)==max(MaxCorr(p,:)));
   BestCorr(p,2) = col;
   CorrETLFrame(p,:) = find(MaxCorr(p,:)==max(MaxCorr(p,:)));

end


   %need to get ETL Focal Power Again

   figure()
   plot(1:ref_num_images,CorrETLFrame) %plots Correlated ETL Frame with ref frames
   title('Correlation of Frames')
   xlabel('Stage Movement Frame Index')
   ylabel('ETL Frame Index')
```

Published with MATLAB® R2020b

Appendix F

Mounting Procedures

Bead Mounting Procedure

200nm yellow-green fluorescent beads (ThermoFisher Scientific F8811) were diluted to a ratio of 1:200 in 2.0% agarose. Sparse samples (dilutions of greater than 1:200) seemed to reduce the effects of the hysteresis curve when compared to calibration maps built with denser bead samples using a 1:50 dilution. The agarose gel is ideal because its index of refraction is close to that of water and is compatible with in-vivo imaging as well as the water-dipping objectives [48]. 0.2 grams of agarose powder (Bio-Rad, Certified Molecular Biology Agarose 1613101) were added to 10 milliliters of DI water to make the mass concentration 2.0%. Next, the agarose solution was heated in a microwave for intervals of 45 seconds. This process was continued until the agarose became a gel mixture. After 1-2 minutes have passed for the agarose gel to cool down to safe handling temperature, the agarose gel was ready to hold the beads in place for imaging analysis. 2.0 milliliters of beads were added to 400 milliliters of agarose to achieve the 1:200 ratio. The bead-gel mixture is then placed inside of a FEP tube (Valco-TFEP130; OD 1.59mm, ID 0.76mm) [25] via a microliter pipette. Both ends of the FEP tube were plugged with parafilm (Parafilm PM 992).

The FEP tube preparation was based on the procedure from Involve3D group [49]. The FEP tubes were prepared by cutting them into 15mm tube sections. The tubes were straightened by placing them inside stainless steel tubes (0.09in OD and 0.02in wall thickness (McMaster-Carr 5560K761). We heated the stainless steel tubes at 180ºC for 30 minutes. The straightened

FEP tubes were set aside to cool for 3 hours. The FEP tube was placed in the stage holder of the 4D-stage (Picard industries USB 4D-STAGE). The 4D stage was used to physically move the middle of the bead sample to the detective objective's focal plane.

Zebrafish Mounting Procedure

The mounting of the zebrafish larvae was adapted from the procedure of the Weber group [48]. The James Lauderdale lab supplied zebrafish of the transgenic *elavl3:GCaMP5g;gad1b:DsRed;mitfa*$^{w2/w2}$ line. We imaged the GCaMP calcium indicator (excitation 488 nm, emission 515 nm) which is expressed in the central nervous system and measures neural activity. The fish were mounted between 3 to 5 days after fertilization. First, the fish were treated with alpha-bungarotoxin (125.25μM α-BTX) to induce paralysis. The fish were left in the alpha-bungarotoxin for 20 minutes to paralyze the fish. Immediately after the 20 minutes have passed, the fish were treated with 15 mM PTZ to induce seizure events that could be captured by the light sheet microscope operating at high speeds. The zebrafish were immediately placed inside 0.2% agarose solution. The 0.2% agarose solution was prepared by adding 0.02 grams of agarose to 10 milliliters of DI water. The mixture was microwaved for 45 second intervals until the mixture had the consistency of gel. The mixture was set aside to cool for 3 minutes so that the hot temperature of the agarose solution would not harm the zebrafish. After the agarose had cooled down to near room temperature levels, the agarose was placed on top of the zebrafish. The zebrafish were transported into 1cm FEP tubes via μL pipette. Both ends of the FEP tubes were plugged and sealed with parafilm (Figure 57).

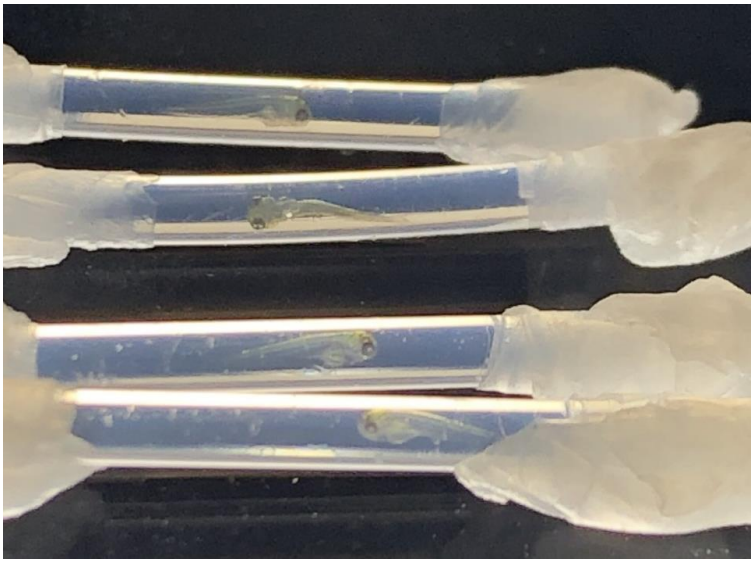

Figure 57. Four zebrafish larvae mounted within 0.2% agarose solution inside a FEP tube.